Laboratory Measurements of Deep-Water Breaking Waves

R. J. Rapp and W. K. Melville

Phil. Trans. R. Soc. Lond. A 1990 **331**, 735-800
doi: 10.1098/rsta.1990.0098

Phil. Trans. R. Soc. Lond. A **331**, 735–800 (1990)

Printed in Great Britain

LABORATORY MEASUREMENTS OF DEEP-WATER BREAKING WAVES

By R. J. RAPP† and W. K. MELVILLE

Massachusetts Institute of Technology, Cambridge, Massachusetts 02139, *U.S.A.*

(*Communicated by M. S. Longuet-Higgins, F.R.S. – Received* 15 *April* 1988 –
Revised 24 *October* 1989)

[Plates 1–4]

The results of laboratory experiments on unsteady deep-water breaking waves are reported. The experiments exploit the dispersion of deep-water waves to generate a single breaking wave group. The direct effects of breaking are then confined to a finite region in the wave channel and the influence of breaking on the evolution of the wave field can be examined by measuring fluxes into and out of the breaking region. This technique was used by us in a preliminary series of measurements.

The loss of excess momentum flux and energy flux from the wave group was measured and found to range from 10% for single spilling events to as much as 25% for plunging breakers.

Mixing due to breaking was studied by photographing the evolution of a dye patch as it was mixed into the water column. It was found that the maximum depth of the dye cloud grew linearly in time for one to two wave periods, and then followed a $t^{\frac{1}{4}}$ power law (t is the time from breaking) over a range of breaking intensities and scales. The dyed region reached depths of two to three wave heights and horizontal lengths of approximately one wavelength within five wave periods of breaking.

A detailed velocity survey of the breaking region was made and ensemble averages taken of the non-stationary flow. Mean surface currents in the range 0.02–0.03 C (C is the characteristic phase speed) were generated and took as many as 60 wave periods to decay to 0.005 C. A deeper return flow due to momentum lost from the forced long wave was measured. Together these flows gave a rotational region of approximately one wavelength. Turbulent root mean square velocities of approximately 0.02 C were measured near the surface and were still significant at depths of three to four wave heights.

More than 90% of the energy lost from the waves was dissipated within four wave periods. Subsequently measured kinetic energy in the residual flow was found to have a t^{-1} dependence.

Correlation of all the above measurements with the amplitude, bandwidth and phase of the wave group was found to be good, as was scaling of the results with the centre frequency of the group. Local measures of the breaking wave were not found to correlate well with the dynamical measurements.

---

† Present address: AT&T Bell Laboratories, Whippany, New Jersey 07981, U.S.A.

[Published 30 June 1990

CONTENTS

	PAGE
1. Introduction	736
1.1. Review	736
1.2. The experimental approach	738
2. The experiments	740
2.1. The experimental facility	740
2.2. Instrumentation	741
2.3. Generation of the breaking wave packet	744
2.4. Methodology of estimating momentum and energy fluxes	748
3. Surface displacement measurements of breaking wave packets	750
3.1. General observations, time series and photographs	750
3.2. The excess momentum flux	753
3.3. Loss of excess momentum flux due to breaking	758
3.4. Local wave parameters at breaking and steepness at breaking	762
3.5. Evolution of the frequency spectrum	764
4. Flow visualization of mixing in the breaking region	768
4.1. Procedures and analysis	768
4.2. Spatial evolution of mixing	770
4.3. Mixed region dependence on wave packet amplitude	774
4.4. The integral length scale of turbulence	775
5. Velocity measurements in the breaking region	775
5.1. Procedures and analysis	775
5.2. Mean velocities induced by breaking	780
5.3. Turbulent velocities induced by breaking	784
5.4. The balance of total momentum and energy	787
5.5. Decay of turbulence and dissipation estimates	794
6. Conclusions	795
Appendix. Second-order estimates of mass, momentum and energy fluxes	796
References	799

1. INTRODUCTION

1.1. *Review*

The breaking of surface waves in deep water is an important fluid dynamical process that is poorly understood. Current theoretical and numerical treatments of the problem fail at the point where the surface impacts upon itself, and models of the later stages of breaking are dependent on experimental measurements for guidance and testing. Field measurements alone can not fill this need and therefore well-controlled laboratory experiments are necessary to advance our knowledge. In this paper a programme of laboratory research is presented that investigates the role of unsteady breaking on the transfer of momentum from waves to currents, on the dissipation of wave energy, and on turbulent mixing in the water column.

Waves break over a wide range of scales and intensities, ranging from very gentle spilling waves only a few centimetres long with no significant entrainment, to violent plunging breakers perhaps ten to a hundred metres long. Breaking at the smaller scales is seen to occur in all but the lightest winds, and breaking is considered to be the most important mechanism limiting the height of, and dissipating, waves (Phillips 1977). However, it may also be important in wave generation (Banner & Melville 1976), and is believed to be a principal mechanism for the transfer of momentum from the wind to surface currents (Longuet-Higgins 1969). Breaking waves may lead to enhanced scattering of microwaves (Kwoh & Lake 1984; Banner & Fooks 1985; Melville *et al.* 1983; Kellar *et al.* 1990). The combined role of breaking in the transport and fluxes across the air–sea interface (Thorpe & Humphries 1980) and in microwave scattering may prove to be very important in remote sensing. Finally, breaking waves impose large forces, perhaps the extreme forces, on ships and offshore structures (Chan 1985), and have perhaps been responsible for catastrophic losses of offshore platforms.

Given this list of the ways in which breaking is important, it is at first surprising that so little attention has been paid to it in the past. To some extent this is due to the success of linear and weakly nonlinear wave theory in describing the more benign features of the sea surface, and the lack of detailed measurements, especially in stormy seas. Until the last decade the computing resources and numerical techniques were not available to describe the evolution of steep waves up to breaking, and oceanographic field instruments were not able to probe the wave zone below the surface. With the availability of the necessary computing speed and acoustic field instrumentation, increasing attention is being focused on breaking. However, numerical solutions are only available for waves up to breaking and field measurements lack the control required for detailed experimental studies.

For the results of laboratory studies to have relevance for breaking in the field they should duplicate, as closely as possible, the natural processes. Now, breaking in the field may result from direct wind forcing (Banner & Phillips 1974), wave–wave interaction, or wave instabilities (Melville 1982). For these experiments we were particularly concerned with simulating breaking around the peak of the wind–wave spectrum, in which significant air entrainment and mixing is possible. Our experience (Melville 1981; Melville & Rapp 1985) suggested that hydrodynamic instabilities of uniform wavetrains would not lead to significant air entrainment and mixing (at least not at laboratory scales), also, we anticipate that the direct influence of the wind is not important unless the fluxes from the wind (momentum and energy) in one wavelength are comparable with the flux carried by the waves. Thus, we would expect wind forcing to be unimportant for waves near the peak of the spectrum. Wave–current interaction is a limiting case of wave–wave interaction, and deserving of a separate study. Therefore, following Longuet-Higgins (1974) we chose to simulate wave–wave interactions in the laboratory. It is our belief that this is probably the single most important cause of breaking near the peak of the spectrum. Although we are not aware of any direct support for this statement there is indirect evidence. It is well known that many of the features of the statistics of surface waves are well described by linear models (Longuet-Higgins 1963; Shum & Melville 1984) of a random superposition of linear waves. It is also known (Holthuijsen & Herbers 1986), although extensive field measurements have not been done, that breaking near the peak of the spectrum is correlated with the groupiness of the wave field. The groupiness of the wind–wave field is a linear process at lowest order, but the dispersive properties of linear waves may lead to focusing of the waves and breaking (Longuet-Higgins 1974). Local nonlinear effects in the wave field may only be strong in the breaking process itself. This is in fact one of the conclusions of our work. This near linearity of the local wave statistics, of course, does not exclude slower secular changes due to weak nonlinear effects.

One distinct advantage of this method of generating breaking is that it is unsteady and localized, as is breaking in the field. This is in contrast to experiments and models of quasi-steady breaking. Longuet-Higgins & Turner (1974) presented a model of the whitecap as a gravity current moving down the forward face of the underlying wave, and compared their results with films of spilling breakers by Kjeldsen & Olsen (1972). Peregrine & Svendsen (1978) proposed a turbulent mixing layer model for the leading edge of a whitecap. In contrast, measurements by Duncan (1981) and Battjes & Sakai (1981) of quasi-steady breaking induced by the flow over a hydrofoil show, perhaps not surprisingly, wake-turbulence decay, and also rough agreement with the dissipation predictions of Longuet-Higgins & Turner (1974).

Research on unsteady breaking has been rather limited. Van Dorn & Pazan (1975) measured dissipation in unsteady breaking waves generated by converging channel walls. They found that dissipation of the wave energy depended on the initial wave steepness and the rate of convergence of the channel. Donelan (1978) produced an unsteady spilling breaker by linear superposition of a group of short waves followed by steep long waves. Dye at the surface was shown to mix down to a depth of the order of the wave height, but the rate of mixing was not reported.

Inherent in the approach adopted here is the fact that the groupiness of the wave field is important. If direct forcing of breaking by the wind is not dominant, it does not appear useful to consider a breaking wave in isolation. Implicit in quasi-steady models and attempts to isolate a single wave is the assumption of periodicity (on the scale of wavelengths and periods), which is clearly not appropriate for breaking near the peak of the spectrum. Therefore, we instead consider the entire wave group as the important feature.

1.2. *The experimental approach*

The intent of these experiments is to generate a single breaking wave group in the laboratory, modelling a process that normally occurs at random times and locations in the ocean. Of interest is the loss of momentum flux and energy flux from the wave group under various levels of breaking intensity. This loss is then related to the growth of the turbulent mixed region under the breaking wave and to mean surface currents generated due to the breaking. Most importantly, these losses are determined as functions of the wave parameters: amplitude, bandwidth and phase. We model wave–wave interaction induced breaking by generating a unidirectional frequency-modulated wave packet so that wave energy is focused at a predetermined time and location. The breaking generates currents and turbulence in an isolated region, while the residual wave packet continues to propagate downstream. The wave motions and the induced motions are subsequently separated in space so that each can be measured independently (figure 1). Waves of other frequencies may be expected to be radiated both upstream and downstream from the breaking region and can also be measured. The effects of wind are not considered in these experiments, although it is known to influence wave breaking and also generate shear currents at the surface layer. In these experiments, we will determine the extent to which breaking alone is responsible for generating surface currents and Reynolds stresses. Measurements of this type must be done on a single wave packet, where

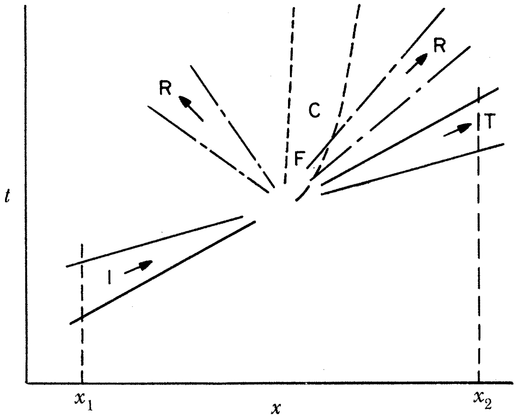

FIGURE 1. Schematic of separation of motion as a wave packet goes through breaking. Incident waves, I; transmitted waves, T; radiated waves, R; turbulence, F; currents, C.

measurements can be made on the packet before and after breaking to determine the losses from the waves. Also, because the turbulent flow field generated at breaking is non-stationary, turbulent statistics can only be determined by ensemble averages of many repeats of the experiment under identical initial and boundary conditions. These types of measurements are practically impossible to obtain in the field and so are done in a well controlled laboratory wave channel. Further, the long lived, slowly decaying fluid motions generated by the breaking can be measured without the influence of the motions generated by other breaking waves as in the field.

Modelling breaking in the laboratory also allows accurate control over the input wave parameters, and allows use of instrumentation not suited to the field. As the wave is very repeatable, the measurement point can be varied to densely sample the entire turbulent flow field under identical wave conditions. The inherent disadvantages of laboratory simulations are reflections due to a finite-length channel and the problem of scaling the results to full scale. The second problem is addressed by measuring at three scales. Wave groups are generated with centre frequencies over the range $f_c = 0.88$–1.28 Hz, which correspond to wavelengths of about 2 m to 1 m. A comparison over this range will give some confidence as to scaling the results to field conditions. The problem of reflections is minimized by installing an efficient dissipating beach. Because a finite length packet is generated in these transient experiments, measurement can be made on the transmitted packet before reflections travel back to the measurement point.

In the course of these measurements, we have found it advantageous to consider the momentum flux and energy flux loss from the wave packet as opposed to considering individual waves. The packet envelope may be considered as the important feature, as the carrier waves propagate through the packet and disappear at the front. Any loss of momentum flux results in a decrease of the envelope amplitude. Also, the wave energy travels with the group. In some cases several wave-breaking events were observed to occur in the packet at intervals of twice the carrier wave period. The sum of these losses is determined by measuring the entire packet downstream of breaking. Further, it is anticipated that breaking wave statistics can be related to wave-group statistics for which a body of work is being developed (Longuet-Higgins 1984).

Critical to the understanding of the losses from the waves and the momentum entering the mean flow and energy going into turbulence, is the ability to identify and separate these motions. With field measurements, the assumption is usually made that under stationary wave conditions, the turbulence is also stationary; the contributions from many overlapping breaking waves are added together. The wave motions and turbulent motions are usually separated using linear filtration methods (Thornton 1979; Benilov 1978; Kitaigorodski *et al.* 1983). The assumption that the wave velocity, considered to be a linear function of the surface displacement, is not correlated with the turbulence must be made in this filtration method. Turbulence under an isolated breaking wave cannot be assumed to be stationary, however. In these experiments, the ensemble averaging effectively separates these two contributions without assuming that the waves and turbulence are uncorrelated. Also, the turbulence and mean motion can be separated in time from the wave packet because the wave packet propagates away from the breaking region (figure 1).

The experiments are divided into three sections, addressing (*a*) the losses of momentum flux and energy flux from the waves, (*b*) the rate and extent of mixing and (*c*) the velocity field in the breaking region. The losses from the waves, as a function of the wave-packet parameters, are based on surface displacement measurements upstream and downstream of breaking. The momentum flux and energy flux due to the carrier waves is estimated to second order in wave slope using weakly nonlinear wave theory and shown to be proportional to the surface displacement variance, $\overline{\eta^2}$. These results are presented in §3. Then the distribution of momentum and energy lost from the wave field is investigated. This is done by first establishing the spatial limits of the region of the water column affected by breaking. Breaking causes dye, initially floating on the surface, to be mixed down. The dye boundary is recorded photographically and is used as an estimate of the mixed region. These results were found to be of importance in their own right and are presented in §4. Measurements of horizontal and vertical velocities are made at grid points in the breaking region, defined by the dye boundary. Ten breaking event repetitions at each point are ensemble averaged to determine the mean flow and turbulent velocities. These are all determined as functions of space and time. By using the measured velocities, the total momentum and energy remaining in the breaking region is compared to that lost from the waves. The time rate of decay of the kinetic energy is also presented in §5. Experimental methods are now discussed in §2.

2. The experiments

2.1. *The experimental facility*

The experiments were done at the Ralph M. Parsons Laboratory of The Massachusetts Institute of Technology in a glass walled channel 25 m long, 0.7 m wide, and filled to a depth of 0.6 m with fresh water (figure 2). A wooden beach of slope 1:10 covered with two-inch thick fibrous mats dissipated the waves at the far end of the tank with reflections of less than 0.16 % of the incident energy, or 4 % of the incident wave amplitude. The beach slope begins at 19.5 m from the wave paddle and extends to 25 m at the waterline. In these transient experiments, measurements were completed on the incident packet before the most energetic wave frequencies were reflected back to the measurement point, further reducing the influence of reflections.

The channel is equipped with a servo-controlled, hydraulically driven wave maker allowing pre-programmed wave packets to be generated. The hydraulic cylinder drives a rigid vertical bulkhead in a horizontal motion so the velocity at the paddle is uniform with depth. The

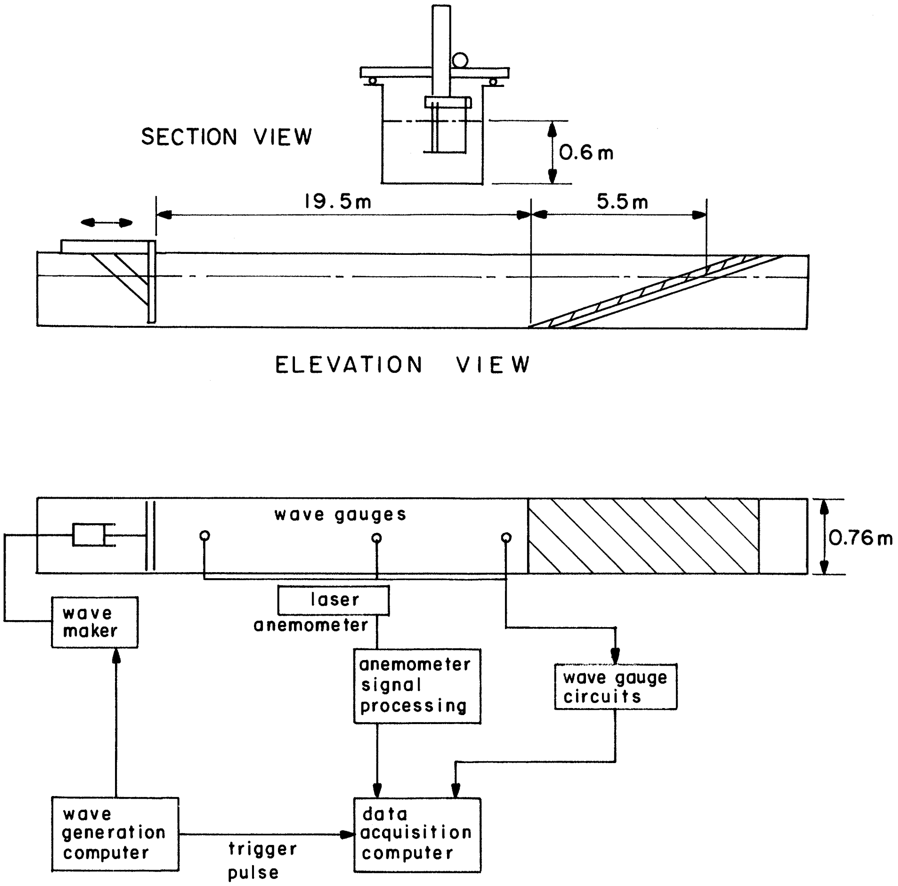

Figure 2. Wave channel and instrumentation.

paddle is supported from above by a carriage riding on rails fitted with linear ball bearings. The paddle is equipped with rubber wiper seals along the sides and bottom to reduce leakage and thus undesirable harmonic generation (Madsen 1970). The wavemaker system transfer function was carefully measured and used to obtain the desired wave spectrum. Very small variations in the paddle transfer function were detected due to hydraulic oil temperature variation in wave inpact pressure measurements (Chan 1985). These small variations could not be distinguished from the stochastic process of breaking itself as far as the parameters measured in these experiments are concerned (surface displacement and fluid velocity).

2.2. *Instrumentation*

The fluid surface displacement was measured with a set of six surface piercing resistance wire wave gauges (constructed at MIT) and resistance measuring circuitry purchased from the Danish Hydraulic Institute (Model 80-74G). The MIT gauge comprises two 0.127 mm diameter Nichrome wires (20 % chromium, 80 % nickel) spaced 4 mm apart, and stretched on a 45 cm by 15 cm frame made of 0.25 inch† diameter stainless steel tubing. The thin profile of the support, 15 cm away from the wires, gave no detectable flow disturbance on the surface displacement measurements or on the velocity measurements made near the probe. The gauge frame was mounted from above to a vertical two-inch square tube with a rack and pinion to

† 1 inch = 2.54×10^{-2} m.

allow accurate vertical positioning. This was mounted to a carriage riding on rails along the tank. The circuitry provides an AC excitation voltage to the wires. The return signal is amplified, demodulated and filtered to provide a DC voltage proportional to the surface displacement. The excitation signal and return signals are isolated by transformers in the circuits to eliminate interference between closely spaced gauges.

The complete system, including A/D sampling board, was calibrated by positioning the gauge at 2 cm increments over the expected range of surface displacements (+16 cm to −10 cm with respect to mean water level) and sampling the static water level. A third-order polynomial was fitted to the average voltage at each elevation, with a standard error for linear, second-, third- and fourth-order polynomials, which was typically 0.13, 0.09, 0.01, 0.01 cm respectively. This error is interpreted as the gauge resolution. The variation of the linear term was less than 1% over 8 h. A 'zero' record of the still water level was recorded for 40 s before each run and subtracted from the measured data to remove any zero drift. It was found to be less than 0.5 cm over 8 h.

Simultaneous horizontal and vertical fluid velocity measurements were made with a laser doppler anemometer (LDA) operated in the dual beam backscatter mode with counter data processors. The laser is a Lexcel Model 95-2, 2 W argon ion laser, which outputs wavelengths in the range 514.5–457.9 nm; the strongest wavelengths being 488.0 nm and 514.5 nm. These lines were used for measuring the horizontal and vertical velocities respectively. The laser was equipped with an etalon filter to obtain the required beam coherence length. The laser and optics (TSI, equivalent to the model 9100-7 system) were mounted on a two-inch thick rigid bench, which in turn was mounted to a cantilevered carriage riding on rails above the channel. The carriage allowed vertical, transverse and longitudinal motion so the measurement point could be positioned anywhere in the channel.

The focusing lens was placed close to the glass so that the required focal length could be minimized (250 mm), because the amplitude of the backscattered signal is proportional to the inverse of the focal length squared. It is also important that the measurement point be close to the channel centre, away from the boundary layer which is estimated to be $\delta = (2\nu/\omega)^{\frac{1}{2}}$ or typically 0.06 cm thick (ν is the kinematic viscosity and ω is the wave radian frequency). The beam crossing and measurement point was typically 17 cm away from the channel wall. The beam spacing was 50 mm.

The water in the wave channel was seeded with silicon carbide particles of 1.5 μm mean diameter and density of 3.2 g cm^{-3}. The backscattered light from these particles was detected by a photomultiplier tube resulting in a signal whose frequency, f_{m}, is proportional to the particle velocity, u, given by

$$u = (f_{\mathrm{m}} - f_{\mathrm{shift}})\,\lambda/2\sin k.$$

Here λ is the laser light wavelength, k is the beam intersection half angle and f_{shift} is the frequency shift induced in one of the incident beams using a Bragg cell. This allows an unambiguous determination of flow direction. The effective frequency shift was typically 100–200 kHz. The counters (TSI Models 1990 and 1980) have 1 and 2 ns of resolution respectively. They were operated in the continuous cycle mode, counting $N = 16$ cycles of the backscattered signal for each measurement, then counting again as long as at least 16 cycles remain in the burst produced by the particle crossing. Here N is the number of interference fringes crossed by a particle (see Rapp (1986) for details).

A time comparison circuit was used to reduce phase noise caused by multiple particles in the measurement volume. This circuit compares the time of crossing the first 10 fringes, with the total 16. If this ratio differs from 5:8 by more than 1% (adjustable) then the measurement is ignored. With this setting, the resolution of the measured frequency is $0.01f_m$, where f_m is the measured frequency.

The selection of N, the number of cycles counted per measurement, was made on the basis of reducing output noise (increasing accuracy of the measurement) but yet maintaining a high data rate. Also, it was kept low enough to reduce the effect of fringe or directional bias at the required frequency shift. (If N is too large, particles crossing at a steep angle to the fringe pattern may not cross enough fringes to register a measurement thus biasing the data to measurements crossing normal to the fringes.)

A typical raw velocity time history is shown below in figure 39 measured with the LDA configured as described. The root mean square (r.m.s.) noise levels for these signals are 0.34 cm s^{-1} and 0.2 cm s^{-1} for u, w velocities respectively ($u/c = 0.0019$, $w/c = 0.0012$, where c is the wave phase velocity). This noise is broadband and cannot be removed by frequency filtering.

The LDA signal was sampled via the digital output of the counter/processor. This port outputs 16 bits of data (12 mantissa, 4 exponent) representing the clock counts of the time for the particle to cross N fringes. As the LDA data rates were relatively high (1000–3000 Hz) compared with the sampling frequencies (50–200 Hz), the signal on the LDA was assumed to be continuous and sampled at equal increments in time rather than reading every data point. In this mode, it is not necessary to record the time of the data point.

The data acquisition system was based on a SMS (Scientific Micro Systems) LSI 11/23 computer with a 30 megabyte Winchester hard disk and an 8″ floppy drive. A magnetic tape drive was also installed for bulk data storage. Installed in the Q-bus was a DT 2769 (Data Translation) Real Time clock, a DT 2781 analogue/digital I/O board, used to sample the wave gauges, and two optically isolated digital I/O boards DT-2768-I, sampling the two digital LDA channels. The wave signal was input to the wavemaker from a separate Charles River Data Systems (CRDS) computer via a DT 2781 D/A channel. A batch master program was used to control the sampling, convert the raw data to physical units, and process the data for plotting. This was all done while the fluid motions in the wave channel decayed before the next run. The data sampling was initiated by a trigger step signal from the CRDS computer that marked the start of the wave packet signal. The step signal triggered the real time clock in the SMS computer. A minimum of 8 min elapsed between runs of the experiment. A double buffering configuration and background processing allowed continuous sampling and writing to disk for an almost unlimited time (limited by disk space). Also, when sampling the two digital channels and four analogue channels a sampling rate limitation of about 500 Hz was observed. When ensemble averaging many repeats of the experiment, a slow timing loop was set up to send trigger pulses and the wave signal at 8 min intervals. Data was automatically sampled and analysed between each repeat and no operator intervention was required.

The single point measurements of the surface displacement and velocity produced time series of these quantities; however, in this unsteady flow, the conversions to spatial dependence is not easy (if at all possible). Still photographs and ciné films were made to record the spatial profile of the free surface with time and also of dye being mixed from the surface.

The still photographs were taken with a $2\frac{1}{4} \times 2\frac{1}{4}$ inch format Hasselblad 500 EL/M camera with motor drive, and with a 35 mm Olympus OM 10 camera. The procedures were not novel but did require optimization of lighting and film exposure time.

Two lighting techniques were used. The photographs of figures 8 and 9 were taken with the

Hasselblad camera and zoom lens set at a focal length of 140 mm or 280 mm, by backlighting a cloth diffusion screen stretched behind the channel. Three flash units (Vivitar model 285, Vivitar model 100 and equivalent) provided the lighting. A flash was placed above the tank to light up the bubbling flow near the free surface. The higher power Vivitar model 285 flash was used at quarter power to reduce its flash duration to approximately $\frac{1}{1000}$ s, the same as the other two. An f stop of f/11 with Plus-X film at ASA 120 and a polarizing filter were used. Blue vegetable dye was mixed into the water to add contrast.

Another lighting technique produced the series of photographs in figure 10. Here a black vinyl coated cloth was placed behind the tank. Two flash units were placed under the tank and one overhead to provide lighting in an otherwise darkened room. Only the surface miniscus and the bubbles reflected light to the camera. The flash speed again was $\frac{1}{1000}$ s and f stop f/4 (camera set at $\frac{1}{60}$ s) with Ektachrome daylight film of ASA 200. To reduce haze effects, the water was filtered when the channel was filled and a polarizing filter used on the camera.

In all the still photographs the camera motor drive was triggered with a step signal from the CRDS computer, and transistor switch circuit, that was delayed by progressively longer times from the start of the wave signal. Each photograph is a separate run of the wave packet.

Ciné films were made under a continuous lighting arrangement and white background as described. A Bolex REX H16 movie camera was run at 64, 48 and 24 frames per second.

A series of films was made of the wave packet corresponding to incipient breaking, spilling and plunging for various bandwidth parameters; no dye was used. Another series of films was made of dye mixing for three scales of wave packets corresponding to incipient breaking, spilling and plunging.

2.3. *Generation of the breaking wave packet*

Techniques for generating breaking waves in a laboratory channel have been reported by Kjeldsen *et al.* (1980) and Longuet-Higgins (1974). Steady spilling breakers have been produced by the relative motion of a submerged hydrofoil and the surrounding fluid (Duncan 1981; Battjes & Sakai 1981) and by the steady motion of a surface-piercing hull (Longuet-Higgins 1974). A steady source of energy proportional to the drag times the velocity of the body is required to maintain the breaking. Unsteady breaking waves can be generated by focusing the wave energy in space; that is, by creating a local increase in energy density. For two-dimensional waves (i.e. unidirectional), the energy may be focused by a laterally converging channel wall (Van Dorn & Pazan 1975) or by a longitudinal focusing caused by the frequency dispersion (Longuet-Higgins 1974; Kjeldsen *et al.* 1980; Greenhow *et al.* 1982). Waves have also been shown to break as they pass through the Fresnel envelope at an advancing wave front produced when the wavemaker is started impulsively (Longuet-Higgins 1974). Melville (1982) experimentally showed that an initially uniform wave train that undergoes the Benjamin–Feir instability may lead to breaking as the carrier waves pass through the modulated envelope. This breaking is quasi-periodic, however, and the breaking location tends to oscillate along the channel length making repeatable measurements difficult.

The technique used in these experiments is, in principle, that described by Longuet-Higgins (1974) where wave energy if focused longitudinally by linearly decreasing the wavemaker frequency and thus increasing the group velocity of the generated waves leading to a dispersive focusing of the waves. In deepwater this is achieved by varying the paddle radian frequency, ω, by

$$\mathrm{d}\omega/\mathrm{d}t = -g/2x_\mathrm{b},$$

where x_b is the energy focal point, according to linear theory, as measured from the paddle. This signal is well known in the communications field as a 'chirp' pulse (Clay & Medwin 1977, p. 131). To reduce startup transients, the signal must also be smoothly brought to zero at the ends of the pulse. This technique has been shown to produce plunging breakers; however, x_b can only be specified to within a wavelength of the wave since no provision is available to specify the individual wave phases. The starting phase of the signal must be empirically determined to fine tune the breaking location (J. H. Milgram, personal communication).

We use a refinement of this basic focusing principle, that given by Greenhow *et al.* (1982), where a quasi-periodic signal is generated by a summation of 32 equal amplitude wave frequency components spaced uniformly in frequency over a specified band. The phase of each component is specified at the paddle so that, according to linear theory, constructive interference will occur at a point down the channel. As the purpose of these experiments is not only to produce a breaking wave, but also to be able to parametrize the input wave group, this method was considered superior.

It is believed that this method models a naturally occurring mechanism of unsteady breaking in the field, and a range of breaker types or intensities from gentle spilling to vigorous plunging can be generated. In this formulation, the resultant signal applied to the wavemaker is already modulated smoothly to zero in amplitude, making any further smoothing windows unnecessary. The method is simple to repeat and follows from basic principles of linear wave theory. The resultant breaking (or non-breaking packet) was extremely repeatable in time and space (to $\frac{1}{100}$ s over 17 s and to within ±2 cm in the horizontal direction in the 7 m of propagation from the paddle).

The free surface displacement, $\eta(x,t)$, can be specified by

$$\eta(x,t) = \sum_{n=1}^{N} a_n \cos(k_n x - 2\pi f_n t - \phi_n), \tag{2.1}$$

where a_n is the amplitude of the nth frequency component, k_n is the wavenumber, $2\pi f_n = \omega_n$ the radian frequency and ϕ_n the phase. N is the number of components, and k_n and f_n are related by the dispersion relation

$$(2\pi f_n)^2/g = k_n \tanh k_n d, \tag{2.2}$$

where d is the water depth and g is the gravitational constant. The phase of each component is computed by setting

$$\cos(k_n x - 2\pi f_n t - \phi_n) = 1$$

at $x = x_b$ and $t = t_b$, the location and time of focusing.

Then

$$\phi_n = k_n x_b - 2\pi f_n t_b + 2\pi m \quad (m = 0, \pm 1, \pm 2, \ldots)$$

and the surface displacement becomes

$$\eta(x,t) = \sum_{n=1}^{N} a_n \cos[k_n(x - x_b) - 2\pi f_n(t - t_b)]. \tag{2.3}$$

We define the mean paddle position to be $x = 0$, and the desired surface displacement at the paddle is

$$\eta(0,t') = \sum_{n=1}^{N} a_n \cos(-k_n x_b - 2\pi f_n t'), \tag{2.4}$$

where $t' = t - t_b$. The effect of changing t_b is to delay or advance the entire signal with no change in packet form or theoretical focal point, x_b. Note that this formulation is based on linear theory and nonlinear amplitude dispersion is not accounted for.

The variables that completely specify $\eta(x, t)$ in equation (2.3) are N, a_n, f_n, k_n, x_b, t_b. As f_n and k_n are related by equation (2.2), k_n can be eliminated but the depth, d, and gravity, g, are added as independent parameters. To simplify the frequency spectrum, we set

$$a_n = a_1 = a_2 \ldots a_N = \text{const.}$$

and define

$$a = a_n N. \tag{2.5}$$

We also specify the discrete frequencies f_n to be uniformly spaced over the band

$$\Delta f = f_N - f_1 \tag{2.6}$$

and define

$$f_c = \tfrac{1}{2}(f_N + f_1), \tag{2.7}$$

the central frequency. The non-dimensional wave packet parameters then become

$$ak_c, \Delta f/f_c, x_b k_c, k_c d, N,$$

where k_c is defined by

$$(2\pi f_c)^2/g = k_c \tanh k_c d. \tag{2.8}$$

A priori, $k_c d$ was considered to be of minor importance in the wave dynamics, because $\tanh(k_c d) = 0.96$, 0.99, 1.00, approximately constant for the three packet centre frequencies used ($f_c = 0.88$, 1.08, 1.28 Hz). To be consistent in this regard, the deep water dispersion relation was used to compute k_n from f_n in equation (2.4).

N was made relatively large ($N = 32$) to approximate a continuous spectrum and to eliminate its dependence. Finally, the following functional relation results from the dimensional analysis:

$$\eta k_c = \eta k_c(x k_c, t f_c; a k_c, \Delta f/f_c, x_b k_c). \tag{2.9}$$

Families of wave packets were computed by systematically varying $\Delta f/f_c$ and $x_b k_c$. The amplitude, ak_c, was varied by multiplying the summed packet by a gain factor. The desired spectrum and signal for a typical set of packet parameters is shown in figures 3 and 4. The signal envelope is periodic with period $T' = 1/\delta f$ where δf is the input spectral resolution $\delta f =$

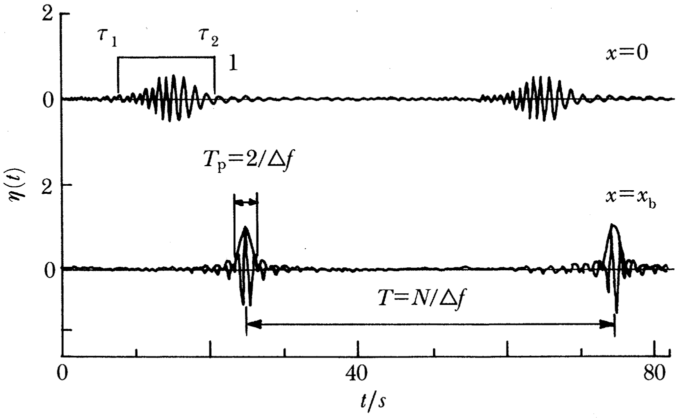

FIGURE 3. Ideal packet signal for $a_n = 1/N$ ($N = 32$), $\Delta f/f_c = 0.73$, $f_c = 1.08$ Hz. Also shown are input signal window limits τ_1 and τ_2.

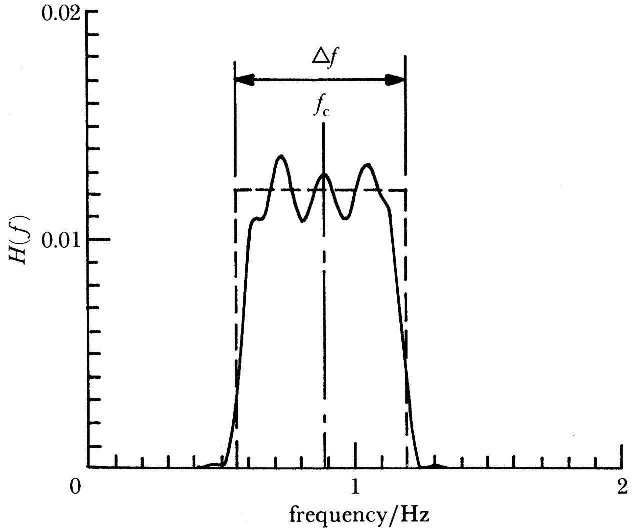

FIGURE 4. Frequency spectra of ideal periodic signal in figure 3, ---- and spectra of windowed signal, ——.

$\Delta f/N$. As the number of components within the band Δf is made large, T' also increases. For practical reasons, the signal was truncated or windowed in time with a box car function $w(t)$, giving a signal at $x = 0$ of

$$\eta'(0,t) = \eta(0,t)\cdot w(t),$$

where

$$w(t)\begin{cases} = 1 & (\tau_1 < t < \tau_2), \\ = 0 \text{ elsewhere.} \end{cases} \tag{2.10}$$

The effect of the window on the ideal-frequency spectrum is found by taking the Fourier transform of $\eta'(0,t)$, which is the convolution of the original spectrum with the Fourier transform of the window. Thus

$$H'(0,f) = H(0,f)\,W(f), \tag{2.11}$$

where

$$H(0,f) = \int_{-\frac{1}{2}T'}^{\frac{1}{2}T'} \eta(0,t)\,\mathrm{e}^{-\mathrm{i}2\pi ft}\,\mathrm{d}t \tag{2.12}$$

and

$$W(f) = \int_{-\frac{1}{2}T'}^{\frac{1}{2}T'} w(t)\,\mathrm{e}^{-\mathrm{i}2\pi ft}\,\mathrm{d}t \tag{2.13}$$

are Fourier transforms.

The resultant spectrum is also shown in figure 4. The Gibbs' phenomenon is manifested in this spectrum. Various techniques are available to reduce these oscillations to better approximate the ideal spectrum; however, for the purpose of this experiment, and to reduce the complexity of the input packet formulation, additional optimization was considered unnecessary. The reader is referred to Oppenheim & Shafer (1975, pp. 239–250) for a more detailed account of these methods.

The effect of varying the non-dimensional wave amplitude ak_c is simply to vary the wave height and thus the momentum and energy flux in the propagating packet. Thus a is a measure of the theoretical wave amplitude at the focal point and is independent of $\Delta f/f_c$ and $x_b k_c$, but depends on N. Increasing $\Delta f/f_c$ results in decreasing the length or period of the packet and thus increases the packet-envelope steepness. For a given wave centre frequency, f_c, the number of waves in the packet equals $2f_c/\Delta f$. Also, because N is a constant, the frequency spectrum resolution varies as $\delta f = N/\Delta f$ and the power spectrum energy density is $S(f) \propto (a_n^2 \cdot N)/\Delta f$. According to linear theory, changes in $x_b k$, should have no effect on the breaking dynamics, but only change the x reference location. This can be seen from equation (2.3). The phase distribution is a function of $(x - x_b)$ and not x_b alone. (In practice, phase mismatch error between frequency components and nonlinear dispersion effects becomes greater as x_b is increased. These will be discussed in §3.)

The desired surface displacement at the paddle position, $\eta'(0, t)$, is realized by applying an input voltage to the wavemaker system that is corrected in amplitude and phase for the complete servo controller, hydraulic system, and wave paddle transfer function.

2.4. *Methodology of estimating momentum and energy fluxes*

The net loss of total mass flux, horizontal momentum flux, and energy flux from the wave packet as a result of breaking and the net gains to the water column are determined by applying the conservation equations to a control volume bounded from below the tank bottom, $z = -d$, and above by the free surface, η. Two verticals, far upstream and downstream of breaking, at x_1, x_2 (figure 5), close the volume. The deterministic motion is considered to be two dimensional, so the quantities are expressed per unit width across the tank. The coordinate system is defined in figure 5 with x, the longitudinal dimension referenced from the paddle, z is vertically upward from the still water line and y is across the channel. The eulerian velocities in the x, y, z direction are u, v, w respectively.

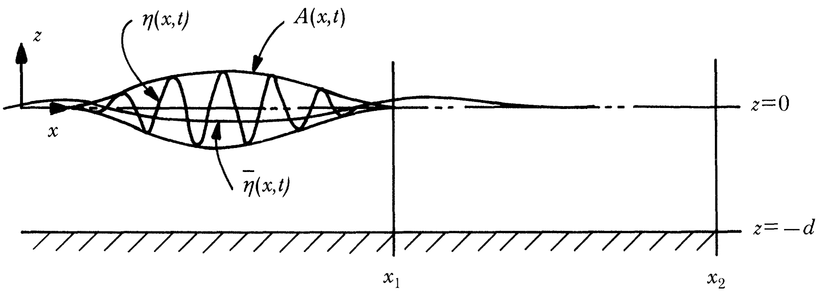

FIGURE 5. Definition sketch of wave packet.

The incident wave packet enters from upstream (the left) crossing x_1, breaking ensues in the control volume, and waves are transmitted downstream crossing x_2. The fluid motion at x_1 and x_2 is assumed to be completely due to waves; all mean currents and turbulence associated with breaking is contained within the control volume. The change in total mass, momentum and energy in the control volume from the initial state, can then be compared with the difference in the corresponding fluxes crossing x_1 and x_2. This is expressed by the conservation equations given by Whitham (1962) as follows

mass
$$\partial(\rho\bar{\eta})/\partial t + \partial M/\partial x = 0, \tag{2.14}$$

momentum
$$\partial M/\partial t + \partial S/\partial x = \bar{\tau}, \tag{2.15}$$

energy
$$\frac{\partial E}{\partial t} + \frac{\partial F}{\partial x} = \rho \overline{\int_{-d}^{\eta} \epsilon \, dz}, \tag{2.16}$$

where

$$\bar{\eta} = \frac{1}{T}\int_0^T \eta(x,t)\,\mathrm{d}t, \tag{2.17}$$

$$M = \overline{\int_{-d}^{\eta} \rho u \,\mathrm{d}z}, \tag{2.18}$$

$$S = \overline{\int_{-d}^{\eta} (p+\rho u^2)\,\mathrm{d}z}, \tag{2.19}$$

$$E = \overline{\int_{-d}^{\eta} (\tfrac{1}{2}\rho u_i^2+\rho g z)\,\mathrm{d}z}, \quad u_i^2 = u^2+w^2+v^2, \qquad (2.20), (2.21)$$

$$F = \overline{\int_{-d}^{\eta} (p+\tfrac{1}{2}\rho u_i^2+\rho g z)\,u\,\mathrm{d}z}. \tag{2.22}$$

The overbar is a time average over the carrier wave period T. Here, $\bar{\eta}$ is the setdown of the free surface, ρ is the fluid density. The average horizontal mass flux, horizontal momentum flux, and energy flux crossing the vertical are given by M, S, and F respectively. In equation (2.18) M is also interpreted as the time averaged momentum density, and E is the energy density. The term $\bar{\tau}$ is the time averaged horizontal shear stress at the boundaries of the channel and ϵ is the rate of energy dissipation unit mass.

The above equations are derived by integration of the differential, eulerian forms of the conservation equations from $-d$ to η and then time averaging over the carrier wave period. Also, use is made of the free surface and bottom boundary conditions (see, for example, Mei 1983).

Ultimately the total fluxes are found by integrating M, S, F over the entire packet period. The intermediate averages are made so that comparison with the results in the literature can be made and so motion at the packet scale is not filtered out. The total balance is done by integrating the equations over long time and over the distance between stations x_1 and x_2 where the flux is measured. For example, the total momentum balance becomes

$$\int_{t_1}^{t_2}\int_{x_1}^{x_2}\frac{\partial M}{\partial t}\,\mathrm{d}x\,\mathrm{d}t+\int_{t_1}^{t_2}\int_{x_1}^{x_2}\frac{\partial S}{\partial x}\,\mathrm{d}x\,\mathrm{d}t = \int_{t_1}^{t_2}\int_{x_1}^{x_2}\bar{\tau}_x\,\mathrm{d}x\,\mathrm{d}t, \tag{2.23}$$

then

$$\int_{x_1}^{x_2} M_{t_2}\,\mathrm{d}x-\int_{x_1}^{x_2} M_{t_1}\,\mathrm{d}x = -\int_{t_1}^{t_2} S_{x_2}\,\mathrm{d}t+\int_{t_1}^{t_2} S_{x_1}\,\mathrm{d}t+\int_{t_1}^{t_2}\int_{x_1}^{x_2}\bar{\tau}_x\,\mathrm{d}x\,\mathrm{d}t \tag{2.24}$$

giving,

$$\underline{\delta M} = -\overline{\overline{\Delta S}}+\underline{\overline{\overline{\tau}}} \tag{2.25}$$

where here the double overbar is a long time integration and the underbar is a space integration, and δ and Δ are difference operators in time and space respectively. Likewise for mass and energy, the total balance becomes

$$\rho(\delta\underline{\bar{\eta}}) = -\overline{\overline{\Delta\eta}}, \tag{2.26}$$

$$\underline{\delta E} = -\overline{\overline{\Delta F}}-\rho\,\underline{\overline{\overline{\int_{-d}^{\eta}\epsilon\,\mathrm{d}z}}}. \tag{2.27}$$

To experimentally determine the fluxes, it is necessary to measure the velocities $u(x,z,t)$, $w(x,z,t)$ and the pressure $p(x,z,t)$ simultaneously all along the verticals x_1 and x_2 and also measure the instantaneous free surface elevation. Alternatively, one may derive the pressure by use of the vertical momentum equation. Gradients in x and y are required, which can only be determined with measurements along two closely spaced vertical lines. These measurements are, in principle, possible using two scanning laser Doppler anemometers. However, there is a limitation on the sampling rate as well as equipment cost considerations. The approach used in these experiments is to estimate the fluxes by measuring the free surface displacement only. In this way a great number of repeats and packet types can be measured for their losses due to breaking with only two wave gauges. (Note that the momentum and energy density can only be measured by velocity measurements at grid points throughout the control volume and will be discussed in §5.) This flux estimation is possible, because at these stations, x_1 and x_2, the fluid motion contains only surface wave components. Also, the carrier wave steepness is $ak = \epsilon = 0.25$ (the symbol ϵ is used to represent wave slope and dissipation rate; however, we do not anticipate any confusion on the part of the readers) and the steepness of the packet envelope is of order ϵ^2 so that a weakly nonlinear wave theory can be used to predict the subsurface velocity and pressure field from the measured surface displacement.

The flux terms and densities shown above will generally contain contributions from the carrier waves, and also from the nonlinearly forced wave travelling with the group. The flux terms have been derived to second order in wave slope by Whitham (1962) and Longuet-Higgins & Stewart (1961, 1962, 1964) for the case of a slowly varying wave group of steepness $(ak)^2$. Mei (1983) treats the case where the wave amplitude is varying more rapidly in space. At locations far upstream and downstream of breaking the slowly varying assumption is valid and relatively small errors (of a few percent, see §3.2) result from using the second-order estimate for the momentum flux and energy flux. Closer to breaking, the higher-order terms become appreciable, and it is of interest to determine the form of these corrections. The details of this analysis are given in Rapp (1986) and summarized in Appendix A.

3. SURFACE DISPLACEMENT MEASUREMENTS OF BREAKING WAVE PACKETS

3.1. *General observations, time series and photographs*

Measurements of the free surface displacement are used to estimate the momentum and energy fluxes due to waves propagating down the channel. In this way many wave conditions are quickly measured with only a few instruments. The results presented in this chapter are all based on measurements of surface displacement made at various stations along the length of the channel.

The wave packets generated at the paddle were composed of short waves followed by long waves as shown in figure 6. As the group propagates down the tank, the length and period of the group decrease to a minimum near the predicted focal point, $k_c(x-x_b) = 0$, and disperse downstream. At the focal point, linear theory predicts the packet period to be $T = 2/\Delta f$, and the number of waves in the packet as $Tf_c = 2f_c/\Delta f$. This equals 2.8 waves for the case of $\Delta f/f_c = 0.73$, which approximates what is observed. For the packet in this particular figure, the conditions are such that a plunging breaker occurs between $k_c(x-x_b) = -5$ and 0, which explains the sudden drop in the wave amplitude.

While ak_c was increased (keeping $\Delta f/f_c$ and $x_b k_c$ fixed), the group went from non-breaking to a slight spilling, occurring approximately one wavelength downstream of x_b. Qualitatively, we define a non-breaking wave as one where the free surface remains smooth as the wave

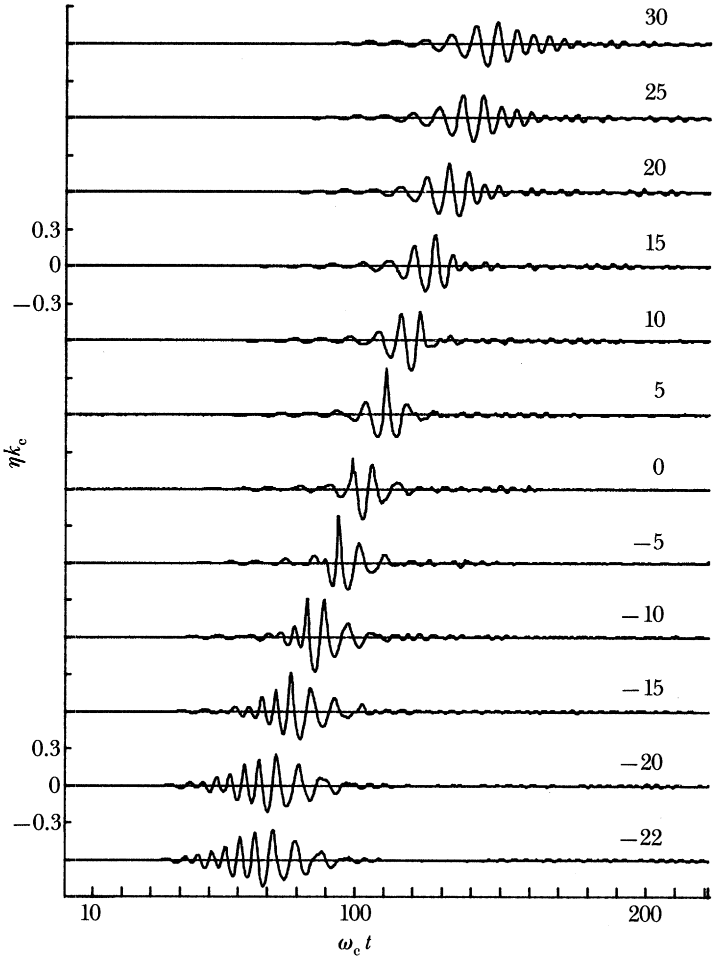

FIGURE 6. Time history of surface displacement at various distances from the theoretical energy focal point, x_b. Wave group parameters $f_c = 0.88$ Hz, $ak = 0.352$, $\Delta f/f_c = 0.73$, $x_b k_c = 27.4$. A single plunging wave was observed between $k_c(x-x_b) = -5$ and 0. The numbers on the graph are values of $k_c(x-x)$.

propagates through the packet envelope. A slight spilling wave is one where fluid appears to break out of the free surface. This is always initiated just ahead of the crest of the wave. More discussion will be given on a definition of breaking. This critical value at incipient breaking, $ak_c = 0.25$, varied little between various packets and scales. As ak_c was increased further, spilling was also triggered upstream near x_b. This breaking became more energetic with increasing ak_c, whereas spilling at the original location was no longer observed. Apparently energy is dissipated in the upstream breaking event so the energy in the packet is below a critical level downstream. At a value of $ak_c \approx 0.3$ only one spilling breaker was produced near x_b. A further increase of ak_c triggered breaking also one wavelength upstream. At $ak_c \approx 0.39$ only one plunging breaker was observed at this upstream location. At intermediate values of ak_c, two or three breakers were observed spaced roughly one wavelength apart and at a period of twice the carrier wave period. This periodicity is well known and has been observed in the field (Donelan *et al.* 1972).

The deviation in the breaking location from that predicted by linear theory may be attributed to nonlinear effects, which become important as the amplitude is increased. This

PHILOSOPHICAL TRANSACTIONS OF THE ROYAL SOCIETY A MATHEMATICAL, PHYSICAL & ENGINEERING SCIENCES

effect can be seen in figure 7 which shows details of the packet at closely spaced locations around breaking. The spilling case shows a relatively symmetric packet envelope with breaking occurring near the peak of the packet. The plunging breaking packet, one wavelength upstream, shows a forward skewed envelope and breaking on the envelope's steep front face. The carrier waves cannot sustain the rapid change in amplitude as they propagate through the steep envelope and thus breaking results.

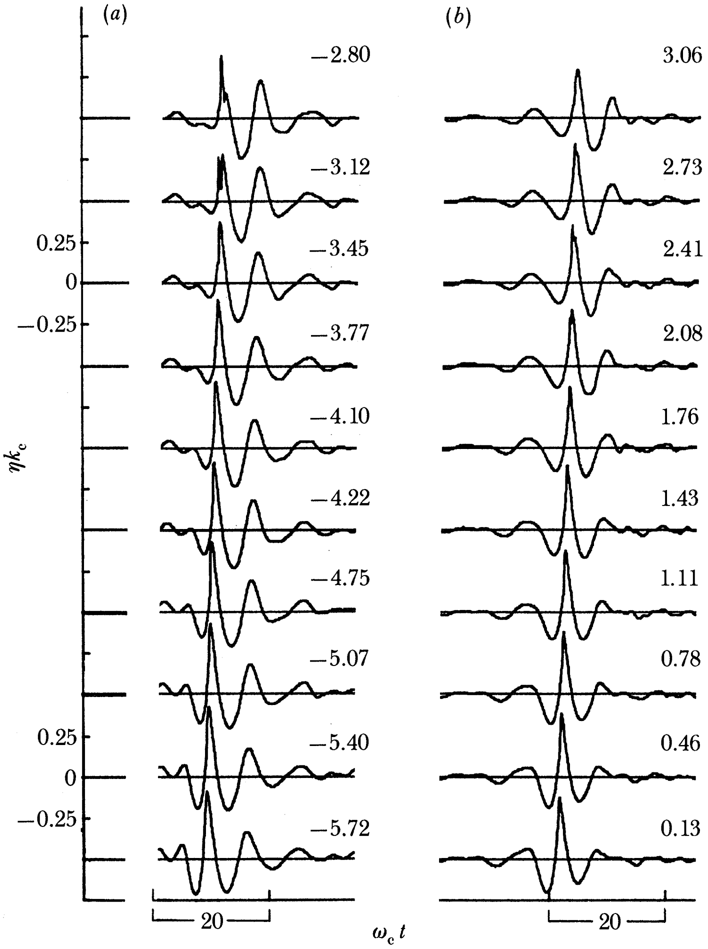

FIGURE 7. Detail of surface displacement time history around breaking. $f_c = 0.88$ Hz, $\Delta f/f_c = 0.73$, $x_b k_c = 27.4$. (*a*) Plunging $ak_c = 0.352$, (*b*) spilling $ak_c = 0.278$. The numbers on the graphs are values of $k_c(x-x_b)$.

The temporal evolution of breaking in two space coordinates is shown in a series of photographs in figures 8 and 9 (plates 1 and 2). Each frame represents a separate run of the wave group where the camera and flash unit were triggered at increasingly longer times in 0.05 s increments. Time is referenced from the paddle startup and can be compared directly with t_b, the theoretical time of breaking (20.2 s in this scale with $f_c = 0.88$ Hz centre frequency). The repeatability of the breaking can be seen in figure 10 at 17.0 s, which shows two separate runs. We estimate the horizontal variability in the surface displacement to be 1–2 cm between repeats when comparing the same time step. The variability in the time of jet impact on the free surface is 0.01 s after 17 s from paddle startup.

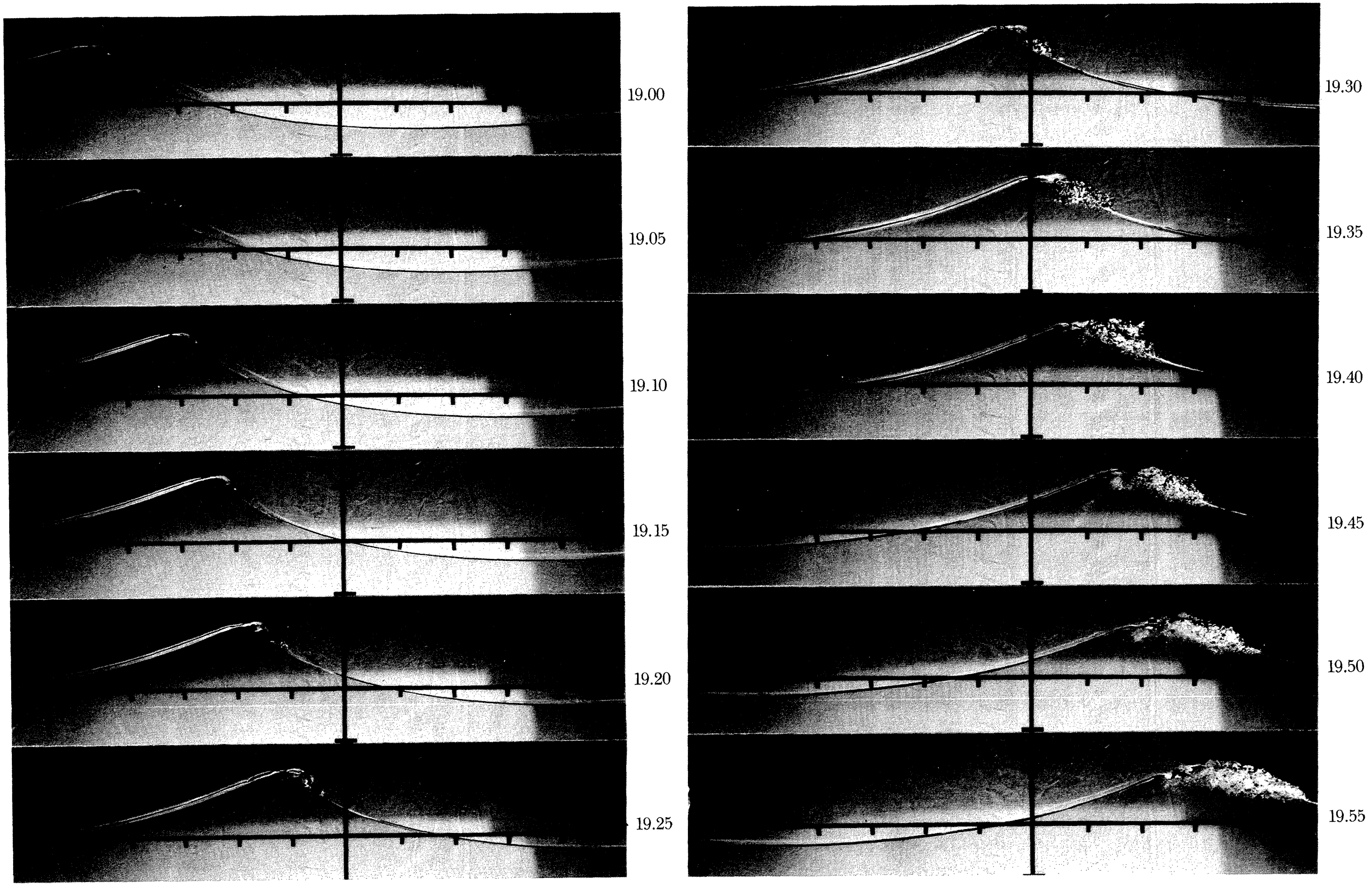

FIGURE 8. Photographs of a single spilling wave for $f_c = 0.88$ Hz $ak_c = 0.278$, $\Delta f/f_c = 0.73$, and $x_b k_c = 27.4$. Tick marks are at 10 cm intervals and times (in seconds) at right are referenced from paddle start.

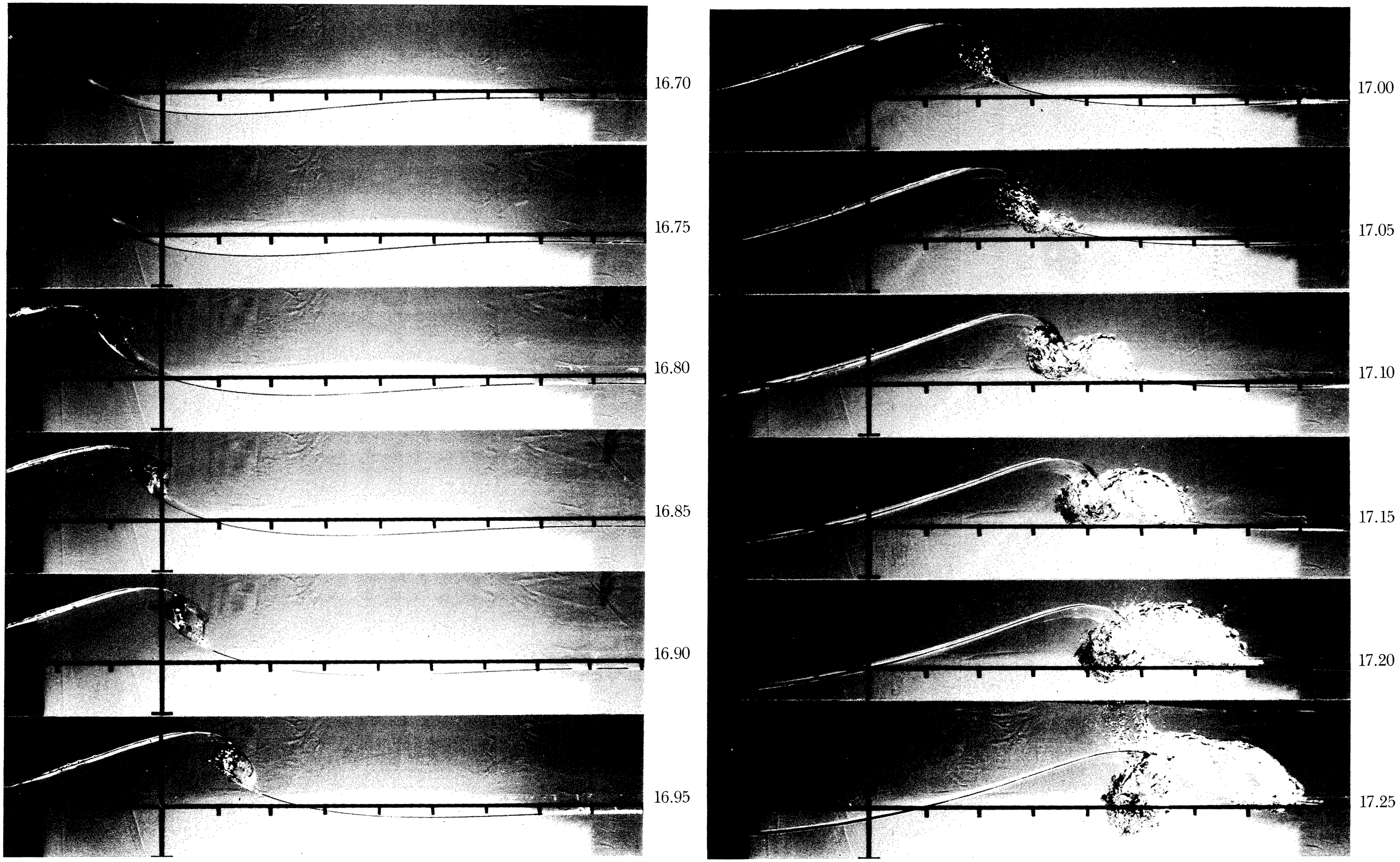

FIGURE 9. Photographs of a single plunging wave for $f_c = 0.88$ Hz $ak_c = 0.352$, $\Delta f/f_c = 0.73$, and $x_b k_c = 27.4$. Tick marks are at 10 cm intervals and times (in seconds) at right are referenced from paddle start.

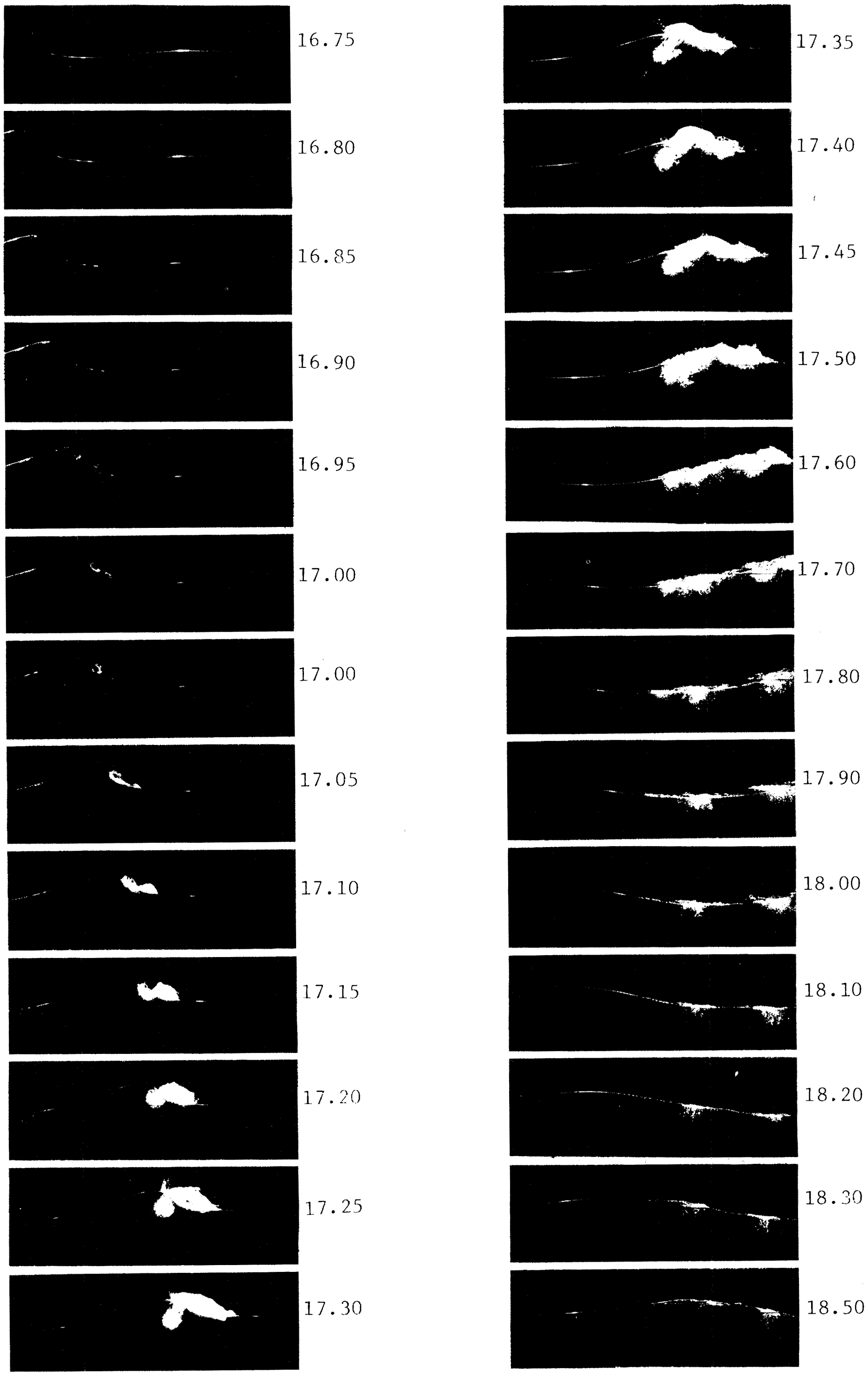

FIGURE 10. Photographs of a single plunging wave for $f_c = 0.88$ Hz $ak_c = 0.352$, $\Delta f/f_c = 0.73$, and $x_b k_c = 27.4$ showing generation and decay of bubble cloud. Times (in seconds) at right are referenced from paddle startup.

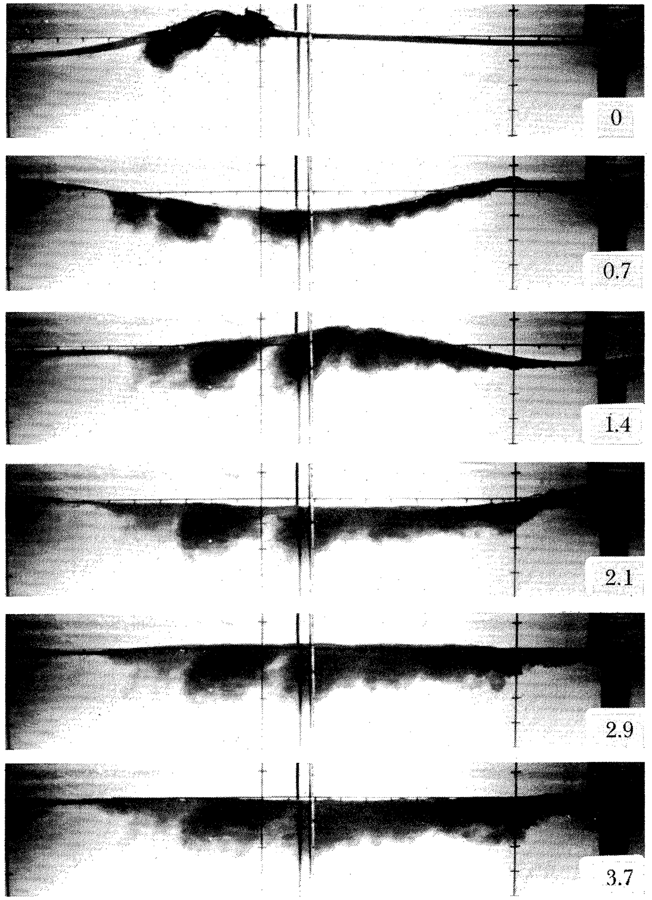

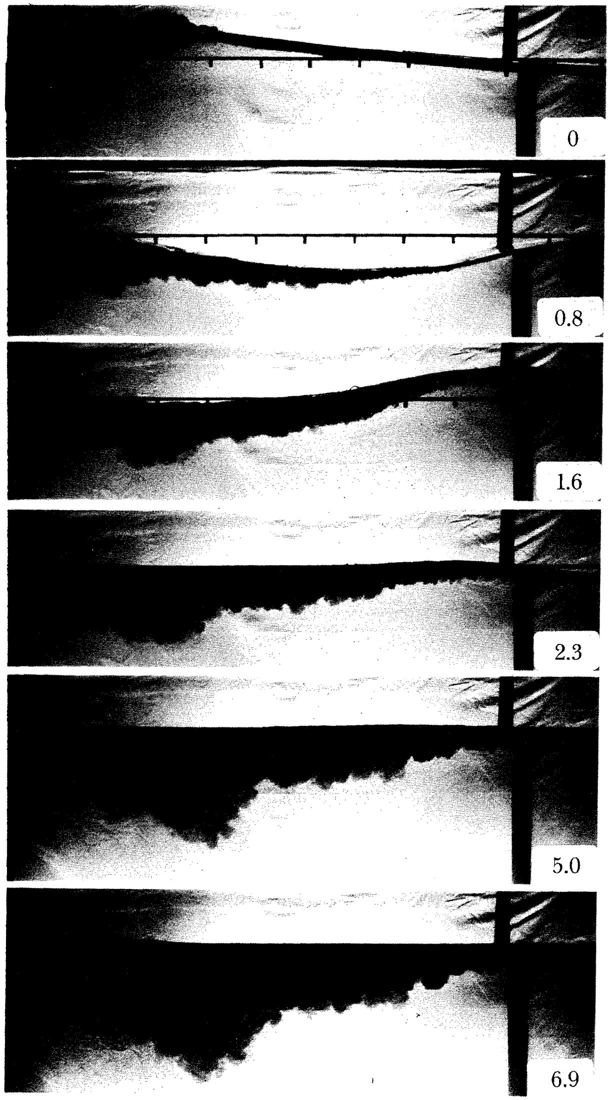

FIGURE 29 (left). Photographs of dye mixing under a plunging breaker for $f_c = 0.88$ Hz, $ak_c = 0.352$, $\Delta f/f_c = 0.73$, and $x_b k_c = 27.4$. Tick marks are 10 cm intervals. Numbers at right are elapsed times in seconds from top frame.

FIGURE 30 (right). Photographs of dye mixing under a spilling breaker for $f_c = 0.88$ Hz, $ak_c = 0.278$, $\Delta f/f_c = 0.73$, and $x_b k_c = 27.4$. Tick marks are 10 cm intervals. Numbers at right are elapsed times in seconds from top frame.

The large-scale single spilling case of $f_c = 0.88$ Hz, $ak_c = 0.278$, $\Delta f/f_c = 0.73$, and $x_b k_c = 27.4$ (figure 8) shows breaking occurring near the predicted location, x_b, but with the breaking evolving over a distance of almost one wavelength. The wave amplitude, and slope fore and aft, are continuously varying in this unsteady process, making a definition of breaking based on one of these variables ambiguous. As the wave approaches breaking, its profile becomes asymmetric with a steeper front face. The free surface breaks up as fluid appears to erupt from a point just forward of the crest and air is entrained forming bubbles. Note that breaking occurs first at the walls, leading the centre of the wave by less than 0.5 cm. The front slope, locally at the crest, reaches a maximum of 90° to the horizontal at $t = 19.25$ s. The region of entrained air grows forward and in depth down the front face of the wave.

This bubbly region looks qualitatively like the model of an accelerating turbulent gravity current (Longuet-Higgins & Turner 1974). However, their model assumes a steady underlying wave with a constant front slope, whereas these photographs show the front slope to be decreasing during the breaking process.

The same wave packet, but with the amplitude increased to $ak_c = 0.352$ resulting in a single plunging wave, is shown in figure 9. The wave starts breaking one wavelength upstream and two wave periods before the spilling wave. The wave is strongly asymmetric about the vertical with the front face going past the vertical as a well defined jet is formed. Again the fluid at the walls leads the centre section. The jet encloses a pocket of air and touches down on the forward face forcing up a secondary jet. Two regions of bubbles are generated which are carried down in depth by the next passing wave trough. (These multiple jets appear to be similar to the phenomena described by Peregrine (1983).) The evolution of this wave is shown for a longer time in figure 10, plate 3. Bubbles persist longer than two wave-periods after breaking.

The problem of defining a unique breaking time or location is evident from these photographs. For the plunging wave, the region from where the wave front becomes vertical to where the jet impacts the free surface spans a length of 40 cm or $0.2\lambda_c$ (where λ_c is the wavelength computed from the centre frequency using the finite depth dispersion relation). The corresponding time of breaking may vary over $0.2\,T_c$, where T_c is the wave period. For the spilling wave, the horizontal span is somewhat less but still over 10 cm. To reduce any ambiguity, two points in the breaking process are defined for later reference. For the plunging wave, the time and location where the wave front becomes vertical will be defined as t_{sb}, x_{sb} and are defined by $t = 19.15$ in figure 8 for the spilling wave and by $t = 16.80$ in figure 9 for a plunging wave. A later time in the breaking process that will be referred to in §§4 and 5, is the point where significant air entrainment (or deformation of the lower surface by impact) has begun. We call this the time and location of observed breaking t_{ob}, x_{ob}. This corresponds to $t = 19.35$ (see figure 8) for the spilling case and $t = 17.05$ (figure 9) for plunging. These times and locations are summarized in table 1. Also listed are the theoretical time and location of breaking t_b, x_b specified in equation (2.3).

These photographs are intended to illustrate the qualitative features of the breaking waves that are analysed for their loss of momentum flux.

3.2. *The excess momentum flux*

Time histories of the surface displacement, $\eta(t)$, were measured at closely spaced intervals (10–25 cm) along the channel for wave packets where f_c, $\Delta f/f_c$, $x_b k_c$ and ak_c were systematically varied. From these measurements, the time integrated free surface displacement variance, $\overline{\overline{\eta^2}}$,

Table 1. Definitions of breaking times and locations

(Refer to figures 8 and 9 for wave profiles. x_b is the theoretical break point or focal point. x_{sb} is the start of breaking defined by profile at $t = 19.15$ s figure 8 spill, $t = 16.80$ s figure 9 plunge. x_{ob} is the start of significant air entrainment defined by profile at $t = 19.35$ figure 8 spill, $t = 17.05$ figure 9 plunge. We call this the time of observed breaking.)

plunge	$f_c = 0.88$ Hz	$x_b = 8.46$ m	$t_b = 20.5$ s
	$ak_c = 0.352$	$x_{sb} = 6.9$ m	$t_{sb} = 16.80$ s
		$x_{ob} = 7.3$ m	$t_{ob} = 17.05$ s
spill	$f_c = 0.88$ Hz	$x_b = 8.46$ m	$t_b = 20.5$ s
	$ak_c = 0.278$	$x_{sb} = 8.8$ m	$t_{sb} = 19.15$ s
		$x_{ob} = 9.1$ m	$t_{ob} = 19.35$ s

was computed at each x location. The averaging time for computing the variance was typically 40 or 80 s. The computed quantity is defined as:

$$\overline{\overline{\eta^2}} = \int_{t_1}^{t_2} \overline{\eta^2}\,\mathrm{d}t = \int_{t_1}^{t_2} \eta^2\,\mathrm{d}t, \tag{3.1}$$

where

$$\overline{\eta^2} = 1/T\int_0^T \eta^2\,\mathrm{d}t$$

and the carrier-wave period, T, is much shorter than $(t_2 - t_1)$. The double overbar denotes the long time integration, whereas the single overbar is an average over the carrier wave period.

As is shown in Appendix A, the time-integrated variance of the free surface displacement is approximately proportional to the time integrated excess momentum flux due to the carrier waves crossing this x location, where

$$\overline{\overline{S}} = \int_{t_1}^{t_2} \overline{S}\,\mathrm{d}t = \int_{t_1}^{t_2} \tfrac{1}{2}\rho g \overline{\eta^2}\left[1 + \frac{2kd}{\sinh 2kd}\right]\mathrm{d}t + O(\epsilon^4), \tag{3.2}$$

and ϵ is a measure of the wave slope.

Additional terms, proportional to the square of the envelope steepness and the fourth power of the carrier-wave steepness give higher-order corrections to this estimate of the excess momentum flux. Also, in shallow water, the momentum flux in the long forced-wave is a significant contribution to the total momentum flux, which is not accounted for in the estimate. These errors, of course, increase as the focal point is approached, and as the carrier-waves and envelope steepen.

For the purpose of estimating the momentum flux, the depth is assumed to be large (kd large) so that $2kd/\sinh(2kd)$ is nearly zero. Using the wavenumber of the packet centre frequency, this assumption is good for the scales tested. However, for the wave component with frequency at the lower end of the packet frequency band, kd is not large and the bottom is influential. Nevertheless, to remain consistent with the slowly varying packet assumptions, we have chosen to compute the momentum flux from the variance of the free surface displacement measurement and ignore the effect of depth in this computation. As is discussed in §5.4, this assumption may have led to errors in the momentum flux estimates. To account for depth requires the rather cumbersome process of doing a Fourier analysis of the measurements, which takes away from the simplicity of these experiments. The bottom also influences the circulation pattern set up in the water column after the packet has passed.

The assumption that $\overline{\overline{\eta^2}}$ is proportional to the integrated energy flux is also valid, except near the energy focal point. The integrated energy flux is given to second order by

$$\overline{\overline{F}} = \overline{\overline{E}}\,\overline{\overline{C}}_g, \tag{3.3}$$

where $E = \rho g \overline{\eta^2}$ is the local energy density at a particular x. Strictly, this is twice the potential energy flux and we assume kinetic and potential energy are equipartitioned at locations away from breaking.

In normalizing the energy flux by its value at an upstream reference station, x_0, two sources of error may result in setting

$$\overline{\overline{F}}/\overline{\overline{F}}_0 = \overline{\overline{\eta^2}}/\overline{\overline{\eta_0^2}}. \tag{3.4}$$

First, C_g is not constant along the channel; and second, the assumption of equipartition is not generally valid close to breaking. Quantitative estimates of these errors based on the measured data are given below.

Figure 11*a* shows the integrated variance computed by (3.1) against distance from the energy focal point or predicted breakpoint for a packet with $f = 1.08$ Hz, $\Delta f/f_c = 0.73$ and $x_b k_c = 27.4$ and three values of ak_c. In this case these amplitudes correspond to an incipient or near breaking packet ($ak_c = 0.256$), a single spill ($ak_c = 0.296$) and a single plunging wave ($ak_c = 0.388$). The variance is normalized by the variance at the upstream reference station $k_c(x - x_b) = -22$, which is approximately three wavelengths from breaking. The x-axis is normalized by k_c.

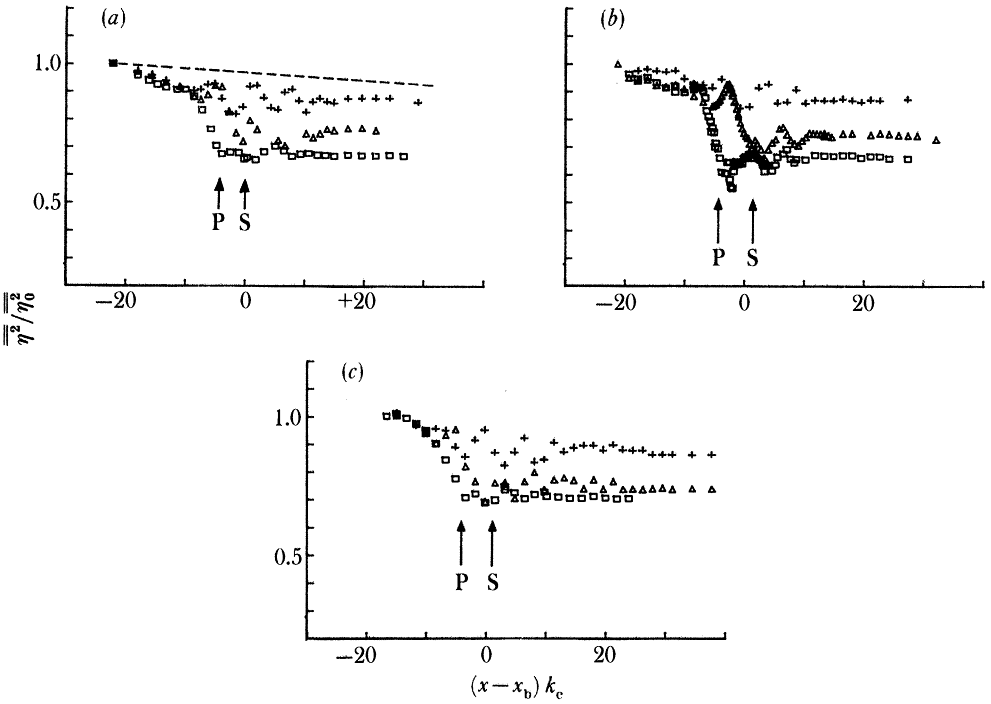

FIGURE 11. (*a*) Measurements of normalized surface displacement variance against distance from x_b ($x_b \equiv$ linear prediction of breakpoint or focal point). Wave packet variables are $f_c = 1.08$ Hz, $\Delta f/f_c = 0.73$, $x_b k_c = 27.4$. Incipient breaking $ak = 0.256$ (+), single spill $ak = 0.296$ (△), single plunge $ak = 0.388$ (□). P and S mark start of breaking, x_{sb} for plunge and spill (table 1). Broken line is theoretical dissipation due to tank side walls and bottom. (*b*) As for (*a*), except $f_c = 0.88$ Hz, incipient breaking (+), single spill (△), single plunge (□). (*c*) As for (*a*), except $f_c = 1.28$ Hz, incipient breaking $ak = 0.264$ (+); single spill $ak = 0.319$ (△); single plunge $ak = 0.420$ (□).

Three distinct regions are evident. Upstream of the focal point, the variance decays almost linearly with x and at the same rate for all three values of ak_c. Viscous dissipation in the channel sidewall and bottom boundary layers is responsible for approximately one-half of this energy loss and is shown by the broken line (Rapp 1986). The corresponding loss of the momentum flux is due to the time-integrated shear stress at the channel boundaries. Because no other losses are expected in this region, it is believed that the additional decay is due to errors in neglecting higher-order terms in the estimates of S and F. At the upstream reference station, the packet contains roughly six waves making the envelope steepness of order $\frac{1}{6}\epsilon$, and giving errors in the momentum flux of $O(10^{-2})$. The steepness of the carrier waves at this location is approximately $ak = 0.25$. So the error due to the carrier wave steepness is approximately $\epsilon^2 = 0.06$. The forced wave velocity was estimated from mean velocity measurements described in §5, and found to be $u = -0.02C$, causing an error of $O(10^{-2})$. These errors increase as the focal point is approached and are of the correct magnitude to account for the larger than expected slope of $\overline{\overline{\eta^2}}$ with x. A detailed discussion of these errors may be found in Rapp (1986).

As breaking is approached, the incipient breaking case shows oscillations in the variance of magnitude $0.10\overline{\overline{\eta_0^2}}$ occurring at intervals equal to one carrier wavelength. As the measured set-up of the mean water level is negligible, the true momentum flux and energy flux should follow the broken line in figure 11a, meaning that again the discrepancy is due to the errors in the estimate. Plots of η against time show that these oscillations are correlated with the phase of the carrier wave in relation to the envelope. A minimum in the variance corresponds to the time history of $k_c(x-x_b) = 4.4$ in figure 12 where the carrier wave is at the peak of the envelope and very steep. The maximum corresponds to $k_c(x-x_b) = 0.9$ where the carrier waves are less steep. The difference in the carrier wave steepness error terms between waves at these two stations is

$$\epsilon_a^2 - \epsilon_b^2 = 0.4^2 - 0.3^2 = 0.07. \tag{3.5}$$

The envelope steepness may also oscillate in this manner with comparable errors, which again leads to errors of the magnitude observed in the data. For the energy flux it may be expected

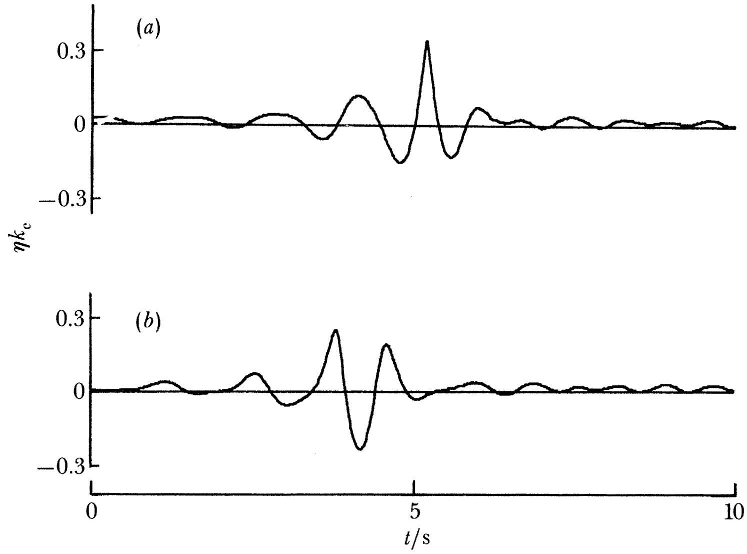

FIGURE 12. Wave packet time history corresponding to local maximum (bottom) and minimum (top) of $\overline{\overline{\eta^2}}$ against x curve, figure 11a. $f_c = 1.08$ Hz, $ak_c = 0.256$ incipient breaking. $k_c(x-x_b) = 4.4$ (a), 0.9 (b).

that the ratio of kinetic to potential energy is greater in the steeper wave of figure 12*a* than in figure 12*b* which may explain the oscillation. Also, there is no reason to believe that the group velocity, C_g, of the wave field is constant in the breaking region. The above discussion is intended to give possible explanations, and is not meant as a complete verification of these features.

The computed variance of the two breaking-wave cases, spilling and plunging, begins a steep drop approximately one-half wavelength upstream of the location where breaking starts, x_{sb}. This is where the front face of the plunging wave is vertical (figure 9, $t = 16.8$ s) and for the spilling wave it corresponds to $t = 19.15$ s in figure 8. This drop in the variance, upstream of where energy dissipation due to breaking is expected, further supports the fact that potential energy is going into the kinetic energy just as the wave steepens (at breaking). In the breaking waves, however, energy and momentum flux is lost from the carrier waves so the variance does not recover up to the non-breaking value. The oscillations are still present downstream for a few wavelengths. The gradient of the loss appears to be equal for all three cases, approximately 25% per wavelength; however, the drop persists over a longer distance for spilling and an even longer distance for plunging (about one wavelength), resulting in lower downstream levels of the variance. Beginning at the start of breaking x_{sb}, and for approximately one wavelength downstream, where the fluid is entrained with air, the surface displacement gauges may not be expected to give reliable measurements. However, the scatter in the data is small, so this does not appear to be a large problem.

Downstream of breaking, the packet disperses and the waves again become more linear as the slope decreases. The oscillations have died out leaving an almost constant level of potential energy with x. The difference in these levels from the non-breaking packet may be attributed completely to wave breaking. The results of similar measurements for two other scales of waves of centre frequencies $f_c = 0.88$ Hz and $f_c = 1.28$ Hz (figures 11*b*, *c*) show good agreement between scales using the wavenumber of the centre frequency to scale x. Notice the good agreement between scales in the location where the variance steeply drops. The agreement is seen more clearly in figure 13 where the three scales are plotted together for each level of breaking. The downstream levels of the surface displacement variance also show good agreement between scales. Note, however, that these results compare packets where the breaking was incipient, a single spill, and a single plunge; and there is a small deviation from scale to scale in the values of ak_c that correspond to these qualitative classifications (see figure 13).

Similar measurements made for packets where the bandwidth $\Delta f/f_c$ was varied show the downstream level of the variance is still very well correlated with ak_c even though the loss rate varied between packets. It is possible, then, to treat the breaking regions as a 'black box' and measure input and output variance to establish the loss due to the breaking packet. The fact that the packet breaks more than once is not important in this type of analysis.

The effect of varying the non-dimensional breaking location, $x_b k_c$, was found to be small. The case of $ak_c = 0.3$ is shown in figure 14. The input and output levels of the variance show essentially no change as $x_b k_c$ is varied from 27.4–66.0. As the breaking was moved farther from the paddle, however, it became more difficult to obtain a single breaking wave and the loss was spread over several wavelengths, as indicated by the shallower slope of the variance in the figure. This can be attributed to finite depth dispersion effects and nonlinearity causing phase mismatch between components as the focal point is moved farther from the paddle.

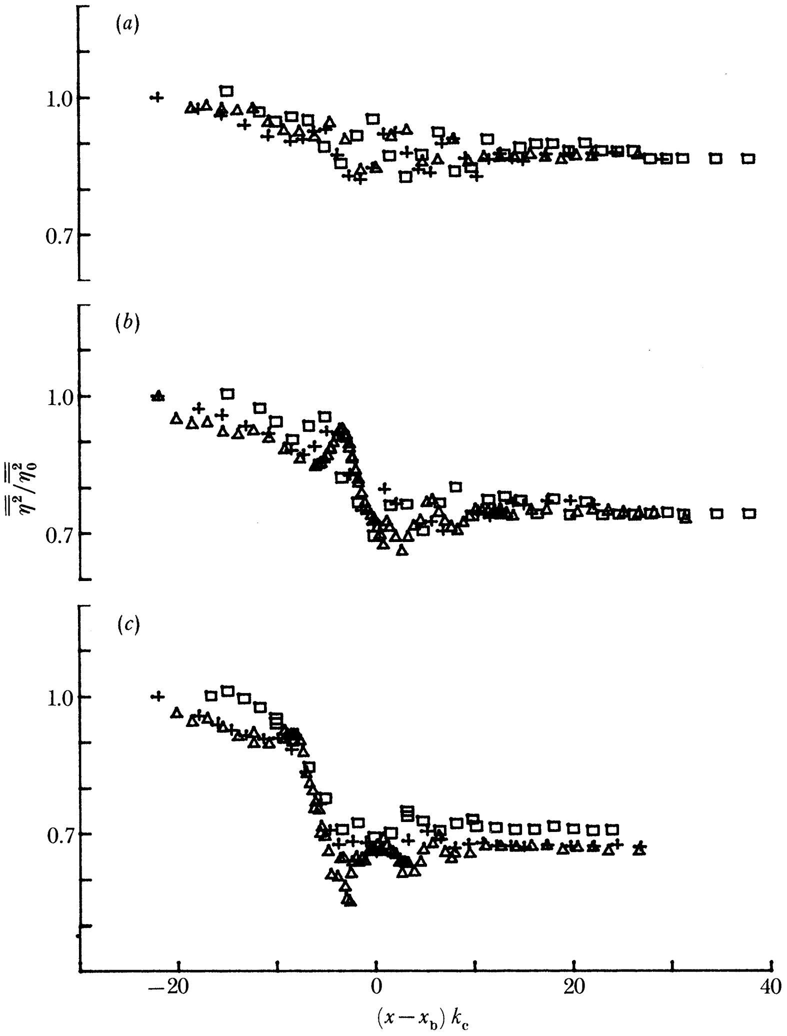

FIGURE 13. Surface displacement variance against distance from breaking, x_b. A comparison between scales or packet centre frequencies. f_c = 1.28 Hz (□), 1.08 Hz (+), 0.88 Hz (△). For $\Delta f/f_c = 0.73$, $x_b x_c = 27.4$. (*a*) Incipient, $ak_c (0.25 \rightarrow 0.26)$; (*b*) single spill, ak_c $(0.28 \rightarrow 0.32)$; (*c*) single plunge, ak_c $(0.35 \rightarrow 0.42)$.

3.3. *Loss of excess momentum flux due to breaking*

At locations greater than three wavelengths from the theoretical break point, x_b, the error in using the surface displacement variance in estimating the momentum flux was shown to be approximately 5%. In addition, it is expected that the group velocity C_g is the same for the packet far upstream and downstream (cf. figure 6), so the normalization used in the previous plots will cancel this multiplier in the energy flux equation. With these assumptions and the relatively small errors in mind, the normalized surface displacement variance at these reference stations away from breaking, will be used as a measure of the excess momentum flux. The loss of excess momentum flux will be defined as the difference between the upstream and downstream levels where the momentum flux is nearly constant in x. Viscous decay due to boundary layers can be subtracted out by referencing the incipient breaking case as the zero level. A similar argument can be made in interpreting the previous plots as the normalized loss of energy flux due to the carrier waves.

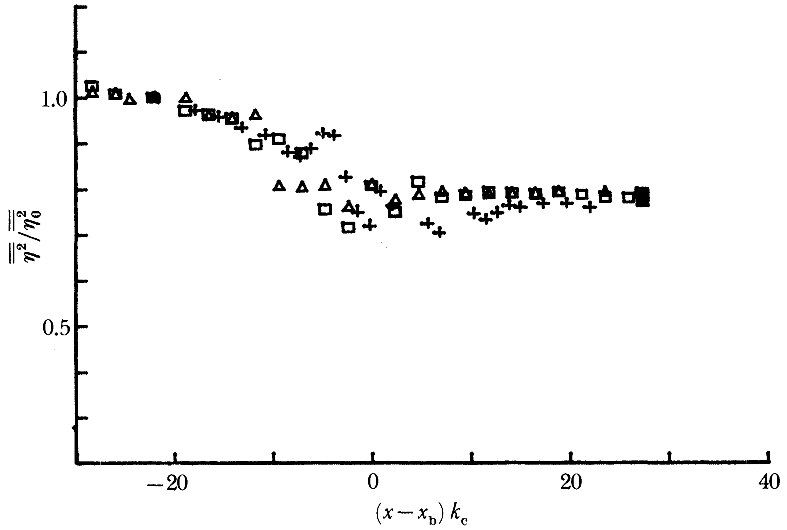

FIGURE 14. Surface displacement variance against distance from breaking, x_b, for variations in breaking location, $x_b k_c = 27.4$ (+), 47.1 (△), 66.0 (□); $f_c = 1.08$; $ak_c = 0.3$, $\Delta f/f_c = 0.73$.

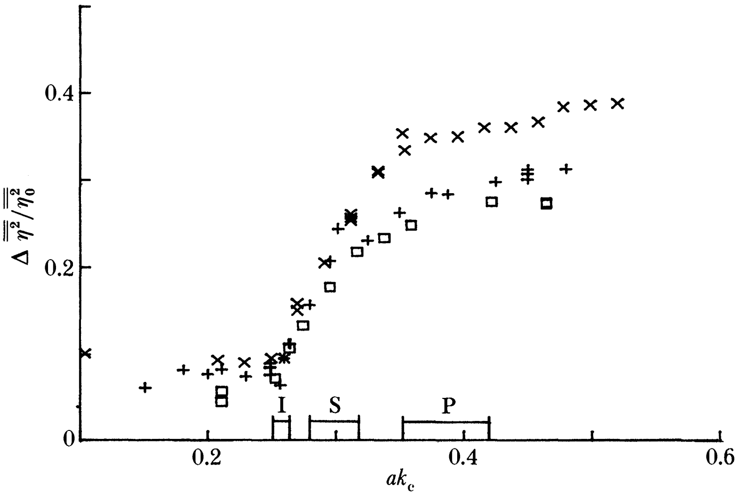

FIGURE 15. Loss of excess momentum flux as a function of the wave packet amplitude for three packet centre frequencies $f_c = 0.88$ Hz (*x*), 1.08 (+), 1.28 (□) and $\Delta f/f_c = 0.73$, $x_b k_c = 27.4$. Occurrence of incipient breaking, single spilling, and plunging are marked by I, S, P with variations between scales shown by horizontal bars.

A plot of these losses against the wave packet amplitude, ak_c, is shown in figure 15 for the three scales of wave packets. The loss is normalized by the measured variance at the upstream location. At amplitudes less than $ak_c = 0.25$ the loss is due completely to boundary layer dissipation and is in agreement with theory (6–8 % loss over eight wavelengths). At the critical value of $ak_c \approx 0.25$, the curve shows a sharp rise, which coincides with the value of ak_c where incipient breaking was observed to occur. Once this transition to breaking is passed, a relatively small increase in amplitude results in energetic breaking up to strong spilling with losses varying from 0–20 % referenced to the non-breaking case. Beyond this point, $ak_c \approx 0.3$, a larger increase in ak_c is required to obtain a plunging breaking wave but results in an additional momentum flux loss of only 5–10 %. The agreement between all three scales is good up to spilling and remains good for the two smaller scales of $f_c = 1.08$ Hz and $f_c = 1.28$ Hz packets beyond. The larger loss at the large scale, $f_c = 0.88$ Hz for high values of ak_c, cannot be explained. It was observed, however, that the plunging jet impinging on the free surface caused a secondary sheet of fluid to be ejected. This continued is a cascading effect. The non-dimensional horizontal extent of this process is greater at the largest scale, leading to the suggestion that surface tension effects, which are not considered here, are important for scaling the air entrainment. Larger, possibly full-scale, experiments are needed to resolve this question.

Variation in the packet bandwidth does not appear to strongly affect the overall loss of excess momentum flux, as can be seen in figure 16. This fact was also evident in the results of the previous section. The only exception to this is evident at amplitudes near the inception of breaking. The curve corresponding to $ak_c = 0.257$ varies by 10% over the range of packet bandwidths. This value of ak_c corresponds to incipient breaking for $\Delta f/f_c = 0.73$ where the curve is a minimum; however, it was observed that breaking was already occurring at higher and lower values of bandwidth resulting in these larger losses. This result points out two things: first that breaking inception is sensitive to changes in $\Delta f/f_c$ and also that small changes in ak_c quickly lead to losses of up to 10% of the initial momentum flux in the packet. Once ak_c is increased to 0.3, the bandwidth has little effect on the overall loss, however.

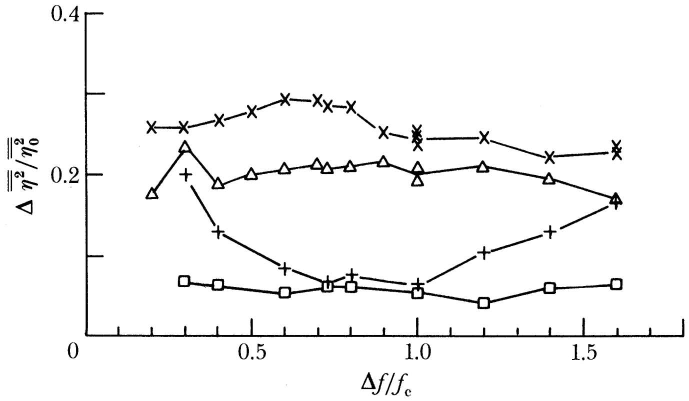

FIGURE 16. Loss of excess momentum flux against the wave packet bandwidth $\Delta f/f_c$ for four input wave amplitudes, $ak_c = 0.151$ (□), 0.257 (+), 0.296 (△), 0.388 (×) and $f_c = 1.08$. These correspond to a non-breaking packet, incipient breaking, a single spill, and a single plunging wave, respectively, for $f_c = 1.08$, $x_b k_c = 27.4$ and $\Delta f/f_c = 0.73$.

The slight plateau in the loss for $ak_c = 0.388$ around $\Delta f/f_c = 0.7$ indicates a slight 'tuning' effect in the breaking. This corresponds to a single plunging event whereas multiple breaking waves were observed at higher and lower values of $\Delta f/f_c$.

The weak dependence on $\Delta f/f_c$ can also be seen in figure 17 where the momentum flux loss is plotted against ak_c for five values of $\Delta f/f_c$. The shapes of the curves are all very similar. However, the sharp break in the curve at breaking inception $ak \approx 0.25$ is smoothed out as $\Delta f/f_c$ is increased or decreased from 0.7 and breaking inception was observed to occur at lower values of ak_c.

Similar plots are shown for measurements made of wave packets where the theoretical energy focal point x_b was varied (figures 18 and 19). These results show that the loss of excess momentum flux is also rather insensitive to changes in this parameter, $x_b k_c$, at wave amplitudes up to $ak_c = 0.3$. Where x_b is not too far from the paddle, the agreement at higher values of ak_c

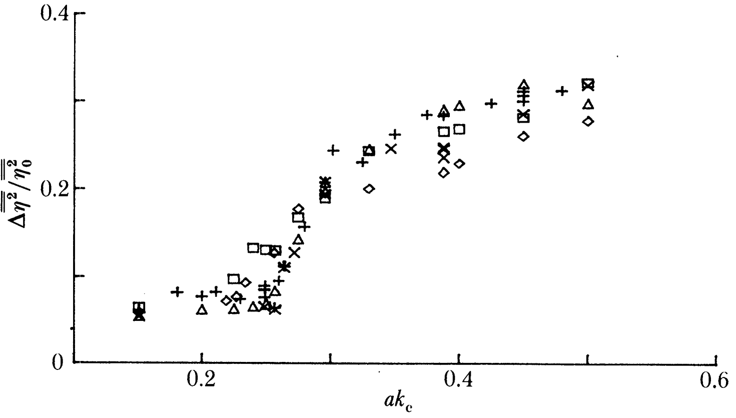

FIGURE 17. Loss of excess momentum flux against ak_c for five packet bandwidths, $\Delta f/f_c = 0.4$ (□), 0.6 (△), 0.73 (+), 1.0 (×), 1.4 (◇). Also, $f_c = 1.08$ Hz, $x_b k_c = 27.4$.

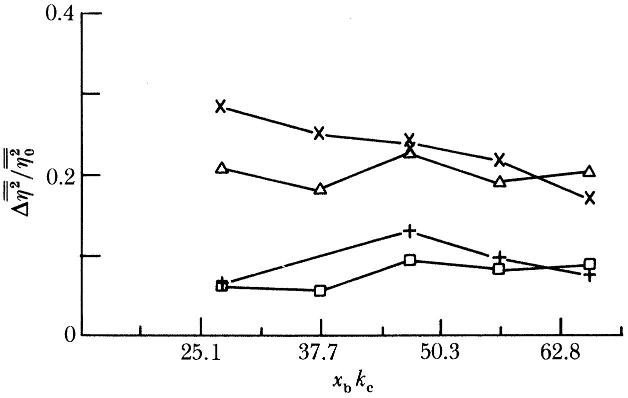

FIGURE 18. Loss of excess momentum flux as a function of the theoretical breaking location $x_b k_c$ for four values of wave amplitude $ak_c = 0.151$ (□), 0.257 (+), 0.296 (△), 0.338 (×). $f_c = 1.08$ Hz, $\Delta f/f_c = 0.73$.

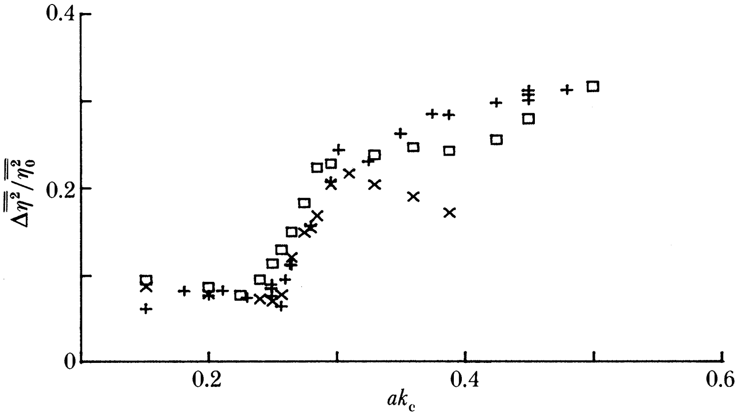

FIGURE 19. Loss of excess momentum flux against ak_c for three predicted breaking locations, $x_b k_c = 27.4$ (+), 47.1 (□), 66.0 (×). $f_c = 1.08$ Hz, $\Delta f/f_c = 0.73$.

is also good. As the breaking location is moved farther downstream, the energy focusing does not appear as good and the loss falls off as is shown in figure 19 for $x_b k_c = 66.0$. The larger propagation length could allow nonlinearity and certainly allows the finite depth effects to cause phase mismatch at this downstream location because the starting phases were computed assuming deep water. The curve of the momentum flux loss against ak_c is seen to retain its shape; even the agreement in the point of breaking inception is good.

3.4. *Local wave parameters at breaking and steepness at breaking*

Given the non-dimensional parameters that specify a particular wave packet before breaking, it is of interest to predict the geometry of the resultant wave at breaking and determine if these local parameters can be used to parametrize the breaking intensity or the momentum-flux loss. From observation there is a strong correlation between the type and strength of breaking (i.e. incipient breaking, spilling, plunging) and its normalized momentum-flux loss. (With practice, one could almost predict the momentum flux loss from visual observation alone.) The goal, then, is to quantify what is observed locally.

Measurements of the local spatial parameters at breaking were made from 16 mm films taken of the wave at breaking. The movie camera (Bolex H16 REX) was run at 64 frames per second. In addition, wave gauges were located at closely spaced intervals (12.5 cm) around breaking to obtain a coarse spatial profile of the wave to check against the films.

Breaking inception or incipient breaking describes the largest wave packet that, at no time during its evolution, ever breaks. The wave profile at the time when the crest of smallest radius of curvature is formed is measured for a_{sb}, λ, H, and L_f as defined in figure 20. This wave profile also corresponds to the maximum wave amplitude.

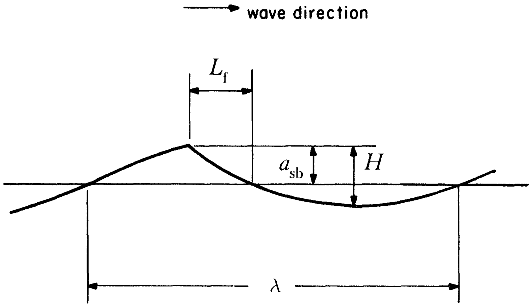

FIGURE 20. Definition sketch of wave geometry in space. $\alpha = a_{sb}/L_f$, $\beta = \pi H/\lambda$.

The input wave amplitude ak_c that was observed to cause incipient breaking is plotted against $\Delta f/f_c$ in figure 21. This value is almost constant for all bandwidths. The measured wave amplitude, a_{sb}, at incipient breaking, normalized by k_c, is also plotted. This parameter decreases with increasing bandwidth indicating that relatively low waves with low steepness are still near breaking. The measured steepness at breaking, H/λ, also decreases with increasing bandwidth. Another parameter, defined as the wave front steepness, $\alpha = a_{sb}/L_f$ (figure 21), is plotted. This parameter remains almost constant for all the incipient breaking cases, indicating that it gives a better indication of incipient breaking.

The same measurements are shown for packets that result in single spilling waves (figure 22). Again, the input wave amplitude, ak_c, causing a single spill remains approximately constant for all bandwidths; likewise, the locally measured amplitude decreases with increasing $\Delta f/f_c$. Here a_{sb} was measured at a profile where it was a maximum which corresponds to the start of breaking defined in §3.1. The measured front steepness of breaking starts out constant at low values of $\Delta f/f_c$, but varies greatly at larger bandwidths. From the films, it was observed that the front steepness varied throughout the breaking process and the actual measure of front

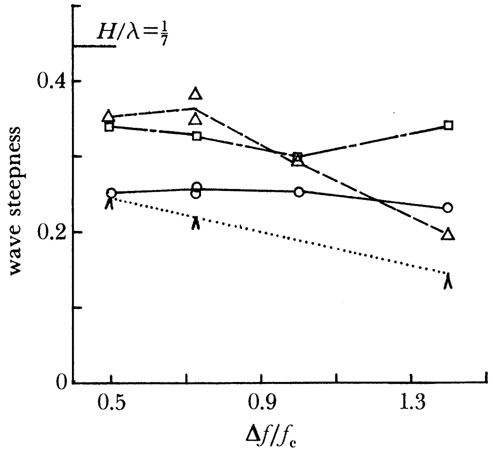

FIGURE 21. Spatial wave steepness measurements for incipient breaking. ak_c (○), $a_{sb}k_c$ (△), $\alpha = a_{sb}/L_f$ (□), $\beta = \pi H/\lambda (\wedge)$. Refer to figure 20.

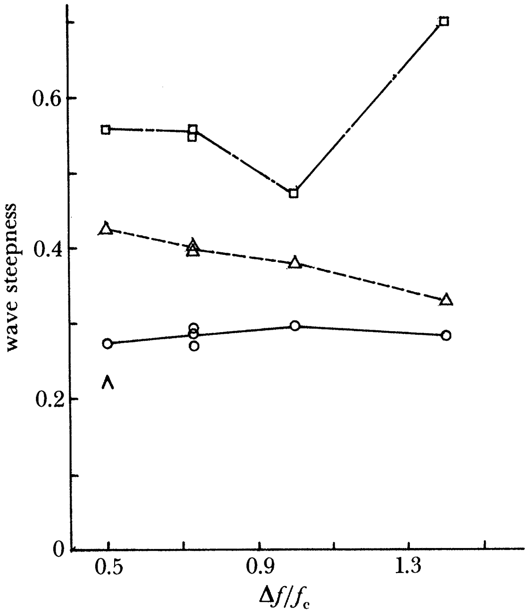

FIGURE 22. Spatial wave steepness measurements for spilling breaking as for figure 21.

steepness at breaking depends upon how the breakpoint is defined. Also, it is possible that the horizontal length, L_f, measured from the crest to the forward zero crossing is still too coarse to predict breaking, especially if there are short waves riding on long waves. Breaking is very localized at the crest. The plunging wave suffers the same problems in defining a front steepness.

Figure 23 shows that the front steepness parameter does a better job of predicting a unique type of breaking for the incipient case, but becomes less reliable as the front slope increases and the breaking becomes more vigorous. Figure 24 shows the poor correlation between the local wave amplitude and the wave packet input amplitude ak_c. Although ak_c is a good predictor of breaking, the local amplitude $a_{sb}k_c$ is not.

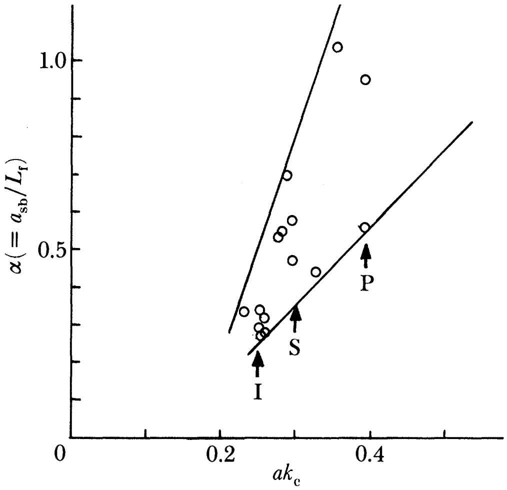

FIGURE 23. Correlation between input packet amplitude, ak_c, and front steepness α. Refer to figure 20. Incipient breaking waves, I; spilling, S; plunging, P.

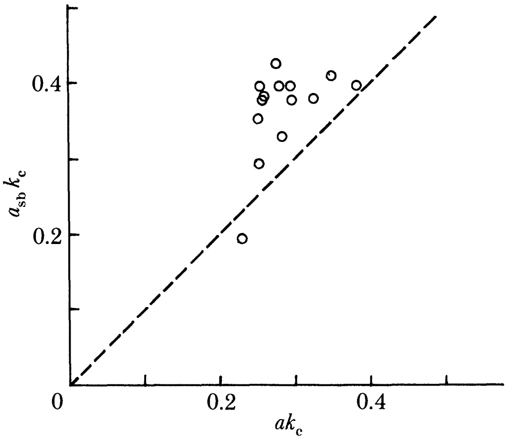

FIGURE 24. Correlation between input packet amplitude, ak_c and locally measured amplitude, $a_{sb} k_c$, for all intensities of breaking. Broken line is ideal linear superposition.

From these results, it appears that a 'snapshot' of the local geometry just before breaking is insufficient to predict spilling or plunging, but spatial derivative or rate of change of the steepness, for instance, maybe needed to better predict breaking. This finding is consistent with that of Van Dorn & Pazan (1975), where the wave growth rate was found to be important in predicting breaking.

3.5. *Evolution of the frequency spectrum*

The measurements of the surface displacement variance have provided a measurement of the loss of the momentum flux and energy flux from the carrier waves due to breaking. It is of interest to determine the form of this dissipation spectrum, that is, which frequencies are losing the most momentum flux. In this section the spectra of the surface displacement are shown as the packet converges and then disperses downstream.

A fast Fourier transform (FFT) was done over the packet, windowed to include the packet energy but exclude reflections. The window is smoothly brought to zero with cosine bells over the end 10% of the window. In the large scale case ($f_c = 0.88$ Hz) the window length is 23.5 s, 1175 data samples, sampled at 50 Hz frequency. The program adds zeros to do a 2048 point FFT. Only one realization at each x location was available, so smoothing was done by averaging over four adjacent spectral estimates, giving eight degrees of freedom. The spectrum over the input band of frequencies is deterministic so these spectral estimates do not have errors associated with stochastic processes.

The spectra for the large scale ($f_c = 0.88$ Hz) incipient breaking packet ($ak_c = 0.257$) are shown in figure 25. The momentum flux density, G, is normalized by $k_c^2 f_c$ and the frequency by f_c. The spectrum at the upstream reference station $k_c(x-x_b) = -22$ shows the 'top hat' input spectrum. Also evident is the energy in the second harmonic band. This spectrum is plotted as a dashed line in subsequent spectra for reference. As the packet evolves to the energy focal point, the spectrum loses its 'top hat' shape, and energy is spread to higher frequencies. Note that these are log plots and one order of magnitude is represented by one tick mark on the left margin, so the energy in the high frequencies has increased by almost ten times. The corresponding time history is the steep carrier wave at the energy focal point. Even though the wave is not breaking, the spectrum has changed significantly. Note also the growth of the forced wave at the low frequencies as the packet approaches breaking.

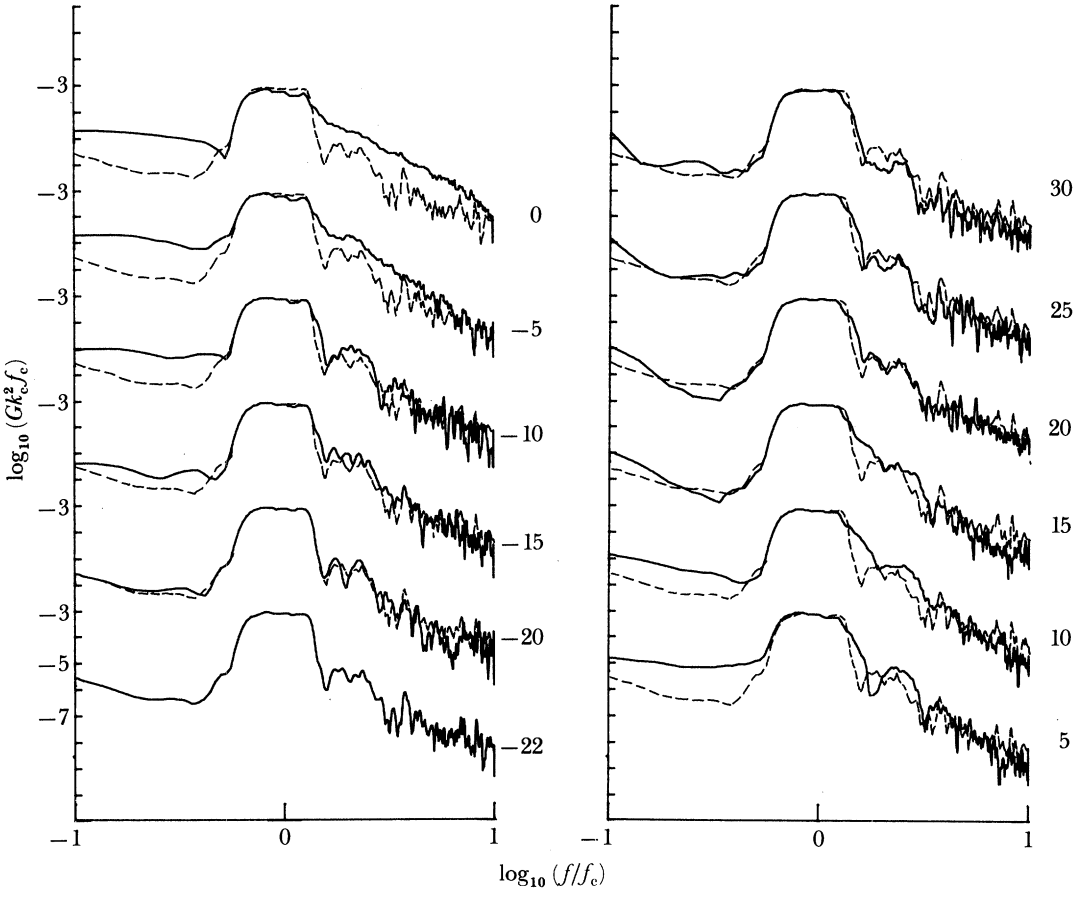

FIGURE 25. Spectra of incipient breaking wave packet. $f_c = 0.88$ Hz, $ak_c = 0.257$, $\Delta f/f_c = 0.73$, $x_b k_c = 27.4$. Dashed line is spectrum at reference station $k_c(x-x_b) = -22$. The numbers on the graphs are values $k_c(x-x_b)$.

As the packet disperses again downstream, the waves become less steep and the spectrum at $k_c(x-x_b) = 30$ returns to almost its initial 'top hat' shape. Note the slight loss at the higher end of the first harmonic band, and in the second harmonic band.

The plunging wave results are shown in figure 26. Here again, near the paddle the spectrum is very much like the theoretical input spectrum. The spectra evolve as for the non-breaking case, but here the packet is steepest at $k_c(x-x_b) = -5$. Breaking occurs between $k_c(x-x_b) = -5$ and 0, and the loss in the high frequency end of the first harmonic and in the second harmonic band between these stations is appreciable. The packet continues downstream, dispersing into linear waves but note the spectra far downstream. Essentially all the momentum flux loss from the packet (24 %) is lost from the high-frequency end of the first harmonic band. About a 90 % reduction is seen in the second harmonic band. A similar behaviour is observed for the spilling breaker (figure 27) but here only 10 % of the momentum flux is lost from the packet, but still comes from the high end of the first harmonic band of frequencies.

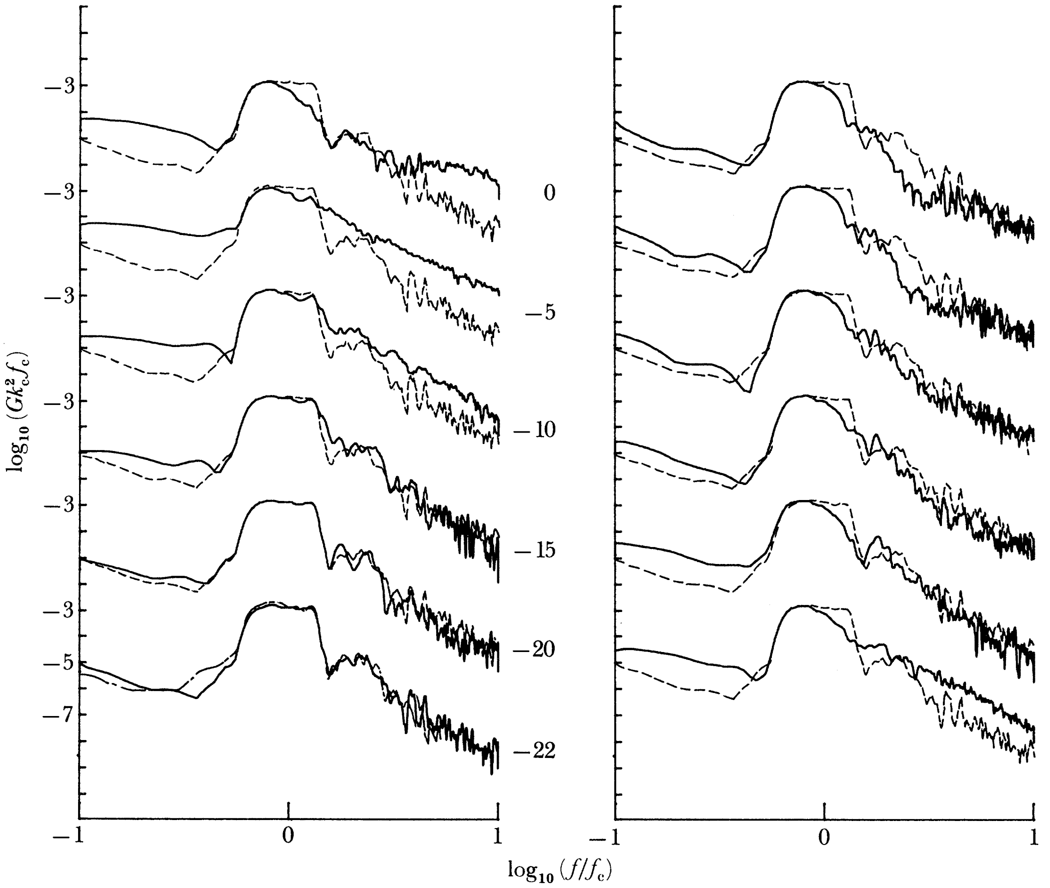

FIGURE 26. Spectra of plunging breaking wave packet. As for figure 25 except $ak_c = 0.352$. Broken line at $k_c(x-x_b) = -22$ is for small scale plunging $f_c = 1.28$ Hz, $ak_c = 0.420$. The numbers on the graphs are values of $k_c(x-x_b)$.

The scaling of this behaviour was verified where the small scale ($f_c = 1.28$) plunging ($ak_c = 0.420$) wave spectra was compared with the results of the large-scale case, and found to agree very well (figure 26). Thus it appears that the low frequency waves in all cases studied, propagate through breaking, even the intense plunging, without significant loss of energy. It

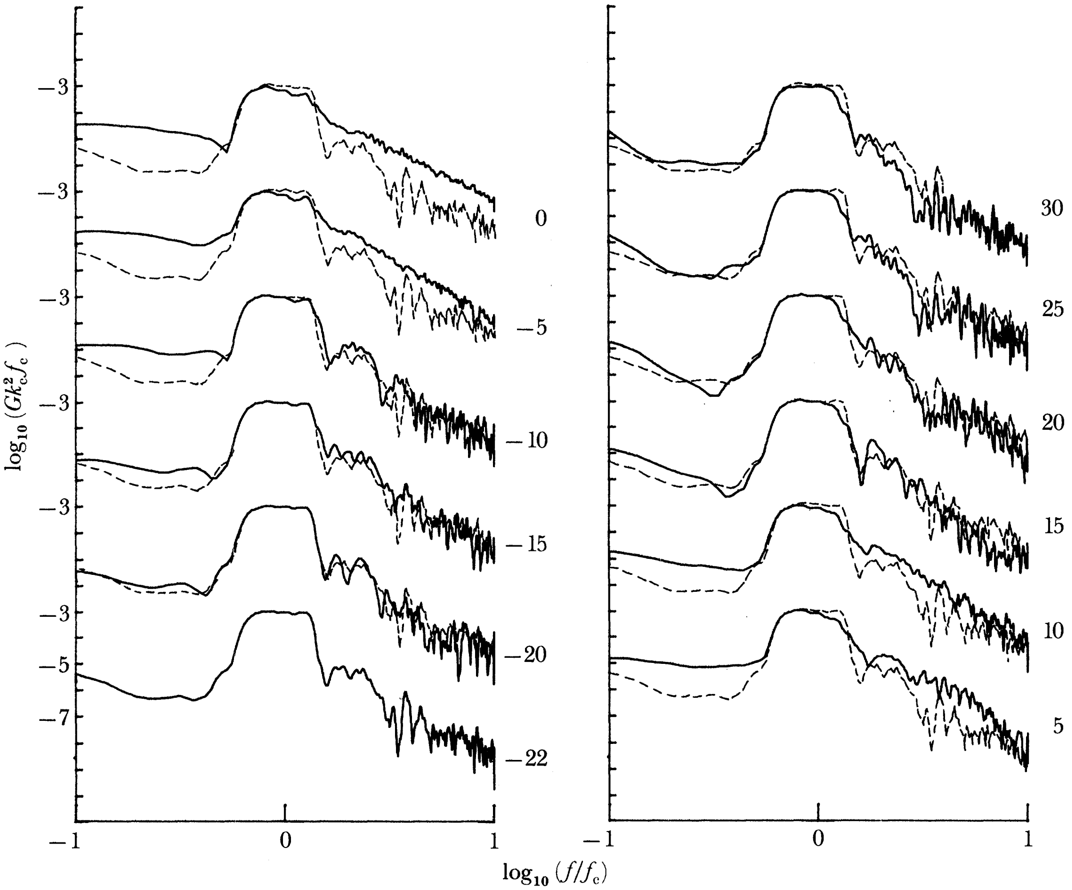

FIGURE 27. Spectra of spilling breaking wave packet. As for figure 25, except $ak_c = 0.278$. The numbers on the graphs are values of $k_c(x-x_b)$.

appears that high frequency waves are required to obtain the required wave steepness for ocean breaking.

In the course of these experiments, it was observed by eye that waves were radiated back upstream from the breaking location as a result of the more intense plunging breaking. It is reasonable to expect that the impact of the plunging jet into the free surface can radiate waves in both directions. Measurements of the free surface displacement throughout the channel were made to measure these waves. The spectra of the free surface after the packet had passed was computed by FFT methods. The FFT window of 2048 samples in 40.96 s was tapered with cosine bells at the end 10%. The data was sampled at 50 Hz. The spectra were smoothed as before. The resultant spectra for the large scale ($f_c = 0.88$ Hz) plunging ($ak_c = 0.352$) is shown in figure 28 as a solid line. The dashed line is for the incipient breaking wave packet ($ak_c = 0.257$). Note the obvious difference between the two cases in the energy around the second harmonic band, particularly for the locations upstream of breaking. A comparison with the spectra of the main packet shows that these radiated waves contain approximately 1% of the energy in the main packet. These data suggest, then, that second harmonic waves are reflected from the breaking region or generated there. Whether or not these waves are random or deterministic cannot be seen here. Results of the ensemble averaged surface displacement over ten repeats

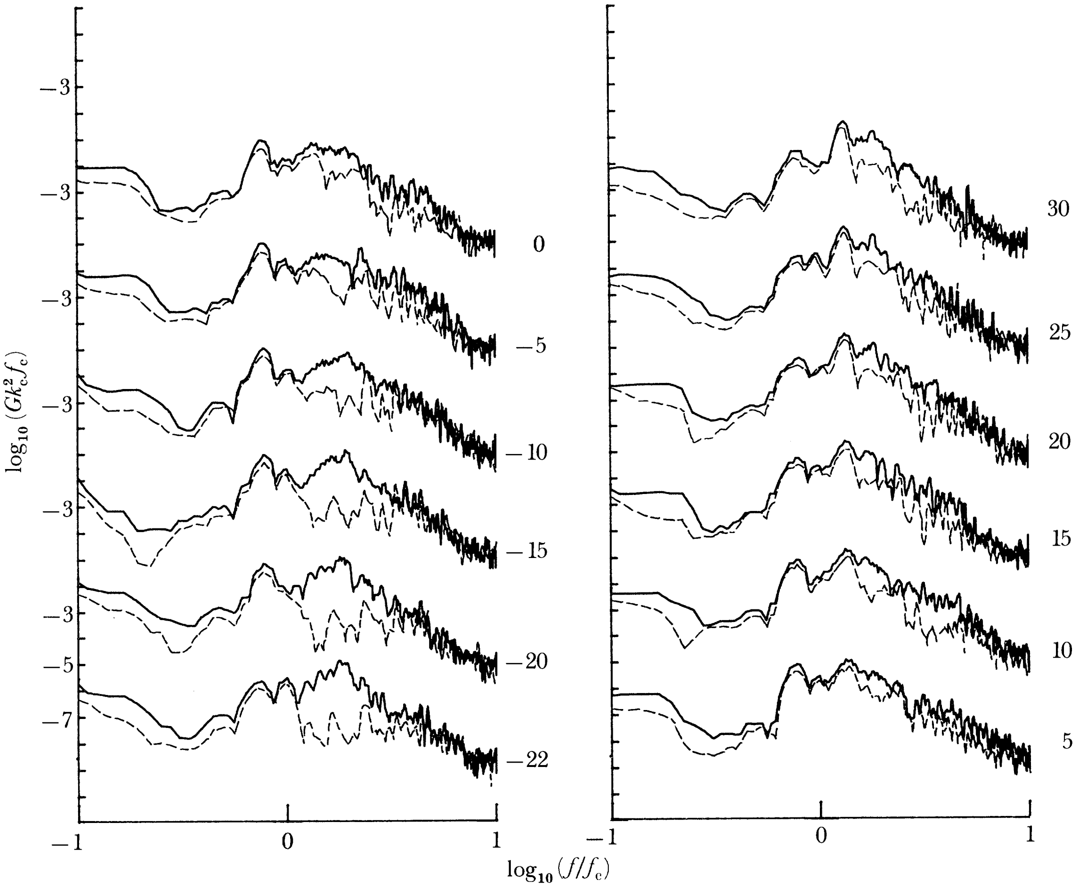

FIGURE 28. Spectra of waves radiated away from breaking disturbance $f_c = 0.88$ Hz, $ak_c = 0.352$, plunging ——, $ak_c = 0.257$, incipient breaking – – –. 95 % confidence interval for spectral estimates is equal to 1 unit on the left axis. The numbers on the graphs are values of $k_c(x - x_b)$.

tend to show that these may in fact be deterministic, surviving the ensemble averaging (figure 40). Downstream of breaking, the difference in the spectra between the incipient and plunging waves is not as large but still evident, suggesting that there are also second harmonic free waves generated by breaking that travel downstream. Comparison between the spectra of the radiated waves due to the large and small scale plunging waves shows that they scale with the waves in the incident packet.

4. FLOW VISUALIZATION OF MIXING IN THE BREAKING REGION

4.1. *Procedures and analysis*

Flow visualization experiments were done to quantify the rate and spatial extent of turbulent mixing of fluid initially at the free surface. By photographing the mixing of a dye patch floated on the water surface, a measure of the mixing, specifically, the time rate of lengthening, deepening, and increase in area of the mixed region, as a function of the wave parameters was obtained. The rate of mixing may then be related to the momentum flux lost from the wave field.

In these experiments we measure the maximum excursion (from breaking) of a continuous sheet of dyed particles with time. A surface dye patch was formed by placing small amounts (quarter of a teaspoon) of blue powdered vegetable dye (FD & C blue no. 1, H. Kohnstamm & Co., New York) on the water surface at equally spaced intervals along the channel centreline. Care was taken to apply the dye gently so as not to break the water surface. The water surface was first skimmed clean of any contaminants. This allowed the dye to spread evenly and the dye slicks to merge and form a uniform and continuous slick over a length of approximately twice the expected mixed region (i.e. about two centre wavelengths). The dye remained on the surface even under the action of near breaking waves. Mixing was observed only when the free surface was broken. Even a very gentle breaking, with no visible air entrainment was observed to trigger mixing. The initial thickness of the dye patch is important in determining the concentration of dye after it is mixed into the water column. However, we do not believe the initial dye thickness (which was very much less than the wave height) affects the maximum excursion of the dye and so is not important in these measurements.

The dye mixing was recorded with a 16 mm Bolex REX ciné camera at 48 frames per second for 12 s and at 24 frames per second for 25 s. A back-lit white cloth background provided good contrast between the mixed and unmixed region when filmed with colour reversal film. At the same time as the ciné films were made, 35 mm slides were also taken as examples. These photographs are shown in figure 29, plate 4, for a plunging breaking and figure 30, plate 4, shows a spilling breaker. These correspond to $f_c = 0.88$ Hz, the large scale. Time (in seconds) referenced from the top photograph, are shown in the bottom right corner. Tick marks are at 10 cm intervals. The two series of photographs are at different spatial scales.

The plunging breaking starts at $x = 6.9$ m (figure 29), which is just off the left margin (7.0 m is at the left edge of the frame). Dye is carried down by the initial jet and the turbulent front mixes dye ahead. Two regions of dye are evident. Photographs of bubbles in figure 10 also show the two regions. Notice the role of the next passing trough in pumping down the dye. The depth of the dye, as measured from the actual free surface, is roughly 10 cm (see figure 29, $t = 0$ s). In the next frame ($t = 0.7$ s), the free surface is carried down to $\eta = -10$ cm from the still water line resulting in a displacement of the dye bottom to -20 cm. As the next crest passes, the bottom of the dyed water does not move up but remains at a depth of -20 cm and rather is 'stretched' to a thickness of 25 cm. We believe this observation is due to the modulation of the wave height in the wave packet. Within two wave periods from breaking the dye has mixed to approximately one and a half wave heights. The dye continues to be mixed down by the turbulence generated by breaking.

The dye under the spilling breaker (figure 30) is mixed down by the turbulent region propagating at near the wave phase speed. Again the following wave assists in displacing the dye downward, after which the generated turbulence takes over in mixing down the dye. A quantitative analysis of the motion is given below.

In photographing this wave, the ciné camera axis was perpendicular to the length of the channel and recorded a transversely integrated measure of the dye concentration as a function of depth, length and time. Although the wave was very nearly two dimensional (i.e. little transverse variation), the turbulent mixing process is three dimensional. However, it was observed that the dye front varied little across the tank and the bottom boundary varied by about 20% of the mean depth of the dye region across the tank. As the length and depth reference marks were located on the front glass wall of the channel, camera parallax could potentially cause the location of the dye boundary to be underestimated if the boundary is not two dimensional across the tank.

Because the boundary was nearly two dimensional the error in the length measurement is less than 10%. In the depth measurement, the parallax angle was small, so even though the depth boundary was not two dimensional, the error is also less than 10%. In both cases the errors cause the quantities to be underestimated.

The cine films show a relatively sharp, well-defined boundary between the dyed and undyed region even though the dye density tends to decrease with depth. Ciné film records were made for single plunging and single spilling for the three scales of the input wave packets ($f_c = 0.88$, 1.08, 1.28 Hz). Two repeats were made for each wave packet. The wave packet bandwidth and breaking location were held constant at $\Delta f/f_c = 0.73$, $x_b k_c = 27.4$.

The films were analysed by projecting on a CALCOMP 9000 digitizing table and tracing the dye boundary for each frame. Digitizing the dye outline for each time step and storing the coordinates in a computer file permitted easy computation and display of the dye depth, length and area against time. Tick marks on the channel glass wall were used to calibrate the digitizer. A third-order polynomial was fitted to the digitizer output of readings of the tick marks in the film frame. This corrects for distortion due to the lens focal length mismatch between the camera and projector and any lens nonlinearity. A resulting accuracy of ± 1 cm^2, which is within the parallax errors, was realized.

Examples of the digitized evolution of the dye boundary in time are shown in figure 31 for a spilling wave and in figure 32 for a plunging wave. Note that these correspond to the medium scale of $f_c = 1.08$ Hz. The top trace is of the free surface just after breaking. The centre wave period is 0.93 s in these examples, so appreciable mixing has taken place within one wave period. The trough of the following wave can be seen pushing the dye down further as described previously. The tracing of figure 32 can be qualitatively compared with the photographs of the bubble cloud in figure 10 where two clouds are formed by the plunging. Note that they represent different scales of the wave packet, however.

The digitized data was analysed for the dye length at the surface, L, the maximum depth, D, and the area (see figure 31). These quantities are non-dimensionalized using k_c^{-1} as a length scale and plotted against non-dimensional time $\omega_c t$ in the results that follow.

4.2. *Spatial evolution of mixing*

The results plotted in figure 33 show the maximum dye cloud length against time for a single spilling wave and a single plunging wave. The results of the three scales of wave packets are overplotted with the indicated symbols. The timescale is referenced from t_c, which is the observed time (from ciné films) of the wave crest crossing the theoretical breaking location or focal point. This reference was used to compare the observed time of breaking between scales. The original intention was to reference the time from t_b (equation (2.3)) by starting a clock at paddle startup. However, the clock face was difficult to resolve in the films so the former method of time referencing was used.

These plots show a rapid increase in the dye length, that is linear in time, at a rate of 0.7–0.8C, where C is the linear wave phase speed computed for finite depth from f_c. The dye length increases to $k_c L \approx 4$ ($k_c L = 2\pi$ is one wavelength) in two wave periods. During this time, the rear boundary of the dye is essentially stationary (see figures 29 and 30), while the turbulent front is moving downstream at the free surface. The oscillations in L are due to the next passing wave trough (minimum of $k_c L$) and the next crest whose orbital velocity displaces the dye front forward to $kL \approx 5$. Essentially, then, the trailing waves act to pump the dye ahead an additional amount. Good agreement can be seen between scales and between repeats of the

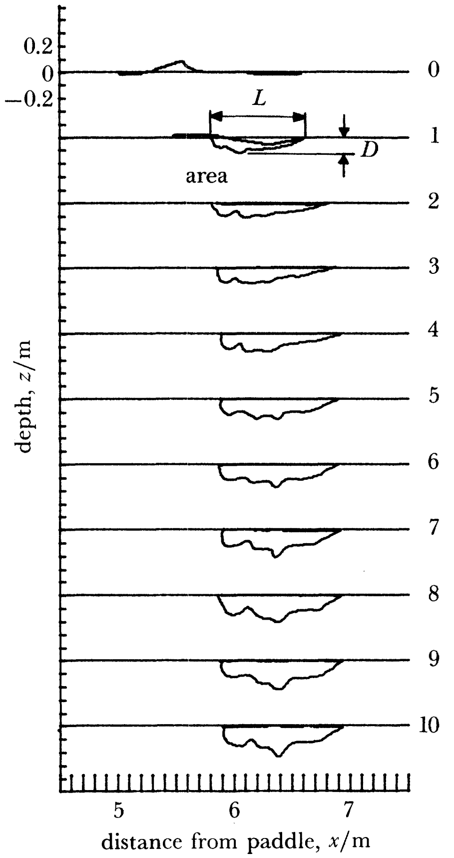

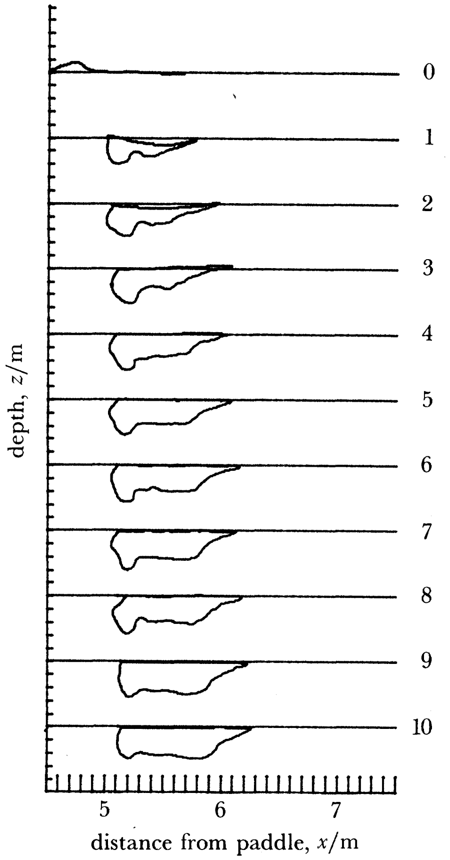

FIGURE 31 (left). Digitized data of dye boundary taken from ciné films. Wave packet with $f_c = 1.08$ Hz, $k_c = 4.721\ \mathrm{m}^{-1}$, $ak_c = 0.296$ (spilling). $\Delta f/f_c = 0.73$, $x_b k_c = 27.4$. Time steps are referenced from t_{ob}, time of observed breaking in seconds. Top contour is the free surface at breaking. Refer to table 1 for definition of t_{ob}. Numbers on right-hand side refer to $t - t_{ob}$.

FIGURE 32 (right). Digitized data of dye boundary taken from ciné films. As for figure 31 except $ak_c = 0.388$ (plunging).

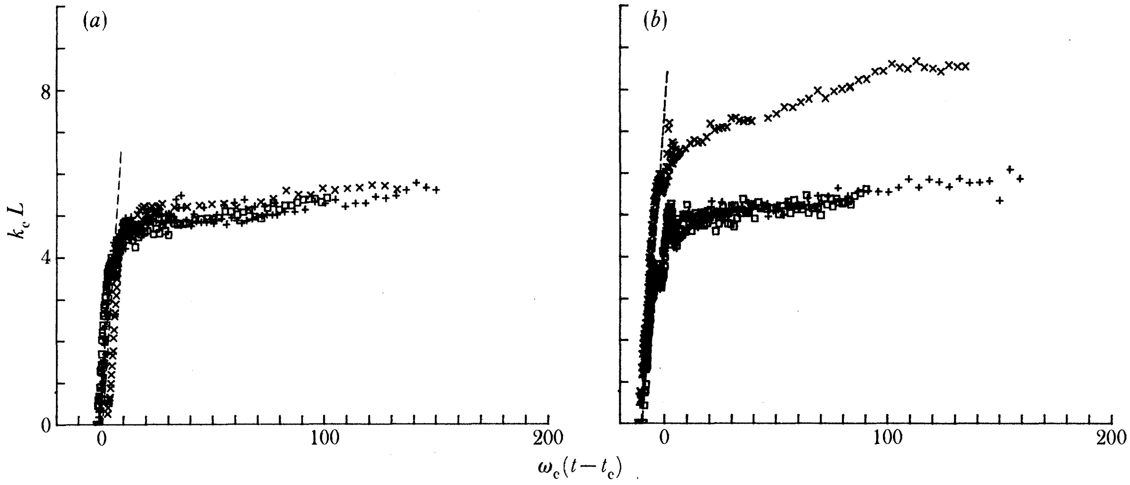

FIGURE 33. Length of dye boundary against time from t_c for (a) spilling wave and (b) plunging wave. Wave group centre frequency $f_c = 0.88$ Hz (×), 1.08 (+), 1.28 (□) and $\Delta f/f_c = 0.73$; $x_b k_c = 27.4$. ---, $0.8C$, phase speed.

same scale packet. Also, the length of the dye is the same for spilling and plunging, except for the case of the large-scale plunging wave $f_c = 0.88$ Hz.

This discrepancy appears to result from the increased air entrainment in the large scale. The sequence of photographs (figure 9*a*, *b*) show a secondary jet causing mixing farther downstream, which was not as pronounced in the smaller scales. The Froude scaling used in these results apparently does not scale this phenomenon.

After three wave periods and after the waves have passed, the rate of lengthening is much slower at *ca.* 0.005–0.01C, which indicates a slow drift current at the surface.

The maximum depth of dye excursion, D, against time is plotted in figure 34. In the spilling wave, the free surface is initially broken near the crest, which is above the still water line. This observation is manifested in these plots, as the maximum depth is initially above the still water line for the spilling wave. The initial rate of deepening is of the order of the wave orbital velocity, 0.18C and again emphasizes the role of the following wave trough in carrying the dye down. Based on observations of ciné films, the following description is offered. The mixing due to breaking carries the dye down to $k_c D \approx 0.3$ for spilling and $k_c D \approx 0.5$ for plunging, both within $\frac{1}{2}$ wave period from breaking. The next passing wave carries the dye down an additional $k_c D \approx 0.3$, to $k_c D \approx 0.6$ for spilling and $k_c D \approx 0.8$ for plunging. Again, because the next crest is of lower amplitude the maximum dye depth does not completely recover to its original level, but small oscillations in the maximum depth are observed as the few remaining waves in the packet pass by.

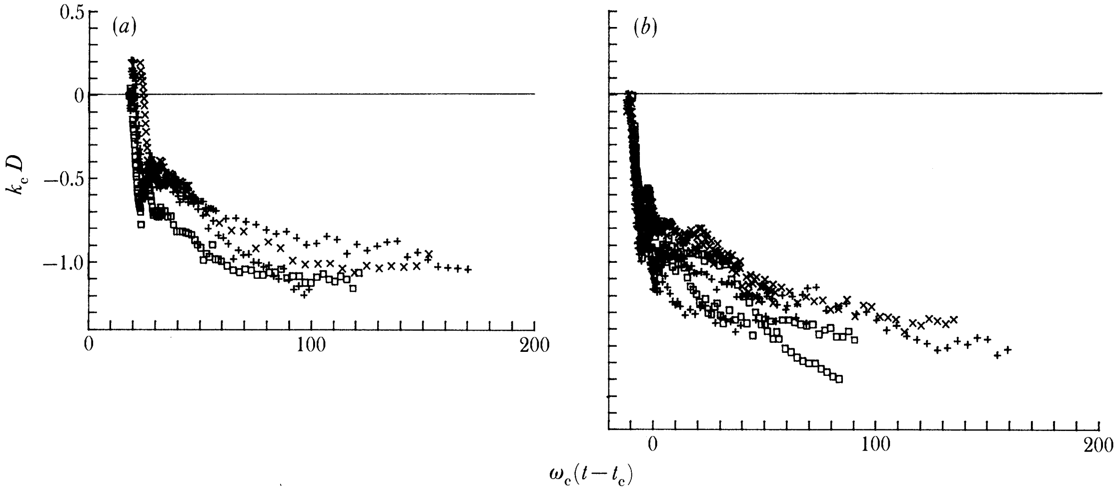

FIGURE 34. Maximum depth of dye boundary below still water level against time for (*a*) spilling wave and (*b*) plunging wave. Wave group centre frequency $f_c = 0.88$ Hz (×), 1.08 (+), 1.28 (□) and $\Delta f/f_c = 0.73$, $x_b k_c = 27.4$.

After approximately three wave periods, the waves have passed and further deepening is due to turbulent diffusion in the highly turbulent flow generated after breaking. In anticipation of self-similarity in the evolution of the dye cloud, an attempt is made to fit this data to a power law in time of the form

$$k_c D = \gamma_1[\omega_c(t-t^*)]^p. \tag{4.1}$$

To empirically determine p the data is plotted on a log–log scale. The equation becomes

$$\log_{10}(k_c D) = \log_{10}\gamma_1 + p\log_{10}[\omega_c(t-t^*)], \tag{4.2}$$

where p is the slope of a straight line that fits the data and $\log_{10}\gamma_1$ is the y intercept. Because the data may not be expected to follow this equation in the immediate vicinity of the time origin, a virtual time origin is usually determined by iteration. As p is dependent upon t^*, the proper choice of t^* is important. The value of t^*, time origin, which gives the longest straight-line fit to the data is the usual choice for t^* (Compte-Bellot & Corsin 1966). The value of t^* that gave this result turned out to be very close to the observed time of breaking, t_{ob}, as defined in §3.1. To eliminate any ambiguity over the choice of time origin, the time of observed breaking was used as the origin. Note that only the data at times after one wave period from breaking were considered in this curve fitting, as the dye motion is dominated by the wave orbital velocity before this time.

The log–log plot corresponding to the maximum depth (figure 35) shows that a slope of $p = \frac{1}{4}$ fits the data reasonably well. The range of the coefficient, γ_1, is determined graphically by drawing two $p = \frac{1}{4}$ slope lines enclosing the spread of data. The y intercepts of these lines give the following range of γ_1:

$$\gamma_1 = \begin{cases} (0.28\text{–}0.43) \text{ for spilling,} & (4.3\,a) \\ (0.38\text{–}0.57) \text{ for plunging.} & (4.3\,b) \end{cases}$$

The value of p is very well followed for the three scales in these experiments. The spread of γ_1 is due to scale effects and due to the random error between runs.

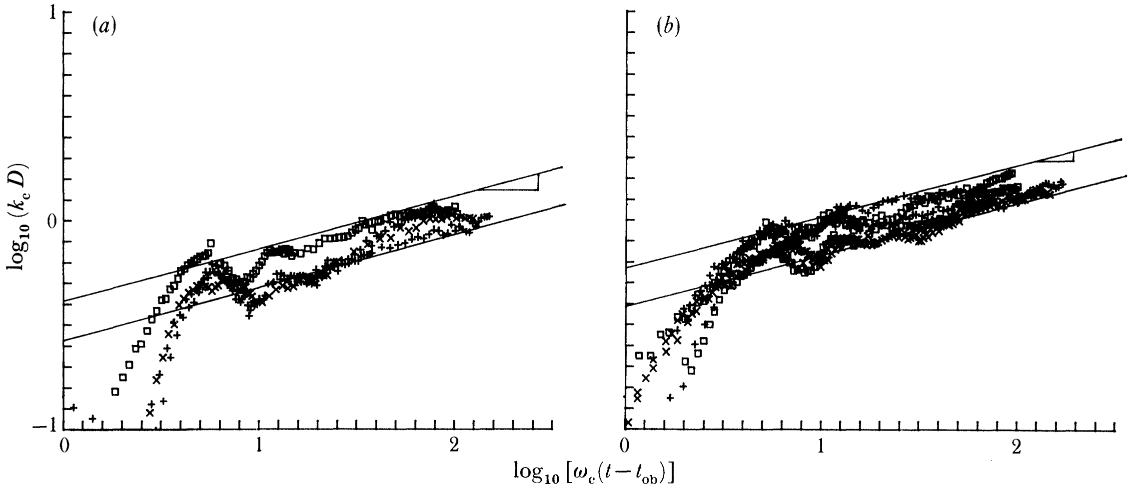

FIGURE 35. Log–log plot of maximum depth against time from observed breaking. Same symbols as figure 34. Plot shows fit of data to $\omega_c(t-t_{\mathrm{ob}})^{\frac{1}{4}}$ power law.

The two dimensional mixed area is similarly plotted for the spilling and plunging wave. The log–log plot of this data (figure 36) shows that after one wave period from t_{ob}, the non-dimensional area grows as $\omega_c(t-t_{\mathrm{ob}})^{\frac{1}{2}}$ for both levels of breaking. As for the maximum depth, the time origin is the time of observed breaking, t_{ob}. Given that the area is normalized by k_c^2, the agreement between scales is quite good and within the scatter of repeated runs of the same wave. Note that the large scale ($f_c = 0.88$ Hz) plunging wave case grows fastest, which is consistent with the fast growing length measurement due to the additional spray generated. The coefficients for the power law were graphically estimated as

$$\gamma_2 = \begin{cases} (0.32\text{–}0.45) \text{ for spilling,} & (4.4\,a) \\ (0.48\text{–}0.74) \text{ for plunging,} & (4.4\,b) \end{cases}$$

and the area is given by

$$k_c^2 \,\text{area} = \gamma_2[\omega_c(t-t_{\mathrm{ob}})]^{\frac{1}{2}}. \qquad (4.5)$$

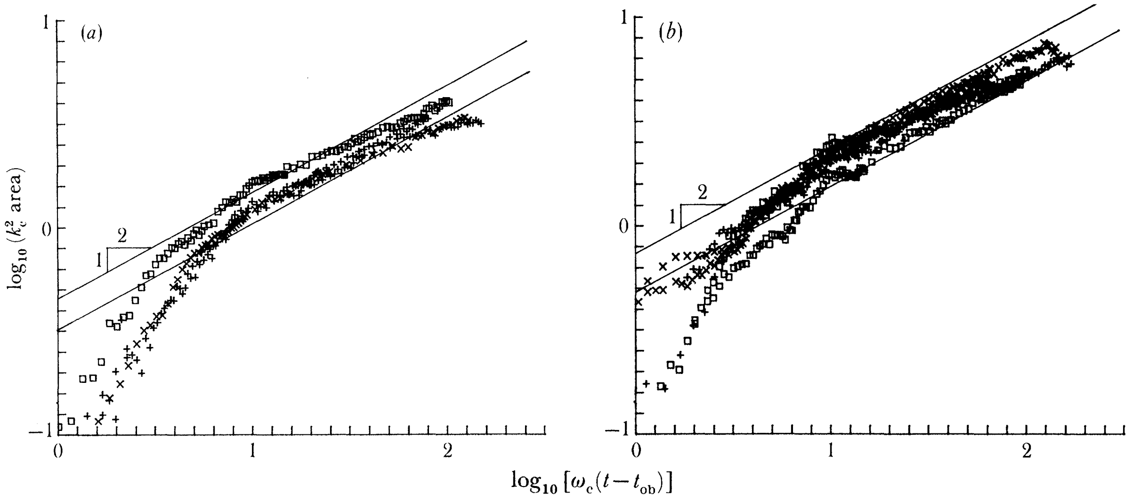

FIGURE 36. Log–log plot of dyed area against time from observed breaking. Same symbols as figure 34. Plot shows fit of data to $[\omega_c(t-t_{ob})]^{\frac{1}{2}}$ power law.

4.3. *Mixed region dependence on wave packet amplitude*

The non-dimensional amplitude, ak_c, was found to be the most sensitive wave packet parameter affecting the loss of momentum flux from the wave field. It also has been found to be important in determining the rate of mixing, through the coefficients γ_1, γ_2 in the power laws for mixed depth and area. These coefficients are plotted against ak_c in figures 37 and 38. The shapes of these estimated curves look similar to the plots of momentum flux loss against ak_c (figure 15) where there is a steep rise in the depth and area of mixing. Once incipient breaking is triggered at $ak_c \approx 0.25$, the curve then starts to level off in the plunging region. The vertical error bars are indicative of the scatter in the measurements between repeats of the same wave. This is also the error between scales of packets. The horizontal 'error' bars indicate the range of ak_c over which a single spilling or plunging wave was generated for the three scales of wave packets. (Note that for each scale, the value of ak_c producing an incipient spilling or plunging breaking wave does not change from run to run.)

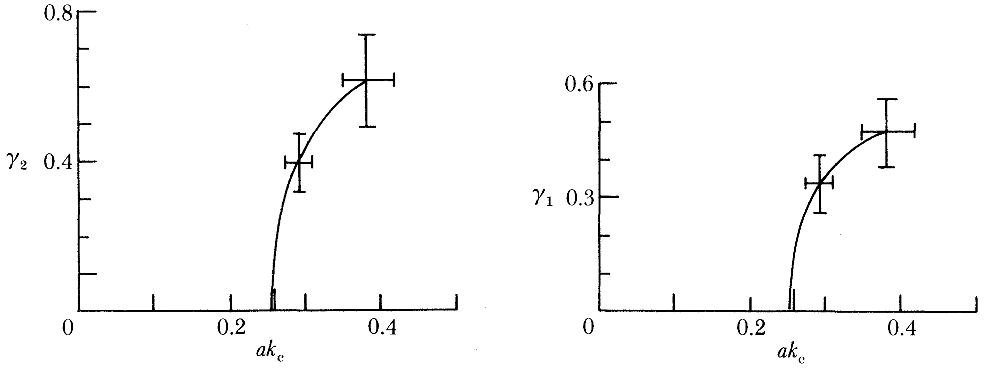

FIGURE 37 (left). Dyed area coefficient, γ_2, as a function of wave packet amplitude, ak_c. Dyed area is given by k_c^2 area $= \gamma_2[\omega_c(t-t_{ob})]^{\frac{1}{2}}$.

FIGURE 38 (right). Dyed depth coefficient, γ_1, as a function of wave packet amplitude, ak_c. Dyed depth is given by $k_c D = \gamma_1[\omega_c(t-t_{ob})]^{\frac{1}{4}}$.

The measurements made here were on one breaking wave in the packet. At intermediate values of ak_c more than one breaking wave is generated, so it is not clear how the total area or maximum depth will be affected if all breaking regions are summed.

4.4. *The integral length scale of turbulence*

A continuous range of length scales is present in turbulent flows, the largest being the size of the flow field. The integral length scale of the turbulence, l, is very useful in describing the turbulence through such parameters as the eddy diffusivity $K \approx ul$ and Reynolds number. Here u is a characteristic velocity, usually the r.m.s. velocity. Also dissipation can be estimated by $\epsilon \approx u^3/l$ (Taylor 1935). The integral length scale is defined as the area under the velocity autocorrelation function, divided by the autocorrelation at zero separation (Hinze 1959, p. 37):

$$l = \int_0^\infty \frac{\overline{u(\xi)\, u(\xi+x)}\,\mathrm{d}x}{\overline{u^2}}.$$

This length scale is roughly a measure of the width of the turbulence if the flow is not periodic (Hinze 1959). In our measurements, D, the maximum dye depth, will be considered to be roughly comparable with l. We found $l \approx t^{\frac{1}{4}}$. Also the dye area was proportional to $t^{\frac{1}{2}}$, so $(\text{area})^{\frac{1}{2}} \approx t^{\frac{1}{4}}$, which is consistent with our results. We would also expect the horizontal length to vary as $t^{\frac{1}{4}}$, but at the surface where the length was a maximum it was found to be nearly constant. However, from observations of dye mixing films, and as can be seen in figures 29 and 30, the growth rate of dye length at the surface may not be the relevant parameter. The growth rate appears to be faster if one considered the horizontal length as some depth below the free surface. Here the eddies are more active in mixing the dye front forward. The growth rate is not zero but should be close to $t^{\frac{1}{4}}$. Measurements were not made at this depth, however. With measurements of turbulent velocities (§5), the time variation of l will be used to estimate the time dependence of K and ϵ.

5. VELOCITY MEASUREMENTS IN THE BREAKING REGION

5.1. *Procedures and analysis*

Having measured the loss of momentum flux and energy flux from the carrier wave field (§3), an attempt is made to account for this loss by measuring the velocity of the flow field in the breaking region. The dye measurements serve as a guide in defining the region over which a detailed velocity survey was done. It is expected that the net horizontal momentum loss from the carrier waves will result in a surface current and that the loss of energy will go into both average and turbulent velocity fields and be dissipated. Because the net horizontal momentum density of the carrier waves plus the forced wave integrated over depth is nearly zero upstream and downstream of breaking, the net momentum integrated over depth in the breaking region must also be zero. It is important, however, to determine how the momentum or current is distributed in depth. The mixing down of turbulent kinetic energy and its decay in time are also obtained from the velocity measurements.

Crucial to any analysis of this type, be it with field or laboratory data, is our ability to distinguish various velocity contributions. We expect the motion to be the sum of the carrier wave orbital velocity, the nonlinearly generated forced wave, the current generated by breaking, and the turbulent velocities. Ensemble averaging over many runs of the experiment was found to be the only method of determining the mean and turbulent quantities in this non-stationary flow generated by breaking. This averaging also effectively separates the deterministic wave orbital velocities (carrier wave and forced waves) from the non-repeatable turbulence. The velocity of the random waves, generated by breaking, is shown to be small in comparison with the random turbulent velocities, particularly away from the free surface where the wave motion decays to low levels. The ensemble averaged signals of the mean velocity are low-pass filtered to remove the carrier waves, resulting in a signal of the forced long wave and the currents generated at breaking. As the currents are long-lived and the forced wave passes the probe relatively quickly, these two contributions are separable in time. The ensembled averaged variance of the turbulence is also filtered to remove the high frequency random errors in the averaging.

The two component velocity measurements were made using the laser Doppler anemometer described in §2. Data was typically sampled at 50 Hz for 81.96 s. A coincident surface displacement measurement was also made. The wave gauge was slightly displaced downstream by 1 mm, and transversely by 10 mm so as not to interfere with the laser beam paths. Data was processed between repeats of the experiment. The time between breaking events was approximately ten minutes, which was found to give sufficient time for the mean motions to decay to negligible levels.

A typical 81.96 s time history of the measured surface displacement η and subsurface eulerian velocity u, and w is shown in figure 39. These are the unfiltered raw signals. Note the clean velocity signal, particularly in the non-turbulent flow before breaking and how well η and u follow one another. The velocity resolution here is better than 0.5 cm s^{-1}, within the thickness of the plot line. The drop-out in the velocity signal is due to the wave trough passing

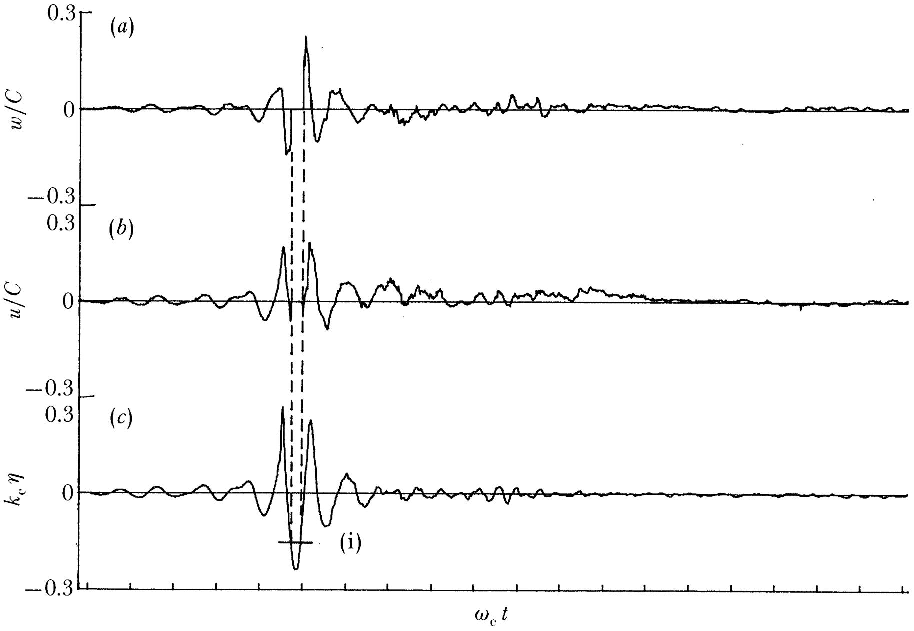

FIGURE 39. Coincident surface displacement and subsurface velocity measurement at $k_c(x-x_{ob}) = 3.80$ and $k_c z = -0.16$ downstream of plunging break. For $f_c = 0.88$ Hz, $ak_c = 0.352$, $\Delta f/f_c = 0.73$, $x_b k_c = 27.4$. C is the linear phase speed, k_c is the wavenumber corresponding to f_c for finite depth. (a) Vertical velocity, (b) horizontal velocity, (c) surface displacement, (i) elevation of velocity probe volume.

the measurement point; the signal is quickly recovered as the next crest crosses the beam intersection point. At times after breaking, the signal is seen to become quite turbulent at all frequencies, almost obscuring the underlying wave velocities. There is also evidence of a mean horizontal and vertical velocity at times after breaking. The measurements of ten repeats of the same breaking wave made at the same measurement point show the variability of the low-frequency motion downstream of breaking. From this set of data it is obvious that one measurement is a poor indicator of the mean motion.

The data is analysed by forming ensemble averages of measurements from many repeats of the experiment with 'identical' initial and boundary conditions. The averages are taken over data at constant times from paddle startup and no attempt is made to adjust the starting phase for best agreement. The ensemble mean is defined as

$$\langle u(x,z,y,t)\rangle = \frac{1}{Q}\sum_{q=1}^{Q} u_q(x,z,y,t), \tag{5.1}$$

where Q is the number of repeats. The same is done for the vertical velocity w and surface displacement η. The raw velocity is then

$$u = \langle u\rangle + u', \tag{5.2}$$

where u' is the fluctuation from the ensemble mean. The variance of the signal is computed as

$$\langle [u'(x,z,y,t)]^2\rangle = \frac{1}{Q}\sum_{q=1}^{Q} [u'(x,z,y,t)]^2. \tag{5.3}$$

In the plots that follow it is convenient to show the square root of this quantity which will be defined as

$$u_{\text{r.m.s.}} = \langle [u'(x,z,y,t)]^2\rangle^{\frac{1}{2}}. \tag{5.4}$$

Examples of the ensemble averaged wave surface elevation and r.m.s. fluctuating velocities are shown in figures 40 and 41, where the number of realizations averaged is 10 and 40 respectively.

The ensemble mean velocities are composed of contributions due to the carrier waves u_{cw}, a forced long wave, u_{fw}, and a current, u_{c}, which are all functions of time. Then

$$\langle u\rangle = u_{\text{cw}} + u_{\text{fw}} + u_{\text{c}}. \tag{5.5}$$

The residual signal is considered to be composed of random waves u'_{w}, turbulence u'_{t} and instrument noise u'_{n}.

Then

$$u' = u'_{\text{w}} + u'_{\text{t}} + u'_{\text{n}}. \tag{5.6}$$

The square of u' will give cross terms of $u'_{\text{w}}u'_{\text{t}}$, $u'_{\text{w}}u'_{\text{n}}$, and $u'_{\text{t}}u'_{\text{n}}$, which, when averaged over the ensemble, are assumed to be negligible, because any correlation between these motions is weak. Then

$$\langle u'^2\rangle \approx \langle u'^2_{\text{w}}\rangle + \langle u'^2_{\text{t}}\rangle + \langle u'^2_{\text{n}}\rangle. \tag{5.7}$$

The magnitude of the measurement noise $\langle u'^2_{\text{n}}\rangle$, can be seen in figure 41 at times before breaking where

$$u_{\text{r.m.s.}} = \langle u'^2_{\text{n}}\rangle^{\frac{1}{2}}. \tag{5.8}$$

This shows $u_{\text{r.m.s.}}$ due to noise $= 0.34\ \text{cm s}^{-1}$ and $w_{\text{r.m.s.}} = 0.2\ \text{cm s}^{-1}$. The noisier u component of velocity is a result of the lower intensity blue laser beam used for the u measurement. This

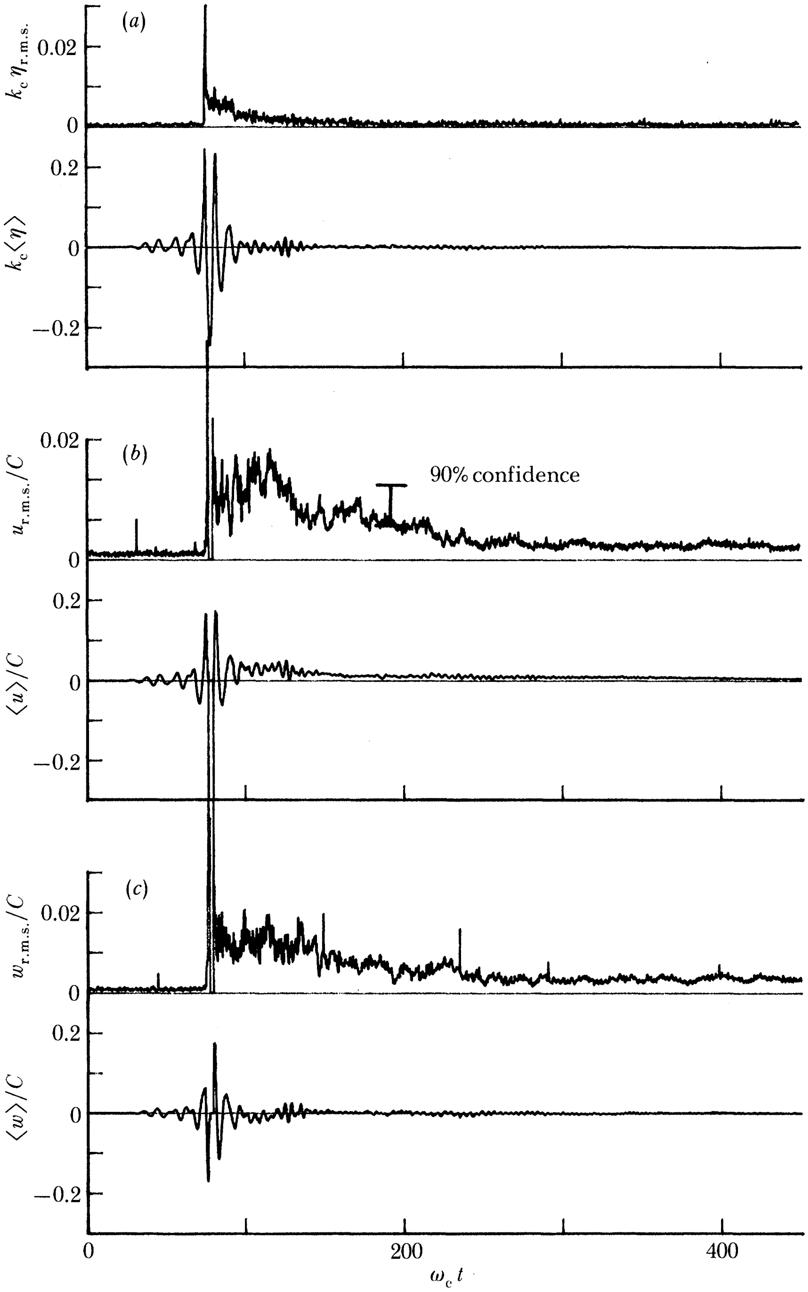

FIGURE 40. Ensemble averaged velocities $\langle u \rangle$, $\langle w \rangle$ and surface displacement $\langle \eta \rangle$. Also the corresponding r.m.s. velocities, and surface displacement. Average of 10 repeats; same location as figure 39. (*a*) Surface displacement, (*b*) horizontal velocity, (*c*) vertical velocity.

noise level is relatively small when compared with the r.m.s. velocity after breaking. The noise in the wave gauge measurement is also small compared with the measured r.m.s. values of surface displacement.

The large spikes in the variance at breaking are largely due to the non-repeatability of the wave-phase, measurement noise due to bubbles, and signal dropout in the wave trough. It is unlikely that drop-out will occur at exactly the same time for each run, and this variability

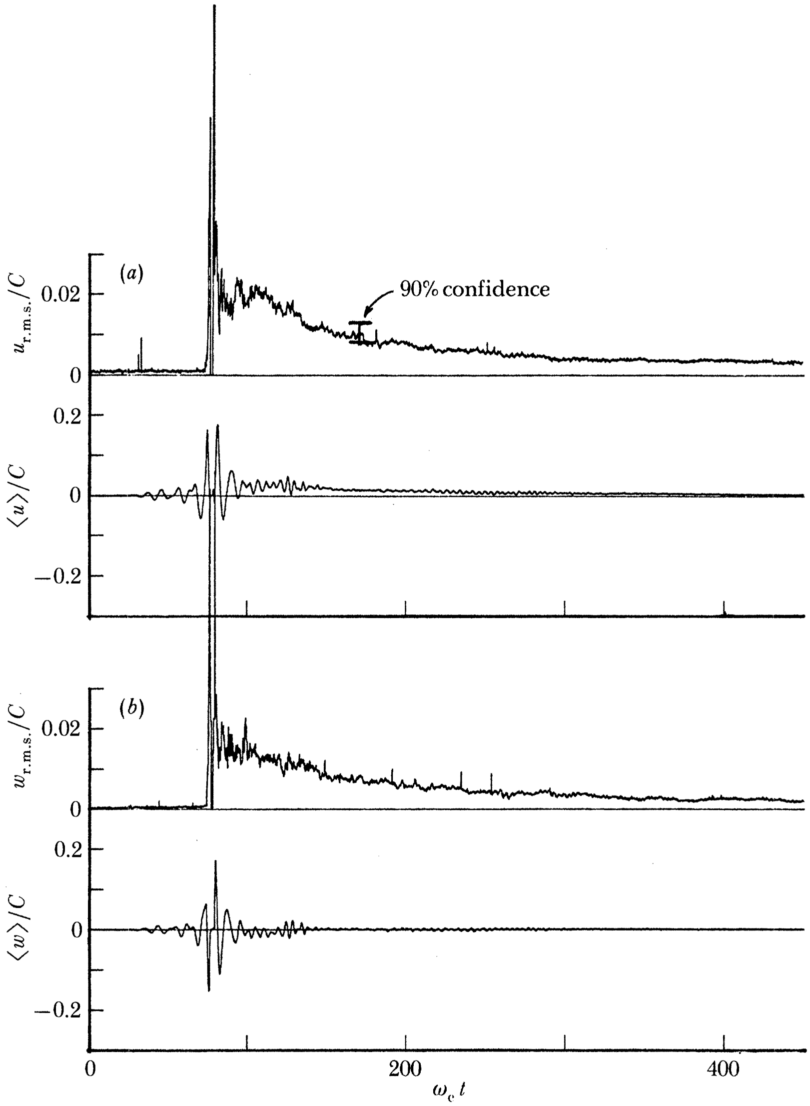

FIGURE 41. Ensemble averages as in figure 40 for 40 repeats. (*a*) Horizontal velocity, (*b*) vertical velocity.

results in spikes in the variance. After the wave packet has passed the velocity probe, the variance level is still quite high at $u_{\text{r.m.s.}} \approx 0.02C$. The question still remains as to how much of this is turbulence and what do the random-wave orbital velocities contribute.

Now the maximum contribution from random waves can be seen in the curve of $\eta_{\text{r.m.s.}}$ (figure 40). If the random waves are of frequency ω_c, then $k_c \eta_{\text{r.m.s.}}$ represents the velocity, $u_{\text{r.m.s.}}/C$ due to waves at the free surface as given by linear theory. This contribution will decay with depth. If the random waves are of frequency $2\omega_c$ then the contribution will be twice that shown in the figure; however, it will decay even faster with depth. With this in mind, the contribution of random waves to the variance is 10%.

At times after the wave packet has passed we will interpret the variance of the fluctuating velocity as being due solely to turbulence, with an error of approximately 10%. Then

$$\langle u_t'^2\rangle \approx \langle u'^2\rangle \tag{5.9}$$

The ensemble means in these figures show a slowly varying horizontal current of $0.03C$, generated by breaking, with the superimposed velocity of a small packet of trailing waves separated from the main group. At later times $\omega_c t = (200\text{–}300)$ a very-low-amplitude, high-frequency wave train is passing. The phase of u follows the phase of η, indicating that they are travelling downstream. These waves have sustained an averaging of over 40 repeats (figure 41)! They are believed to be second harmonic waves radiated upstream from the breaking region, then reflected back from the wave paddle (see §3.5).

The vertical mean velocity shows a negative flow just after the packet has passed, and essentially zero velocity at later times. No mean set down in the free surface can be seen in this figure, after the packet has passed. This indicates that the mass flux in the horizontal current is being supplied from below or from upstream, because, by conservation of mass,

$$\rho\, \partial\bar{\eta}/\partial t + \partial M/\partial x = 0 \tag{5.10}$$

and $\partial\bar{\eta}/\partial t = 0$.

The extent to which the averages of ten realizations converge to the true mean can be seen by comparing it with the averages taken over 40 repeats (figure 41). The differences between the mean, computed with $Q = 10$ and $Q = 40$, are negligible. The effect on the r.m.s. average is to reduce the random error and oscillations evident in figure 40. At times after the waves have passed, this comparison shows that the oscillations in the r.m.s. average over ten repeats are in fact random errors and may be smoothed with time averaging, which will closely approximate the more time consuming 40 repeat averaging. At the rear of the packet, however, there appears to be a correlation between the turbulence, $u_{\text{r.m.s.}}$, and the carrier wave, $\langle u \rangle$, with $u_{\text{r.m.s.}}$ approximately 180° out of phase with $\langle u \rangle$. An explanation of this may be that a region of higher turbulence near the surface is advected down to the fixed measurement point by the wave orbital velocity. This explains why the turbulence is greater when the wave trough passes the measurement point.

The data was further processed by filtering the repeatable, carrier-wave velocity from the ensemble mean velocities. This was done by low-pass filtering the ensemble mean with a filter having a cut-off frequency $f_{\text{cut}}/f_c = 0.34$ or $f_{\text{cut}} = 0.3$ Hz for $f_c = 0.88$ and $f_{\text{cut}} = 0.436$ for $f_{\text{cut}} = 1.28$ Hz. The filter was designed by specifying an ideal boxcar frequency response and then using a Hamming weighting on the impulse response to improve the stop band attenuation. The Fourier transform was then taken, resulting in the impulse response of the filter. The filter was implemented using the overlap-add method (Oppenheim & Shaffer 1975), which effectively does the linear convolution. An example of the filtered data can be seen in figure 42.

The ensemble averaged r.m.s. velocity was filtered in the same manner. Note that the filtering was done on the squared velocity, then the square root was taken (examples of this data are shown below in figure 45). This is consistent with taking short time averages on u'^2 if the process is stationary over short time segments.

5.2. *Mean velocities induced by breaking*

The low-pass filtered ensemble mean horizontal $\langle\bar{u}\rangle$ and vertical velocity $\langle\bar{w}\rangle$ were obtained at seven elevations and seven x locations from the observed breaking location. The three wave packets measured in this way were the large-scale ($f_c = 0.88$ Hz), plunging ($ak_c = 0.352$) and spilling ($ak_c = 0.278$) and the small-scale ($f_c = 1.28$ Hz) plunging ($ak_c = 0.420$) wave packets.

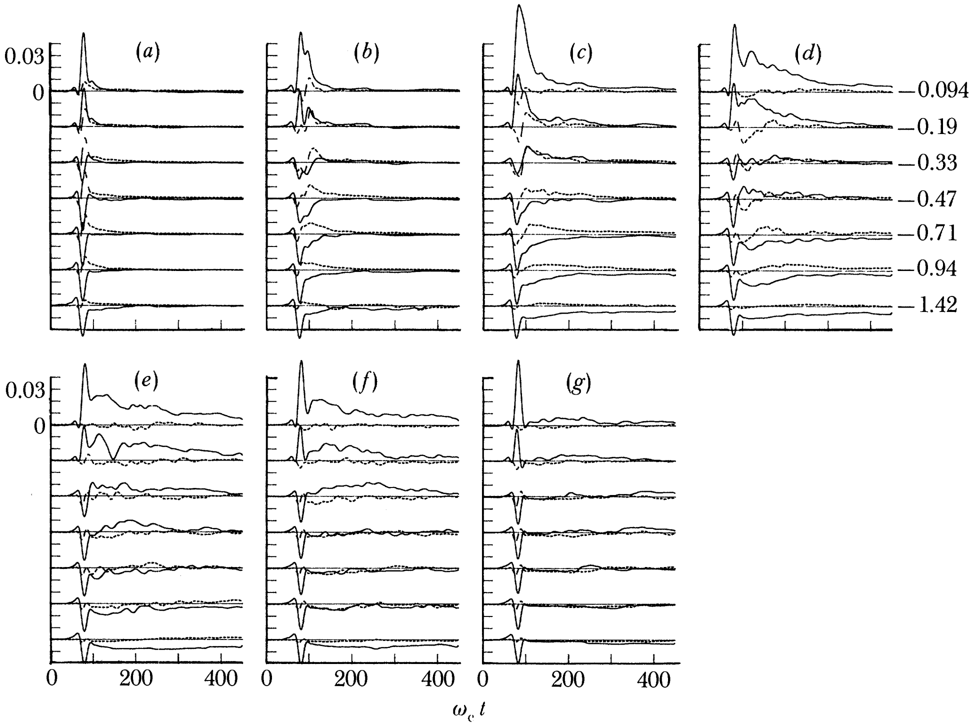

FIGURE 42. Time series of mean horizontal $\langle\bar{u}\rangle/C$, —— and vertical $\langle\bar{w}\rangle/C$, – – – velocity measured at stations downstream of breaking. Each curve is an ensemble average of 10 repeats which was then low pass filtered. $f_c = 0.88$ Hz, $ak_c = 0.352$ (plunging). With $k_c(x-x_{ob})$ values of (*a*) 0.94, (*b*) 1.9, (*c*) 3.0, (*d*) 3.8, (*e*) 4.7, (*f*) 5.7, (*g*) 6.6. The numbers on the graph are values of $k_c z$.

The measurement at each grid point represents ten repeats of the packet; a total of 490 runs were made for each of the three cases.

Figure 42 shows the case of the large-scale plunging. The first box shows measurements just downstream of observed breaking $(x-x_{ob}) = 0.29$ m. The positive mean horizontal velocity at elevations above the trough represent the mass flux in the carrier waves. This is consistent with the eulerian description, which gives all the carrier wave mass flux and momentum density in the trough to crest region of the waves. At depths below the wave trough the forced long wave velocity is evident, and can be seen to remain nearly constant with depth. The vertical mean velocity decays to zero near the bottom. The magnitude of this velocity, $-0.025C$, compares with the estimate from equation (A 14) based on weakly nonlinear wave theory of $\bar{u} = -0.026C$. The long transient wave ahead of the packet can be seen as the positive mean velocity at times before the packet has arrived at the probe. At later times, after the packet has passed, there remains a positive horizontal streaming which, at this x location, is advected downstream. This flow is supplied from below as seen by the upward vertical mean velocity at lower depths. Below an elevation of one wave amplitude $k_c z = 0.33$, there is a return flow set up after the packet has passed. At stations farther downstream these features are all magnified and are longer lived. At $k_c(x-x_{ob}) = 3.8$ the surface current induced by breaking is initially $0.03C$ decaying to $0.01C$ only after 60 carrier wave periods. The deeper return flow is also accentuated. The depth of penetration of the positive going flow has reached almost $1\frac{1}{2}$ wave amplitudes at this station. Finally, at stations approximately one wavelength from breaking, the current has decayed to less than $0.005C$ but is still significant.

The spatial flow field corresponding to these measurements is illustrated with the vector diagrams in figure 43. The time steps are referenced from the observed time of breaking. The top diagram illustrates the measured flow field as the wave group passes through the region. Note the mass flux due to the carrier waves near the surface and the return flow in the long forced waves. The bottom of the channel is at $k_c z = -1.95$ at this scale. After four wave periods from breaking, the group has passed the region and a large eddy is left behind. At the ends of the breaking region the horizontal velocity is near zero. The surface flow velocity is *ca.* $0.02C$ and the deeper return velocity *ca.* $0.01C$. The rotational motion is still significant after 50 wave periods from breaking.

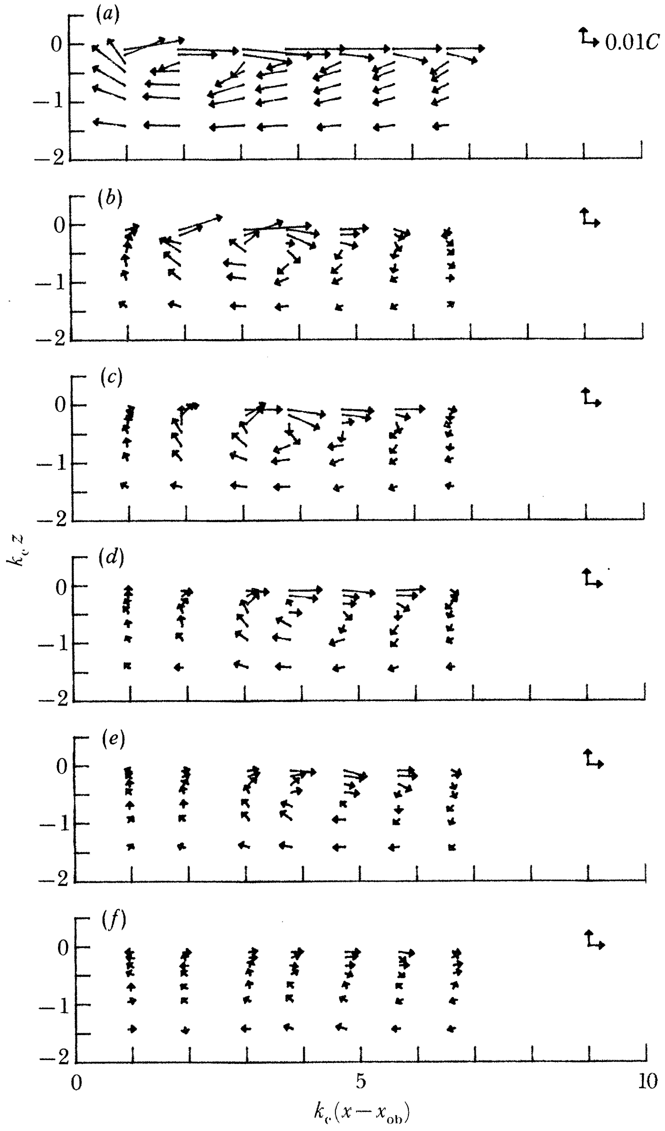

FIGURE 43. The mean velocity field at times after breaking for $f_c = 0.88$ Hz, $ak_c = 0.352$ (plunging), $\Delta f / f_c = 0.73$, $x_b k_c = 27.4$. Derived from ensemble averaged, low pass filtered measurements. Each vector is the average of 10 repeats. Channel bottom is at $k_c z = -1.95$ for this scale. Here $\omega_c(t - t_{ob})$ is (*a*) 2π, (*b*) 8π, (*c*) 12π, (*d*) 20π, (*e*) 40π, (*f*) 100π.

Similar results are shown for the large-scale spilling wave in figures 44 and 45. The filtered time history show the forced long wave under the packet to be $\bar{u} = 0.015C$ and is due to the lower envelope amplitude compared with the plunging case. The surface currents generated by this spilling breaking are still appreciable, initially at $0.02C$ and decaying slowly. The positive currents penetrate to depths comparable with the plunging wave. The return flow after the packet has passed, is smaller but a similar eddy is generated. It appears that the forced wave under the packet is important in setting up this large vortex. One may have attributed it to the overturning in the plunging wave; however, the size of the measured eddy is larger than the plunging region. Also the fact that it is set up in a spilling wave supports the idea that the group is important in generating it and not the plunging of the wave itself.

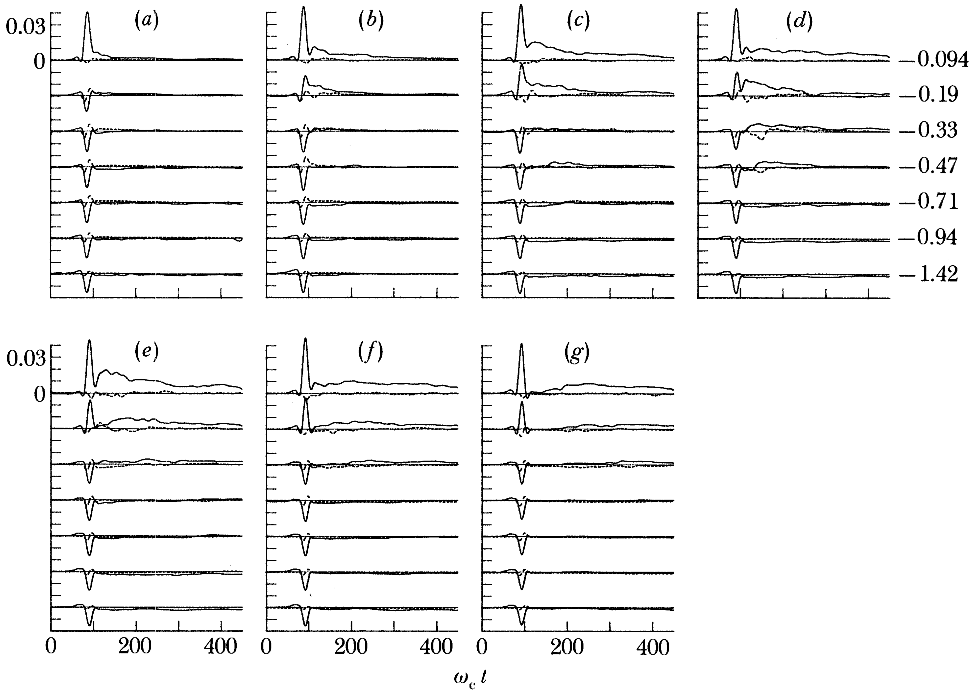

FIGURE 44. Time series of mean horizontal $\langle\bar{u}\rangle/C$, —— and vertical $\langle\bar{w}\rangle/C$, ---- velocity for $f_c = 0.88$ Hz. $k_c(x - x_{ob})$ is (a) 1.9, (b) 2.7, (c) 3.8, (d) 4.7, (e) 5.7, (f) 6.6, (g) 7.6. The numbers on the graph are values of $k_c z$.

Some verification that this breaking induced flow does scale with the wave packet centre frequency can be seen in the results for the small scale plunging wave $f_c = 1.28$, $ak_c = 0.420$. These velocities scale very well with the large-scale case. The differences are thought to be due to the larger non-dimensional depth of the channel in the small scale $k_c d = -3.96$. This situation reduces the forced long wave velocity, because now the required return mass flux (to balance that in the carrier waves) is distributed over a larger effective depth. Also, the forward flowing induced flow penetrates about 20% deeper than in the large scale case. Otherwise the non-dimensional values of the breaking induced flow of approximately 0.02–$0.03C$ agree with the larger-scale case. The same large eddy is also generated.

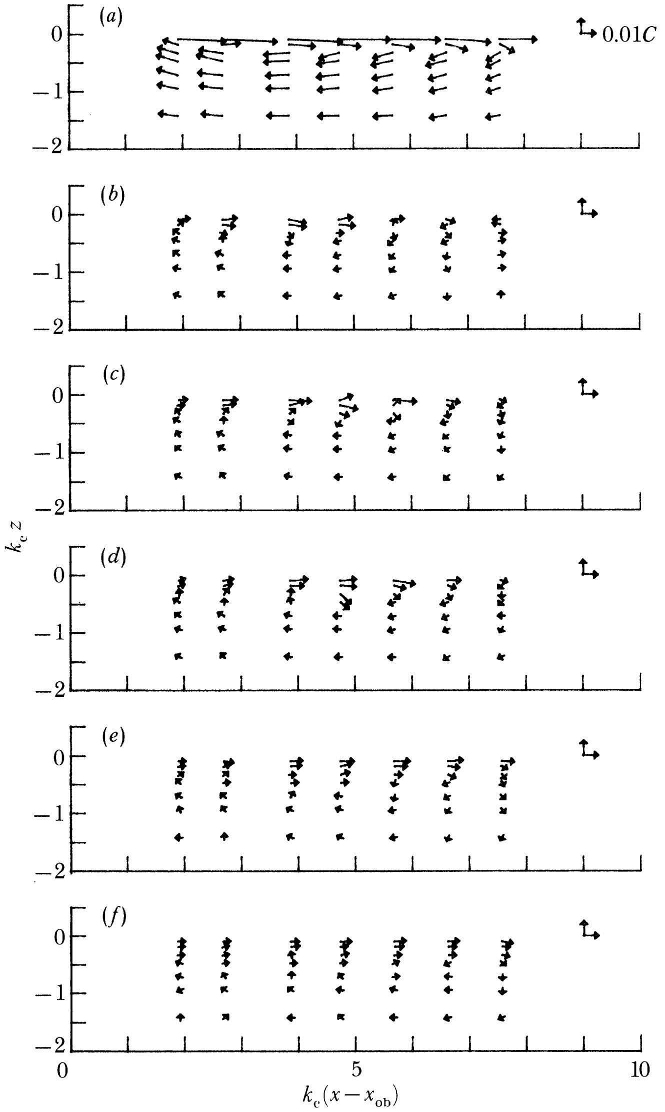

FIGURE 45. Mean velocity field for $f_c = 0.88$ Hz, $ak_c = 0.278$ (spilling) (a)–(f) as for figure 43.

5.3. *Turbulent velocities induced by breaking*

The measurements of horizontal and vertical turbulent velocities in the breaking region are shown in figures 46–49. As was discussed in §5.1, these signals represent the ensemble average of the square of the fluctuating velocity. This signal was low-pass filtered and then the square root was taken and plotted. For times after the wave packet has passed, this signal represents the turbulent ensemble mean square velocity to within an error of approximately 10 %. The instrument noise and random waves contribute at most 10 %. Measurements at times very close to breaking show a large increase in these turbulent velocities. Here, spikes due to bubbles crossing the measurement point, which contribute to the variance (noise) in the signal, are generally larger than 10 %, and it is not possible to resolve the accuracy of this measure of turbulence right at breaking in the bubbly flow. After several wave periods, however, the

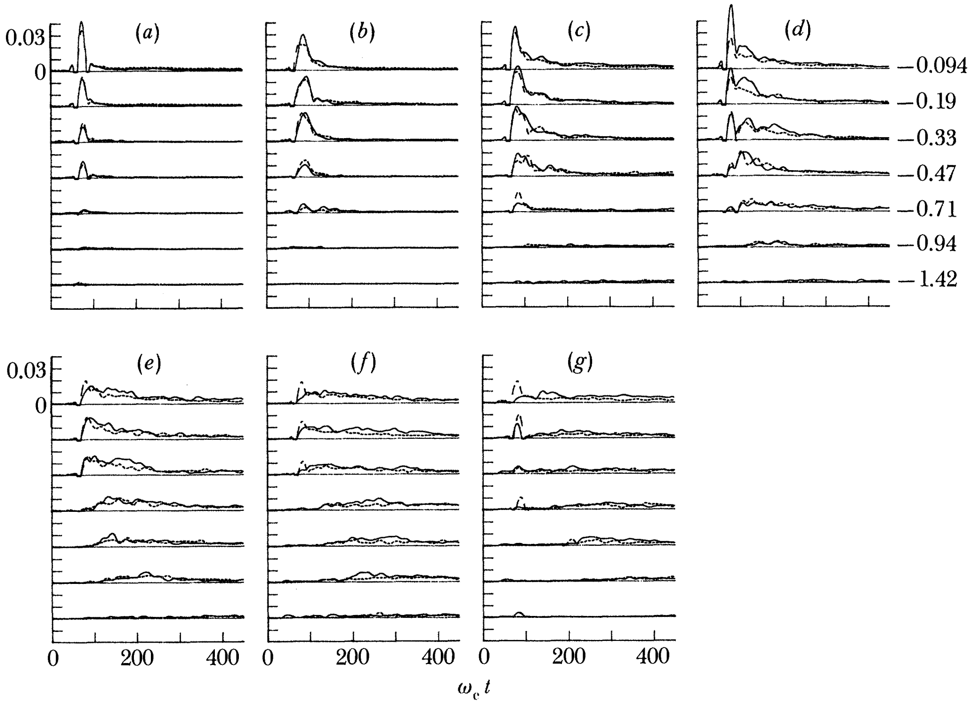

FIGURE 46. Time series of horizontal and vertical r.m.s. turbulence velocities. For $f_c = 0.88$ Hz, $ak_c = 0.352$ (plunging). Where $k_c(x-x_{ob})$ is (*a*) 0.94, (*b*) 1.9, (*c*) 3.0, (*d*) 3.8, (*e*) 4.7, (*f*) 5.7, (*g*) 6.6. The numbers on the graph are the values $k_c z$.

turbulent measurements are very reliable and show intensities of approximately $0.02C$. The plots in figure 46 correspond to the large scale plunging wave. Just downstream of breaking, at $k_c(x-x_{ob}) = 0.94$, the turbulence levels after breaking ($\omega_c t > 100$) are relatively small, about $0.005C$, and decay to nearly zero. The turbulence appears to be nearly isotropic in that the vertical and horizontal velocities are nearly equal for all time. From these measurements and observations, it seems that the turbulent region generated at breaking is advected further downstream. Measurements at these downstream stations show levels of turbulence initially of $0.02C$ and decaying slowly to $0.005C$ after over 60 wave periods. The depth of penetration is seen to increase further downstream showing turbulent r.m.s. velocity levels of $0.005C$ at $k_c z = -0.94$ (2–3 wave amplitudes) after 60 s. At $k_c(x-x_{ob}) = 6.6$ or one wavelength from breaking, turbulence r.m.s. velocities are still near $0.005C$ to depths of three wave amplitudes. The rate of vertical advance of the turbulent front can be estimated by the time delay of the observed increase in the turbulent velocity with depth (see measurements at $k_c(x-x_{ob}) = 4.7$ and 5.7. This rate of 0.01–$0.02C$ is of the same order as the turbulent r.m.s. velocities.

The spatial distribution of the r.m.s. fluctuations is shown in figure 47 at various time steps from observed breaking. Also plotted in this figure is the traced dye boundary digitized from films as described in §4. These boundaries correspond to the indicated time step after breaking. The horizontal extent of the turbulent region is established within 1–2 wave periods. Although the turbulence levels decay with depth, it is possible to define some spatial boundary where the turbulence is below $0.002C$, say. This depth of the turbulence increases in time and follows the dye boundary quite well. Note that in the top time step, high turbulence velocities are seen downstream of breaking, ahead of the instantaneous dye boundary. This is because the

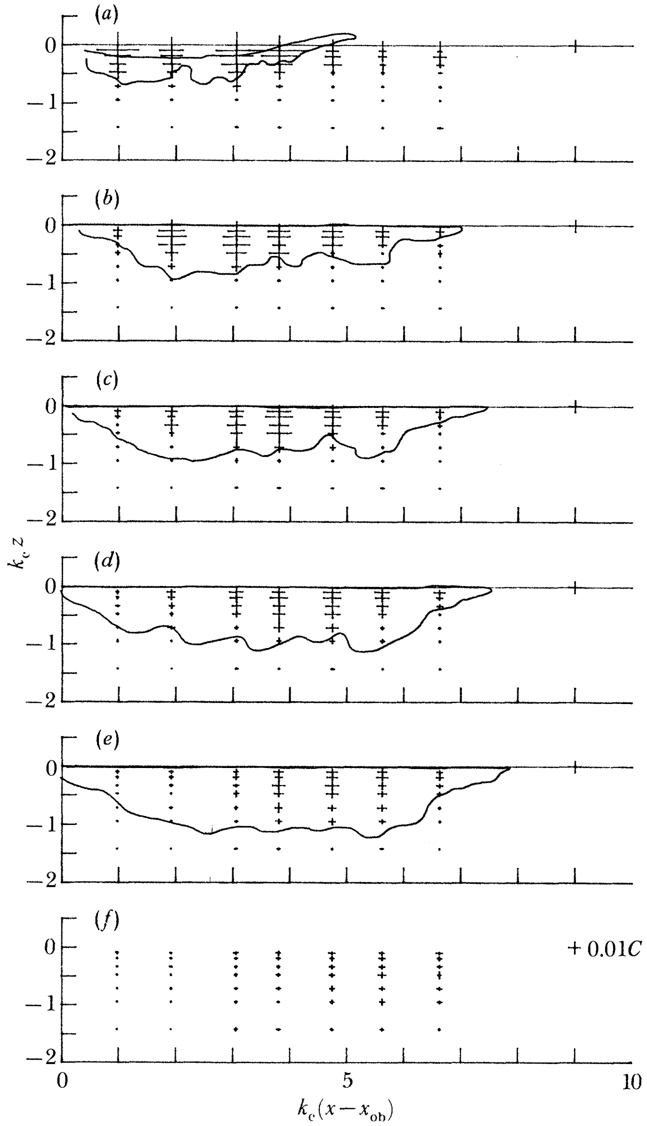

FIGURE 47. Turbulence r.m.s. velocities in the breaking region. $u_{\text{r.m.s.}}/C$ (horizontal bar), $w_{\text{r.m.s.}}/C$ (vertical bar) for $f_c = 0.88$ Hz, $ak_c = 0.352$ (plunging). Also shown is digitized dye trace at corresponding time after breaking. Bottom is $k_c z = -1.95$. (*a*)–(*f*) same as figure 43.

turbulence r.m.s. signal is low-pass filtered over several wave periods, while the dye boundary is moving rapidly here. At later times, where the motion is slowly changing in time, the dye boundary and extent of turbulence are in agreement. The results for the large-scale spilling wave (figures 48 and 49) show a similar growth of the turbulence in x and z and decay in time. The initial levels, however, are approximately $0.01C$ for this case, somewhat lower than in the plunging wave. The depth penetration is still appreciable for this less intense breaking, reaching two wave heights. Again, the dye boundary is a good estimator of the region where turbulent velocities are greater than $0.002C$. Some discrepancy is noted at 20 wave periods after breaking, where the dye appears deeper than the high levels of turbulence. Also, at the rear of the dye cloud, turbulence has decayed to negligible levels, whereas the dye remains.

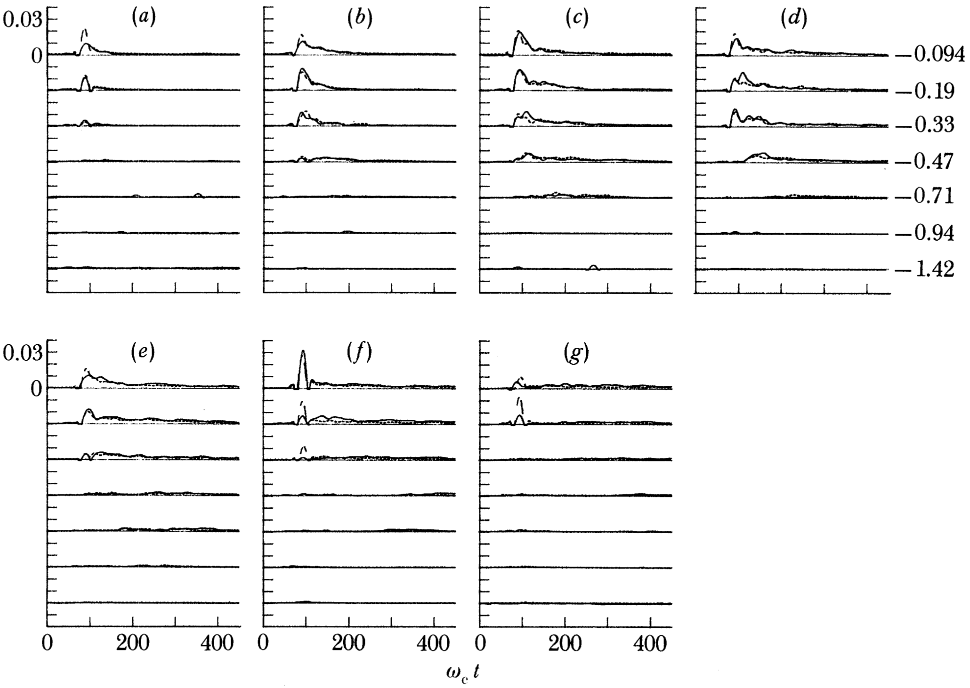

FIGURE 48. Time series of horizontal and vertical turbulence r.m.s. velocities (*a*)–(*g*) as for figure 46, except $ak_c = 0.278$ (spilling). The numbers on the graph are values of $k_c z$.

The magnitude of the turbulent r.m.s. velocity, the depth of penetration, and the time of decay, all appear to scale reasonably well with the length and timescales of the waves. This was proved by the results of the small-scale ($f_c = 1.28$ Hz) plunging wave group.

5.4. *The balance of total momentum and energy*

The conservation of horizontal momentum and conservation of energy is applied to the control volume enclosing the breaking region to attempt a balance between the measured fluxes crossing the vertical boundaries x_1 and x_2 (figure 5), and the increase with time of the corresponding densities (momentum and energy). These conservation equations are reviewed in Appendix A.

From equation (2.25), the conservation of total momentum is given by

$$\underline{\delta M} = -\overline{\overline{\Delta S}} + \overline{\overline{\tau}}. \tag{5.11}$$

Again, the underbar is a space integration from x_1 to x_2 and the double overbar is a time integration over long time, typically 40–80 s or 40–80 carrier wave periods. The change in the momentum flux is

$$\overline{\overline{\Delta S}} = \overline{\overline{\Delta S}}_{\mathrm{cw}} + \rho g d \overline{\overline{\Delta \eta}}. \tag{5.12}$$

The momentum flux lost from the carrier waves, $\overline{\overline{\Delta S}}_{\mathrm{cw}}$, has been measured from the surface displacement variance and is plotted as $\Delta\overline{\overline{\eta^2}}/\overline{\overline{\eta_0^2}}$ as a function of ak_c in figure 15. The dimensional value of $\overline{\overline{\Delta S}}_{\mathrm{cw}}$ is computed for each of the three wave cases where the detailed velocity measurements were made. It can be shown that

$$\overline{\overline{\eta_0^2}} = \tfrac{1}{2}a^2/\Delta f, \tag{5.13}$$

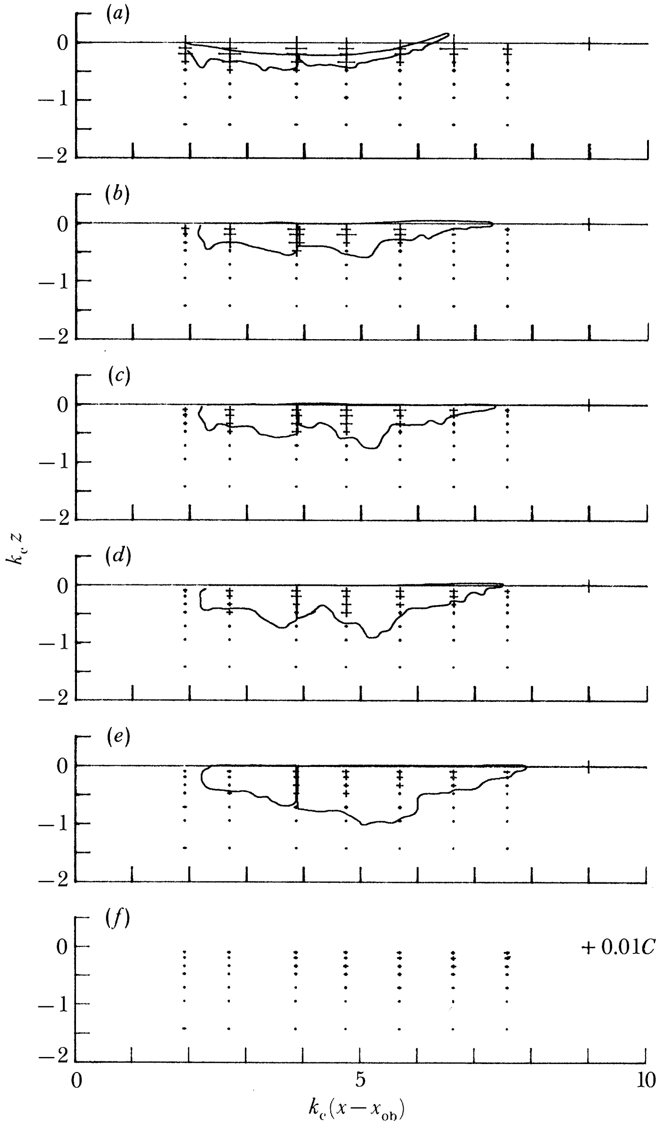

FIGURE 49. Turbulence r.m.s. velocities for $f_c = 0.278$ Hz (spilling). (a)–(f) as for figure 47. Contour is two dye tracings spliced together from separate runs of the breaking wave.

where a is the input wave amplitude $a = a_n N$, and Δf is the bandwidth of the packet. The number of input frequency components is $N = 32$. For the case of $f_c = 0.88$ Hz, $ak_c = 0.352$. $\Delta f/f_c = 0.73$ we have $\Delta f = 0.643$ Hz and $k_c = 3.25$ 1/m. Then $\overline{\overline{\eta_0^2}} = 90.7$ cm^2 s. This compares with the measured value at the reference station of 90.1 cm^2 s, showing that the theoretical value of $\overline{\overline{\eta_0^2}}$ can be used to compute the dimensional form of the results in figure 15.

Then
$$\overline{\overline{\Delta S}}_{\text{cw}} = \rho g \overline{\overline{\Delta \eta^2}}\,[(2C_g/C)-\tfrac{1}{2}]. \tag{5.14}$$

For this breaking case, figure 15 shows that
$$\overline{\overline{\Delta\eta^2}}/\overline{\overline{\eta_0^2}} = 0.24,$$
then
$$\overline{\overline{\Delta S}}_{\text{cw}} = 1.4\times 10^4 \text{ cm}^3\text{ s}^{-1}.$$

This is normalized by multiplying by $k_c^3/\omega_c\rho$ and the results for the three breaking wave cases is shown in table 2.

The second term on the right in equation (5.12) is the change in the time integrated setdown under the packet and represents the loss of momentum flux from the forced wave. When integrated over the packet, excluding the setup of the transient waves propagating away at $C_g = (gd)^{\frac{1}{2}}$, this is comparable with the loss in ΔS_{cw}.

Table 2. Momentum balance in carrier waves

(δM represents the positive momentum left in the breaking region after four wave periods from breaking. ΔS, δM are normalized by multiplying by $k_c^3/\omega_c\rho$.)

		$\overline{\overline{\Delta\eta^2}}/\overline{\overline{\eta_0^2}}$	$\overline{\overline{\Delta S}}_{cw}$	$\delta \underline{M}$	in current (%)
plunging					
$f_c = 0.88$ Hz	$ak_c = 0.352$	0.24	0.086	0.050	58
$f_c = 1.28$ Hz	$ak_c = 0.420$	0.19	0.076	0.065	86
spilling					
$f_c = 0.88$ Hz	$ak_c = 0.278$	0.10	0.024	0.02	83

The total momentum, $\underline{M}$, in the control volume is given by

$$\underline{M} = \int_{x_1}^{x_2}\int_{-d}^{\eta} u\rho \,\mathrm{d}z\,\mathrm{d}x, \tag{5.15}$$

as the fluid in the control volume is initially quiescent. Because the volume integral of the turbulent fluctuations is zero, the total horizontal momentum was computed using $\langle \overline{u} \rangle$, the mean velocity. Elemental areas were computed around each measurement point and multiplied by the corresponding measured mean velocity. These were then summed over the 49 elemental areas. This measured total momentum is plotted in figure 50. These time histories show, first, the positive going momentum due to the long transient wave propagating ahead of and away from the packet at $C_g = (gd)^{\frac{1}{2}}$. This wave is discussed by McIntyre (1981) and Benjamin (1970). The forced wave negative return flow is seen as the packet crosses the integration region. Note that the Stokes drift should come close to balancing this; however, measurements were not taken above the still-water line, where much of this flux is located; therefore the plot shows a net negative momentum here.

The total momentum is then seen to become very close to zero, which it should in deep water. The momentum in the positive flowing surface drift is roughly balanced by the lower return flow. Apparently, the carrier waves lose momentum, which goes into a surface current, but because the packet envelope decreases in amplitude due to breaking, so does the forced wave and thus its lost momentum is left behind. This lost momentum from the forced waves is sufficient to balance the positive flow above. Thus the eddy is generated, as was shown in figure 43.

Put another way, the momentum in the finite length wave packet upstream of breaking is zero (McIntyre 1981). Similarly, downstream of breaking it is also zero, so there can be no net momentum left behind. In shallow water, the momentum is slightly negative according to equation (A 14). If a percentage of this negative flow is lost from the packet it will show up as a negative momentum in the breaking region. These results, shown in figure 50, seem to support this, Also evident is a slow oscillation of period *ca.* 28 s, which corresponds to the

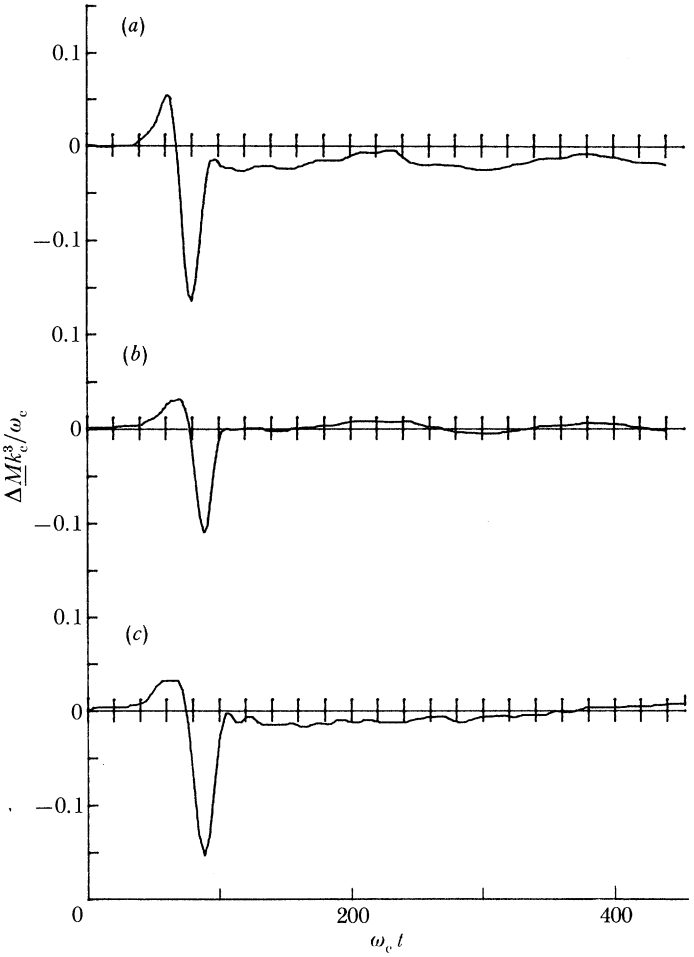

FIGURE 50. Total momentum in the breaking region as a function of time. $f_c = 0.88$ Hz with (*a*) plunge, (*b*) spill, (*c*) $f_c = 1.28$ Hz plunge.

TABLE 3. ENERGY BALANCE OVER THE BREAKING REGION

(δE represents the total energy in the breaking region after four wave periods from breaking. ΔF, δE are normalized by multiplying by k_c^2/C^2.)

		$\overline{\overline{\Delta\eta^2}}/\overline{\overline{\eta_0^2}}$	$\overline{\overline{\Delta F}}$	$\delta \underline{E}$	$\delta E/\overline{\overline{\Delta F}}$ (%)
plunging					
$f_c = 0.88$ Hz	$ak_c = 0.352$	0.24	0.076	2.5×10^{-3}	3.3
$f_c = 1.28$ Hz	$ak_c = 0.420$	0.19	0.072	2.5×10^{-3}	3.5
spilling					
$f_c = 0.88$ Hz	$ak_c = 0.278$	0.10	0.02	5.0×10^{-4}	2.5

fundamental mode of oscillation in the channel. The long-wave velocity is $C_g = (gd)^{\frac{1}{2}} = 2.4$ m s^{-1}. The length of the channel is approximately 30 m giving the first mode oscillation of period approximately ($T = 2L/C_g$) approximately 25 s, which is close to that measured.

The results showing zero net horizontal momentum in the breaking region are consistent with the physics; however, we are interested in predicting the magnitude of the momentum transferred to surface currents from the carrier waves. This we can estimate by assuming that the negative going flow, set up by the forced wave, U_2, is uniform in depth (figure 51). (This

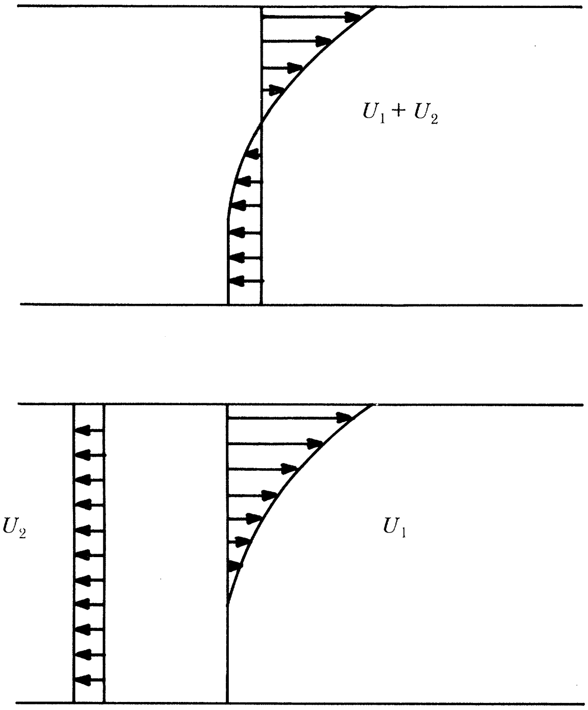

FIGURE 51. Model of mean velocity distribution in the breaking region. U_1 induced by carrier wave breaking, U_2 set up by forced wave.

is reasonable, because the forced wave is long.) Also we assume that the flow induced by momentum lost from the carrier waves U_1, decays to zero at some depth above the bottom. Then the velocity near the bottom is completely due to U_2 and this can be subtracted throughout the depth to obtain U_1. This we have done for each time step from breaking. The volume integrated momentum was then computed to obtain the plots in figure 52. From these plots, the total momentum left in the breaking region after four wave periods has been estimated and listed in table 2. Comparing the momentum flux loss from the carrier waves $\overline{\overline{\Delta S}}_{cw}$ with that in the breaking region, it can be seen that 83 % or 86 % is accounted for in the mean flow for the spilling wave and the small scale plunging waves. Thus agreement is considered good given the estimation methods and assumptions. The discrepancy for the large scale plunging wave is difficult to explain; however, it may be noticed that $\overline{\overline{\Delta\eta^2}}/\overline{\overline{\eta_0^2}}$ from figure 15 is higher than in the other scales of plunging waves which leads to this discrepancy. We attributed this to additional spray and thus larger losses; however, these momentum balance results tend to cast some doubt on the high losses. Possibly finite depth effects are responsible. On the other hand, the error may be in the estimate of $\delta \underline{M}$ and the assumption that the breaking effects of the carrier waves are not felt near the bottom. Possibly, there is cancellation between U_1 and U_2 (figure 51) at the lower depth and we underestimate U_2 which would give this error between ΔS_{cw} and $\delta \underline{M}$.

Overall, however, these momentum balance results are encouraging, showing that indeed breaking can directly transfer horizontal momentum from waves to currents.

A similar balance is performed on the energy. From (2.35) the conservation of total energy is given by:

$$\delta \underline{E}+\Delta F = -\rho \underline{\overline{\overline{\int_{-d}^{\eta} \epsilon \, \mathrm{d}z}}}. \tag{5.16}$$

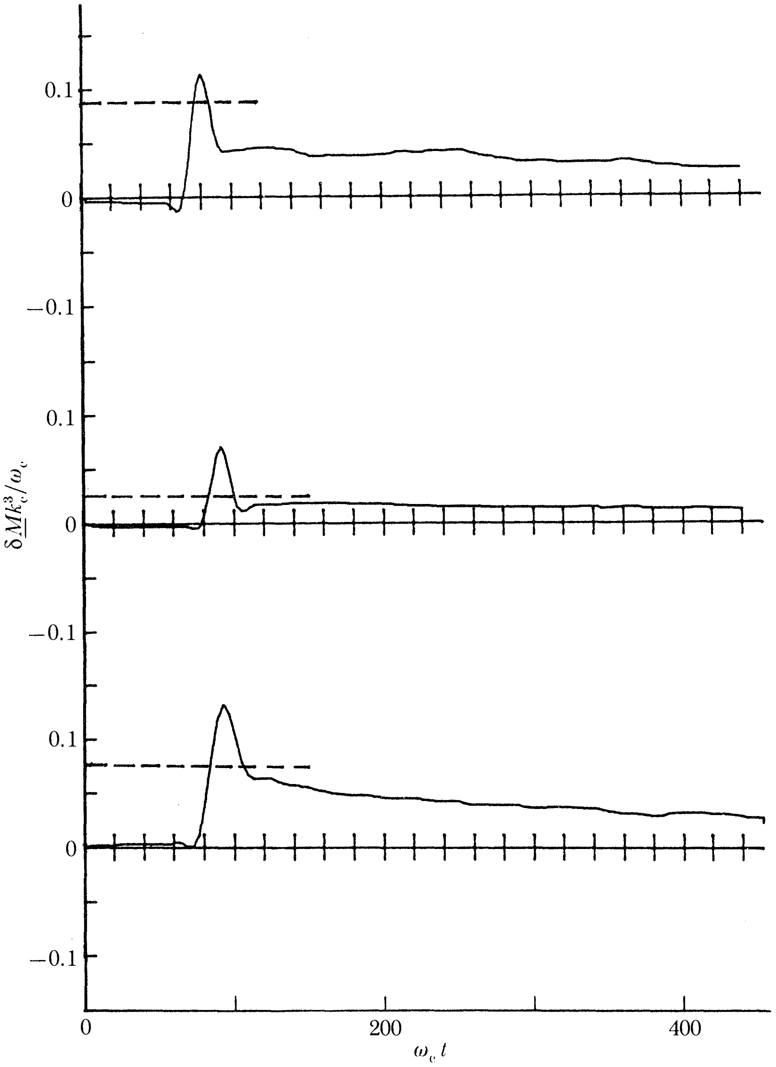

FIGURE 52. Total momentum estimated to be induced by breaking carrier waves. Also shown is $\overline{\overline{\Delta S}}_{cw}$ (– – –) the time integrated change in momentum flux. (*a*)–(*c*) as for figure 50.

The difference in the energy flux crossing x_1 and x_2 is

$$\overline{\overline{\Delta F}} = C_g[\overline{\overline{E}}_{x_2} - \overline{\overline{E}}_{x_1}], \tag{5.17}$$

where C_g is assumed equal at these stations. Then

$$\overline{\overline{\Delta F}} = \rho g C_g \overline{\overline{\Delta \eta^2}}. \tag{5.18}$$

The measured values of $\overline{\overline{\Delta\eta^2}}/\overline{\overline{\eta_0^2}}$ can be used to compute the change in the energy flux as was done for the momentum balance from

$$\overline{\overline{\Delta F}} = \tfrac{1}{2}\rho g C_g (\overline{\overline{\Delta\eta^2}}/\overline{\overline{\eta_0^2}})\, a^2/\Delta f. \tag{5.19}$$

The increase in the total energy in the breaking region (integration region) is due to the kinetic energy of the mean motions together with the fluctuating turbulent motion. The still-water level returns to its initial level after the waves have passed so the change in potential energy is assumed to be zero. The total energy is given by

$$\underline{\Delta E} = \tfrac{1}{2}\rho \int_{x_1}^{x_2} \int_{-d}^{\eta} \langle u_i^2 \rangle \,\mathrm{d}x\,\mathrm{d}z, \tag{5.20}$$

where $u_i^2 = u^2+w^2+v^2$. The contribution to the kinetic energy is computed by

$$\langle u_i^2 \rangle = \langle u \rangle^2 + \langle w \rangle^2 + \langle u'^2 \rangle + \langle w'^2 \rangle + \langle v'^2 \rangle. \tag{5.21}$$

Because the transverse velocity, v, was not measured, the assumption was made that the mean motion was two dimensional giving

$$\langle v \rangle^2 = 0. \tag{5.22}$$

The turbulence, being three dimensional, must include energy from the transverse direction so we set

$$\langle v'^2 \rangle = \langle w'^2 \rangle, \tag{5.23}$$

because $\langle w'^2 \rangle$ was typically lower than $\langle u'^2 \rangle$. We do not have a strong basis for this assumption; however, it seems to be a better assumption than setting it to zero.

The squared velocities were multiplied by the elemental areas surrounding each measurement location and then summed. The results are plotted in figure 53 for the three breaking cases. The kinetic energy is normalized by k_c^2/C^2 to make the comparison between the

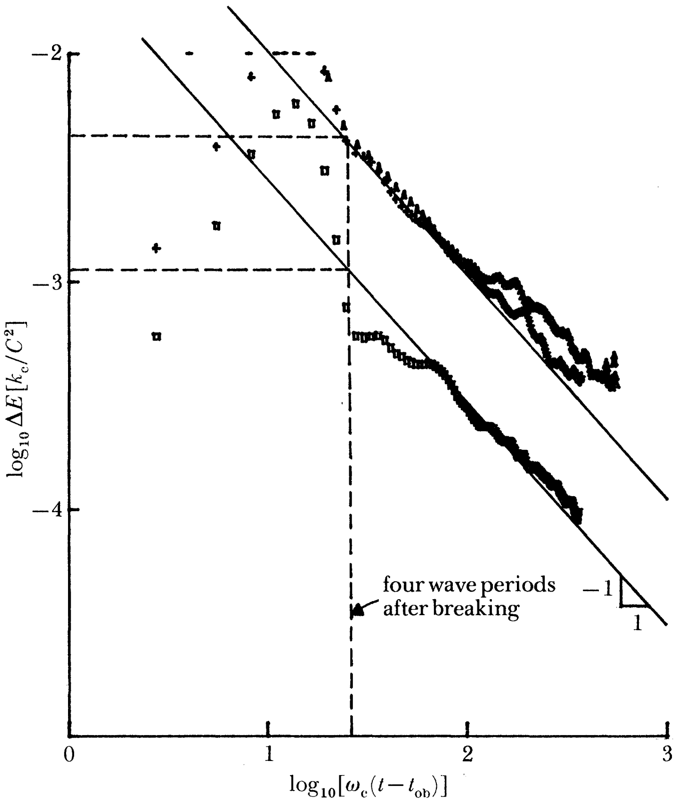

FIGURE 53. Total kinetic energy in the breaking region as a function of time. For $f_c = 0.88$ Hz, $ak_c = 0.352$ plunge (+), $ak_c = 0.278$ spill (□), $f_c = 1.28$ Hz, $ak_c = 0.420$ plunge (△).

large-scale plunging and small-scale plunging. At four wave periods after breaking, the decay of the total kinetic energy with time is seen to be proportional to $\omega_c(t-t_{ob})^{-1}$, where t_{ob} = time of observed breaking. This holds for both scales of plunging, and for the large-scale spilling.

The normalized kinetic energy measured in the breaking region after four wave periods is estimated from figure 52 and equation (5.20). These results are summarized in table 2. From this energy balance, it is shown that only a small percentage (2–4 %) of the energy lost by the waves in breaking remains in the breaking region after four wave periods. From this time on, the kinetic energy decays as t^{-1}. From these measurements it is estimated that 96–98 % of the energy goes into turbulence and is dissipated within four wave periods.

5.5. *Decay of turbulence and dissipation estimates*

The decay rate of the total turbulent kinetic energy is needed in estimating dissipation and diffusion rates in turbulent flow generated by breaking. Plotted in figure 54 is the volume integrated turbulent kinetic energy contribution from the horizontal and vertical velocities u'^2, w'^2. The decay of each of these contributions also follows a t^{-1} power law, where the time origin is the time of observed breaking. The deviation from isotropy can be seen in the lower energy level in the vertical velocity. Assuming u'^2 also decays like t^{-1} we have that the total turbulent kinetic energy (TKE) is given by

$$\text{TKE} = \tilde{u}^2\mathscr{V} \propto t^{-1}, \tag{5.24}$$

where $\mathscr{V}$ is the volume of the turbulent region, and $\tilde{u}$ is a velocity scale. From the dye mixing results presented in §4 we showed that

$$\mathscr{V} \propto \text{area} \propto l^2 \propto t^{\frac{1}{2}}, \tag{5.25}$$

where l is an integral length scale of the turbulence. Then

$$\tilde{u}^2 \propto t^{-\frac{3}{2}} \tag{5.26}$$

and

$$\tilde{u} \propto t^{-\frac{3}{4}}. \tag{5.27}$$

The dissipation rate of total turbulent kinetic energy is

$$\epsilon\mathscr{V} \equiv \mathrm{d}/\mathrm{d}t\,(\text{TKE}) \propto t^{-2}, \tag{5.28}$$

where ϵ is the dissipation rate per unit mass. Whence,

$$\epsilon \propto t^{-\frac{5}{2}}. \tag{5.29}$$

A separate estimate of the dissipation, ϵ, based on isotropic turbulence given by Taylor (1935) assumes a large Reynolds number flow and that the large eddies supply energy to the small eddies at a rate equal to the dissipation rate. The energy is dissipated at high wavenumbers (small eddies). In this flow field the Reynolds number is $O(10^3–10^4)$, which is large compared with 1.

The rate of energy transfer by the large eddies is given by

$$\epsilon \propto \tilde{u}^3/l. \tag{5.30}$$

By using the power laws for $\tilde{u}$ and l as measured above

$$\epsilon \propto t^{-\frac{5}{2}}. \tag{5.31}$$

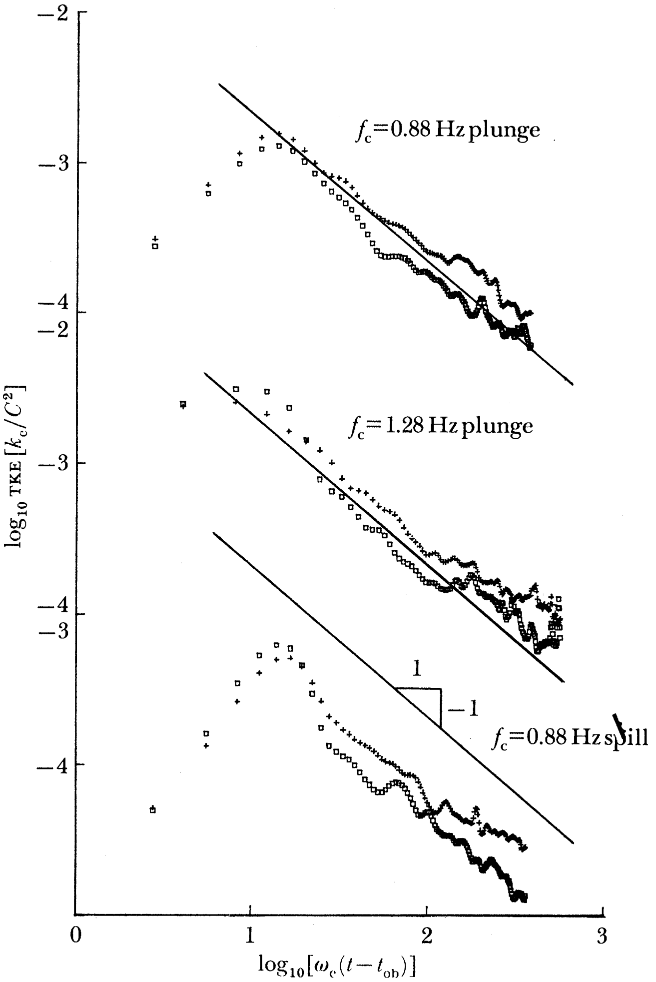

FIGURE 54. Turbulent contribution to volume integrated kinetic energy u'^2 (+), w^2 (□). Line of slope -1 is drawn at same relative location in each plot for reference.

This independent estimate of the time dependence of ϵ is in agreement with the estimate given above from equation (5.29) which gives support to the accuracy of these estimated power laws based solely on the measurements.

Our estimates of $\tilde{u}$ and l also show that an eddy diffusivity κ would vary as

$$\kappa \propto \tilde{u}_t \, l \propto t^{-\frac{5}{2}}, \tag{5.32}$$

which is also the time dependence for the Reynolds number of the flow. Note that the time dependence of these variables $\tilde{u}$, ϵ and κ in this unsteady breaking wave do not agree with measurements made on a steady spilling breaker (Battjes & Sakai 1981), which were shown to match the model of a wake flow.

6. CONCLUSIONS

Further development of empirical results of the kind presented here may be used in conjunction with breaking wave statistics to estimate global loss rates over the wave field. Some preliminary estimates of this have already been made (Melville & Rapp 1985). The average measured loss of 10% per breaking wave group was used in conjunction with an estimate by Thorpe & Humphries (1980) of the horizontal distance between breaking waves, to arrive at an estimate of the gradient of the momentum flux lost from the wave field. The order of this term agrees well with the corresponding wind input. This implies that essentially all the momentum flux from the wind is going through the wave field and being lost in breaking. This, then, explains the much slower growth of the wave field as measured by Mitsuyasu (1985), because the full wind input is not expected to go into wave growth.

An important result of the experiments is that the measured quantities scaled well with the packet centre frequency and wavelength. Some discrepancy was reported for the more vigorous plunging at the large scale. The loss of momentum flux and the horizontal extent of mixing were larger than in the smaller scales. We believe that this was due to the air entrainment and spray in this particular case. Resolution of this issue can only be achieved with larger-scale experiments.

In summary, the measurements show the quantitative importance of the breaking process in wave modelling, in mixing and in transferring horizontal momentum from the wind to currents. As far as we are aware, these are the first controlled experimental measurements of these processes in realistic unsteady deep-water breaking. The large-scale circulation left behind by the breaking has, to our knowledge, not been previously observed.

We thank Eng-Soon Chan who collaborated in preliminary experiments and Jack Crocker for his construction of the wave-making facility and associated equipment. This work was supported by National Science Foundation Grants 8214746-OCE and 8614889-OCE.

APPENDIX A: SECOND-ORDER ESTIMATES OF THE MASS, MOMENTUM AND ENERGY FLUXES

Following Dysthe (1979) the free surface displacement is represented to second order by

$$\eta(x,t) = \bar{\eta} + \eta', \tag{A 1}$$

where

$$\eta' = A(x_1, t_1)\,\mathrm{e}^{\mathrm{i}\theta} + A_2(x_1, t_1)\,\mathrm{e}^{\mathrm{i}2\theta} \quad (\theta = k_c x - \omega_c t). \tag{A 2}$$

The velocity potential is represented by

$$\phi = \bar{\phi} + BF(Z)\,\mathrm{e}^{\mathrm{i}\theta} + B_2 F_2(Z)\,\mathrm{e}^{2\mathrm{i}\theta} \tag{A 3}$$

The coefficients A, A_2, B, B_2, and the forced wave variables, $\bar{\eta}$, $\bar{\phi}$ are all assumed to be functions of slow time and space variables,

$$t_1 = \mu t, \quad x_1 = \mu x, \tag{A 4}$$

where $\mu = \Delta\omega/\omega_c$ gives the envelope steepness of $\mu ak = \mu\epsilon$ and $\epsilon = ak$ is the carrier wave steepness. Also, $\bar{\phi}$ is allowed a slow depth dependence $z_1 = \mu z$. The horizontal and vertical velocities are given by

$$u = \partial\phi/\partial x, \quad w = \partial\phi/\partial z \tag*{(A 5), (A 6)}$$

where

$$\partial/\partial x \rightarrow \partial/\partial x + \mu\,\partial/\partial x_1, \quad \partial z \rightarrow \partial z + \mu\,\partial z^1.$$

The velocities are represented by

$$u = \bar{u} + u^{(1)} + u^{(2)} \tag{A 7}$$

$$w = \bar{w} + w^{(1)} + w^{(2)} \tag{A 8}$$

The wave variables $\bar{\phi}$, $\bar{\eta}$, $\bar{u}$, $\bar{w}$ can be determined for $kd = O(ka)^{-1}$ as shown by Dysthe (1979) with the following set of equations:

$$\nabla^2\bar{\phi} = 0, \qquad 0 < z < -d, \tag{A 9}$$

$$\partial\bar{\phi}/\partial t + g\bar{\eta} = 0, \qquad z = 0, \tag{A 10}$$

$$\bar{w} - \partial\bar{\eta}/\partial t = \tfrac{1}{2}\omega\,\partial/\partial x\,|A|^2, \qquad z = 0, \tag{A 11}$$

$$\bar{w} = \partial\bar{\phi}/\partial z = 0, \qquad z = -d. \tag{A 12}$$

Assuming a packet of permanent form so that

$$\partial/\partial x \rightarrow (-1/C_g)\,\partial/\partial t,$$

where C_g is the group velocity, the above set of equations is solved using Fourier transform methods provided $|A|^2$ is known and we can set

$$|A|^2 = 2\overline{\eta^2}. \tag{A 13}$$

These forced wave variables were earlier derived by Longuet-Higgins & Stewart (1962) using a perturbation expansion approach and expressed as a sum of Fourier components. Dysthe (1979) showed the two methods give the same result. The important results of their analysis show that in the case when the depth is small compared with the group length, the force wave velocity $\bar{u}$, being constant in depth, can be expressed in terms of the local surface displacement variance by

$$\bar{u} = \frac{-g}{d}\left(\frac{C_g}{2(gd - C_g^2)} + \frac{1}{C}\right)\overline{\eta^2} \tag{A 14}$$

and

$$\bar{w} = 0, \quad \bar{\eta} = \left(\frac{-g}{\rho(gd - C_g^2)}\right)\overline{\eta^2}. \qquad \text{(A 15), (A 16)}$$

In deep water it is not generally possible to express the forced wave variables in terms of the local radiation stress, $\overline{\eta^2}$, since the solution is a summation of Fourier components that decay in depth at different rates. One should refer to Longuet-Higgins & Stewart (1962, equation (3.13)). In the sample case of periodic packets where $|A|^2 = A_0^2[1 + \cos\mu k(x - C_g t)]$, the forced wave variables are given in terms of the local radiation stress (Rapp 1986).

Mass flux

Upon substitution of the horizontal velocity due to the carrier waves and forced wave into equation (2.18) for the mass flux the following is obtained

$$M = \rho\overline{\eta'^2}\,\omega_c \coth k_c d + \rho\int_{-d}^{\bar{\eta}} \bar{u}\,\mathrm{d}z. \tag{A 17}$$

The first term on the right represents the mass flux due to the carrier waves or Stokes drift. The second term is the mass flux in the return flow due to the forced wave. For water, shallow compared with the group length, equation (A 14) is substituted for $\bar{u}$ and the following is obtained

$$M = -\tfrac{1}{2}\rho g(C_g/(gd - C_g^2))\,\overline{\eta^2}. \tag{A 18}$$

(Longuet-Higgins & Stewart 1962, equation (3.36)).

In this situation the net mass flux is in the opposite direction to the carrier wave propagation. Physically this must be true, because by conservation of mass the return flow must not only balance the Stokes drift but also account for the fluid displaced by the forced long-wave depression under the group. In the case of very deep water the net mass flux must go to zero,

$$M = 0. \tag{A 19}$$

In this case the Stokes drift in the carrier waves is exactly balanced by the return flow in the forced wave. This fact has been previously noted by Longuet-Higgins & Stewart (1964), and also shown by R. Iusim & M. Stiassnie (personal communication) using Dysthe (1979). This also implies that the total momentum integrated over the packet length and depth is also zero as is pointed out by McIntyre (1981).

Momentum flux

The total time averaged horizontal momentum flux, equation (2.19) can be put in terms of u, w, η by substituting for the pressure. The pressure $p(z)$ is obtained by integrating the vertical momentum equation over depth, and using the kinematic free surface boundary condition, which yields

$$S = \tfrac{1}{2}\rho g\overline{(\eta+d)^2} + \rho\overline{\int_{-d}^{\eta}(u^2-w^2)\,\mathrm{d}z} + \rho\overline{\int_{-d}^{\eta}\frac{\partial}{\partial t}\int_{z}^{\eta} w\,\mathrm{d}z\,\mathrm{d}z'} + \rho\overline{\int_{-d}^{\eta}\frac{\partial}{\partial x}\int_{z}^{\eta} uw\,\mathrm{d}z\,\mathrm{d}z'}. \tag{A 20}$$

The velocities and surface displacement may contain wave components, forced waves, and turbulence. In general one may expect interactions between these motions which makes separating S into component parts impossible. However, if the timescales of the motions are sufficiently separated, then the averaging will cancel these terms, and there is no interaction. At stations far from breaking, turbulent velocities are zero and the wave packet is indeed slowly varying, making $\bar{u}$ slowly varying. A separation of scales is then possible.

Substituting for the various wave variables and neglecting terms higher than second order, the momentum flux becomes

$$S = \rho g\overline{\eta^2}\left(\frac{2kd}{\sinh 2kd}+\tfrac{1}{2}\right) - \rho\int_{-d}^{0}\frac{\partial\bar{\phi}}{\partial t}\,\mathrm{d}z + O(\epsilon^3), \tag{A 21}$$

where the hydrostatic term $\tfrac{1}{2}\rho g d^2$ is neglected.

The first term is due to the carrier waves and the second term is due to the pressure of the forced wave. In shallow water, the forced wave pressure is constant in depth and hydrostatic and given by the free surface boundary condition,

$$\partial\bar{\phi}/\partial t + g\bar{\eta} = 0. \tag{A 22}$$

The momentum flux in this case is,

$$S = \rho g\overline{\eta^2}[(2kd/\sinh 2kd)+\tfrac{1}{2}] + \rho g\bar{\eta}d, \tag{A 23}$$

and is that given by Longuet-Higgins & Stewart (1962) and Whitham (1962). An alternative form is given by

$$S = \rho g\overline{\eta^2}[(2C_{\mathrm{g}}/C)-\tfrac{1}{2}] + \rho g\bar{\eta}d, \tag{A 24}$$

where C_{g} is the linear group velocity and C is the linear phase speed.

In deep water the contribution from the carrier waves becomes

$$S_{\mathrm{cw}} = \tfrac{1}{2}\rho g \overline{\eta^2}. \tag{A 25}$$

Higher-order corrections were obtained in the derivation of the momentum flux for the purpose of estimating the errors in our use of the second order estimate. These are given in Rapp (1986). The higher-order corrections are a result of the steepness of the envelope, and involve terms containing $\partial|A|^2/\partial x$ and $\partial A/\partial x\,\partial A/\partial x$, which are of $O(\epsilon^4)$. The steepness of the carrier waves gives terms proportional to $|A|^4$ and $|B_2|^2$, also of $O(\epsilon^4)$. The forced long wave velocities $\bar{u}^2, \bar{w}^2$ also contribute to the momentum flux but are of order $O(\epsilon^6)$ in deep water. In shallow water, compared with the group length, $\bar{w} = 0, \bar{u}^2 = \epsilon^4$. An interaction term proportional to $\bar{\eta}|A|^2$ was also found. These corrections are used in §3 to estimate the order of the errors in the measurements of the momentum flux.

Energy flux

The second-order estimate of the energy flux due to waves is given by

$$F = C_g E + O(\epsilon^3), \quad \text{where} \quad E = \tfrac{1}{2}\rho g \overline{\eta^2} \tag{A 26}$$

(see Whitham 1962), where his mean velocity is considered second order.

REFERENCES

Banner, M. L. & Fooks, E. H. 1985 On the microwave reflectivity of small-scale breaking water waves. *Proc. R. Soc. Lond.* A **399**, 93–103.

Banner, M. L. & Melville, W. K. 1976 On the separation of air flow over water waves. *J. Fluid Mech.* **77**, 825–842.

Banner, M. L. & Phillips, O. M. 1974 On the incipient breaking of small scales waves. *J. Fluid Mech.* **65**, 647–656.

Battjes, J. A. & Sakai, T. 1981 Velocity field in a steady breaker. *J. Fluid Mech.* **111**, 421–437.

Benilov, A. Ju. 1978 The error of the linear filtration method in the analysis of the fluctuations of random fields of the near water atmospheric layer and the upper ocean. *Oceanology* **18**, 28–34.

Benjamin, T. B. 1970 Upstream influence. *J. Fluid Mech.* **40**, 49–79.

Chan, E. S. 1985 Deep water breaking wave forces on structures, Sc.D. thesis, Massachusetts Institute of Technology, U.S.A.

Clay, C. S. & Medwin, H. 1977 *Acoustical oceanography*. New York: John Wiley.

Compte-Bellot, G. & Corrsin, S. 1966 The use of a contraction to improve the isotropy of grid generated turbulence. *J. Fluid Mech.* **25**, 657–682.

Donelan, M. A. 1978 Whitecaps and momentum transfer. In *Turbulent fluxes through the sea surface, wave dynamics and prediction*. Favre, Hasselmann, NATO Conf. Series. New York: Plenum Press.

Donelan, M. A., Longuet-Higgins, M. S. & Turner, J. S. 1972 Periodicity in whitecaps. *Nature, Lond.* **239**, 449–451.

Duncan, J. H. 1981 An experimental investigation of breaking waves produced by a towed hydrofoil. *Proc. R. Soc. Lond.* A **377**, 331–348.

Dysthe, K. B. 1979 Note on a modification to the nonlinear Schrodinger equation for application to deep water waves. *Proc. R. Soc. Lond.* A **369**, 105–114.

Greenhow, M. 1983 Free surface flows related to breaking waves. *J. Fluid Mech.* **134**, 259–275.

Hinze, J. O. 1959 *Turbulence: an introduction to its mechanism and theory*. New York: McGraw-Hill.

Holthuijsen, L. H. & Herbers, T. H. C. 1986 Statistics of breaking waves observed as whitecaps in the open sea. *J. phys. Oceanogr.* **16**, 290–297.

Keller, W. C., Jessup, A. T. & Melville, W. K. 1990 Measurements of sea spikes in radar backscatter at moderate incidence. *J. geophys. Res.* (In the press.)

Kitaigorodski, S. A., Donelan, M. A., Lumley, J. L. & Terray, E. A. 1983 Wave-turbulence interactions in the upper ocean. Part II: statistical characteristics of wave and turbulent components of the random velocity field in the marine surface layer. *J. phys. Oceanogr.* **13**, 1988–1999.

Kjeldsen, S. P. & Olsen, G. B. 1972 *Breaking waves* (16 mm film) Lyngby, Technical University of Denmark.

Kjeldsen, S. P., Vinge, T., Myrhaug, D. & Brevig, D. 1980 Kinematics of deep water breaking waves. In *Proc. 12th Offshore Tech. Conf.* Paper no. 3714. Houston, Texas.

Kwoh, D. S. W. & Lake, B. M. 1984 A deterministic, coherent dual-polarized laboratory study of microwave backscattering from water waves. Part 1. Short gravity waves without wind. *IEEE J. Ocean. Engng* **5**, 291–308.

Longuet-Higgins, M. S. 1953 Mass transport in water waves. *Phil. Trans. R. Soc. Lond.* A **345**, 535–581.

Longuet-Higgins, M. S. 1963 The generation of capillary waves by steep gravity waves. *J. Fluid Mech.* **16**, 138–159.

Longuet-Higgins, M. S. 1969 On wave breaking and the equilibrium spectrum of wind generated waves. *Proc. R. Soc. Lond.* A **310**, 151–159.

Longuet-Higgins, M. S. 1974 Breaking waves in deep or shallow water. *Proc. 10th Conf. on Naval Hydrodynamics*, pp. 597–605. M.I.T.

Longuet-Higgins, M. S. 1984 Statistical properties of wave groups in a random sea state. *Phil. Trans. R. Soc. Lond.* A **312**, 219–250.

Longuet-Higgins, M. S. & Stewart, R. W. 1961 The changes in amplitudes of short gravity waves on steady non-uniform currents. *J. Fluid Mech.* **10**, 529–549.

Longuet-Higgins, M. S. & Stewart, R. W. 1962 Radiation stress and mass transport in gravity waves, with application to surf-beats. *J. Fluid Mech.* **13**, 481–504.

Longuet-Higgins, M. S. & Stewart, R. W. 1964 Radiation stress in water waves; a physical discussion with application. *Deep Sea Res.* **11**, 529–562.

Longuet-Higgins, M. S. & Turner, J. S. 1974 An entraining plume model of a spilling breaker. *J. Fluid Mech.* **63**, 1–20.

Madsen, O. S. 1970 Waves generated by a piston-type wavemaker. *Proc. 12th Conf. Coastal Engng*, pp. 589–607.

Mei, C. C. 1983 *The applied dynamics of ocean surface waves.* New York: John Wiley.

Melville, W. K. 1982 The instability and breaking of deep-water waves. *J. Fluid Mech.* **115**, 165–185.

Melville, W. K. & Rapp, R. J. 1985 Momentum flux in breaking waves. *Nature, Lond.* **317**, 514–516.

Melville, W. K., Loewen, M. R., Felizardo, F. C., Jessup, A. T & Buckingham, M. J. 1988 The acoustic and microwave signatures of breaking waves. *Nature, Lond.* **336**, 54–59.

Mitsuyasu, H. 1985 A note on momentum transfer from wind to waves. *J. geophys. Res.* **90**, 3343–3345.

McIntyre, M. E. 1981 On the wave momentum myth. *J. Fluid Mech.* **106**, 331–347.

Openheim, A. V. & Shafer, R. W. 1975 *Digital signal processing.* Englewood Cliffs, New Jersey: Prentice-Hall.

Peregrine, D. H. 1983 Breaking waves on beaches. *A. Rev. Fluid Mech.* **15**, 149–178.

Peregrine, D. H. & Svendsen, I. A. 1978 Spilling breakers, bores, and hydraulic jumps. *Proc. 16th Conf. on Coastal Engng*, pp. 540–550. Hamburg.

Phillips, O. M. 1977 *The dynamics of the upper ocean.* Cambridge University Press.

Rapp, R. J. 1986 Laboratory measurements of deep water breaking waves, Ph.D. thesis, Massachusetts Institute of Technology, U.S.A.

Shum, K. T. & Melville, W. K. 1984 Estimates of joint statistics of amplitudes and periods of ocean waves using an integral transform technique. *J. geophys. Res.* **89**, 6467–6476.

Taylor, G. I. 1935 Statistical theory of turbulence. *Proc. R. Soc. Lond.* A **151**, 421.

Thornton, E. B. 1979 Energetics of breaking waves within the surf zone. *J. geophys. Res.* **84**, 4931–4938.

Thorpe, S. A. & Humphries, P. N. 1980 Bubbles and breaking waves. *Nature, Lond.* **283**, 463–465.

Van Dorn, W. G. & Pazan, S. E. 1975 Laboratory investigation of wave breaking, Scripps Inst. of Ocean. Ref. No. 75-21, *AOEL rep. no. 71.*

Whitham, G. B. 1962 Mass. momentum and energy flux in water waves. *J. Fluid Mech.* **12**, 135–147.

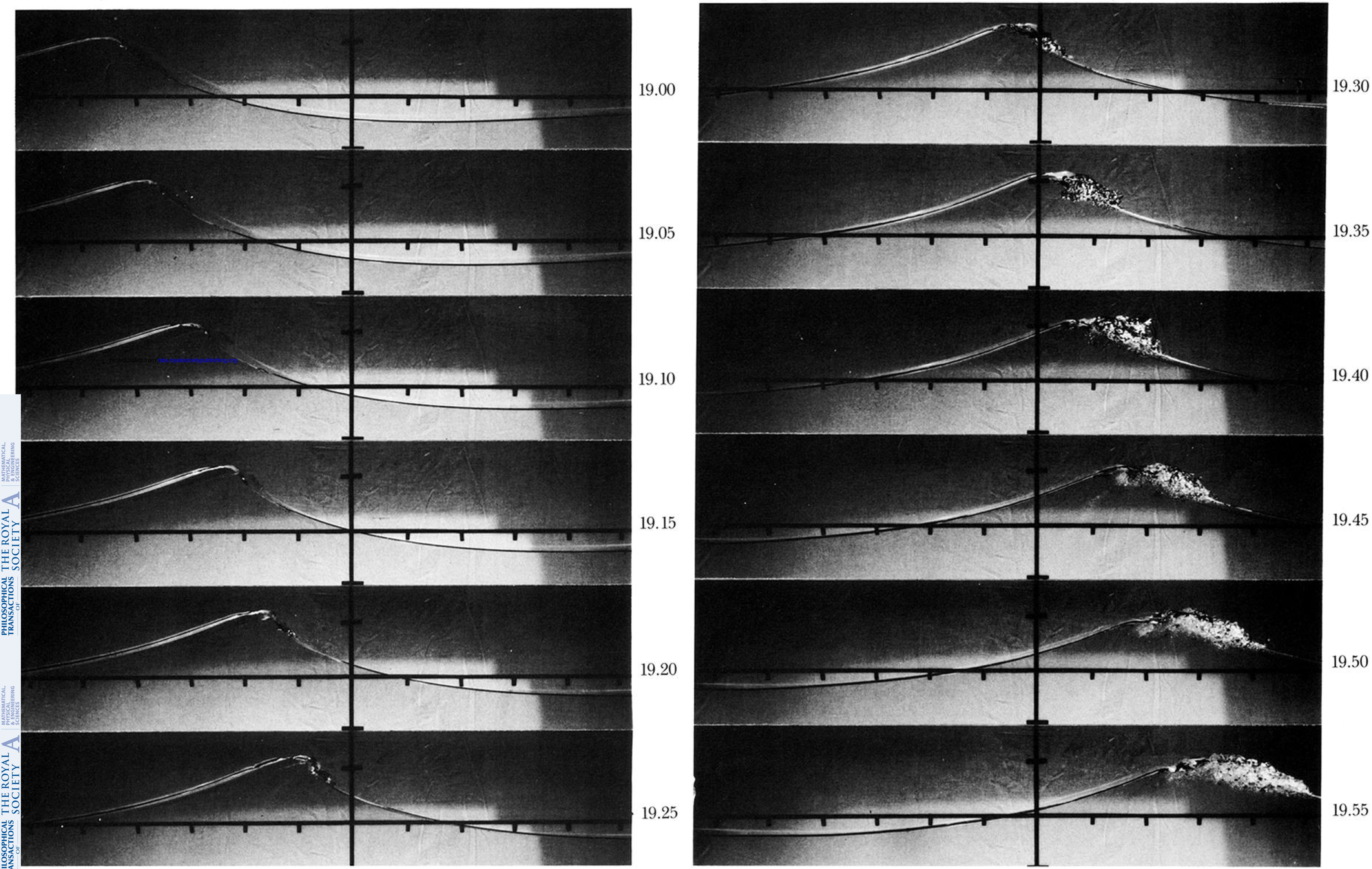

FIGURE 8. Photographs of a single spilling wave for $f_c = 0.88$ Hz $ak_c = 0.278$, $\Delta f/f_c = 0.73$, and $x_b k_c = 27.4$. Tick marks are at 10 cm intervals and times (in seconds) at right are referenced from paddle start.

FIGURE 9. Photographs of a single plunging wave for $f_c = 0.88$ Hz $ak_c = 0.352$, $\Delta f/f_c = 0.73$, and $x_b k_c = 27.4$. Tick marks are at 10 cm intervals and times (in seconds) at right are referenced from paddle start.

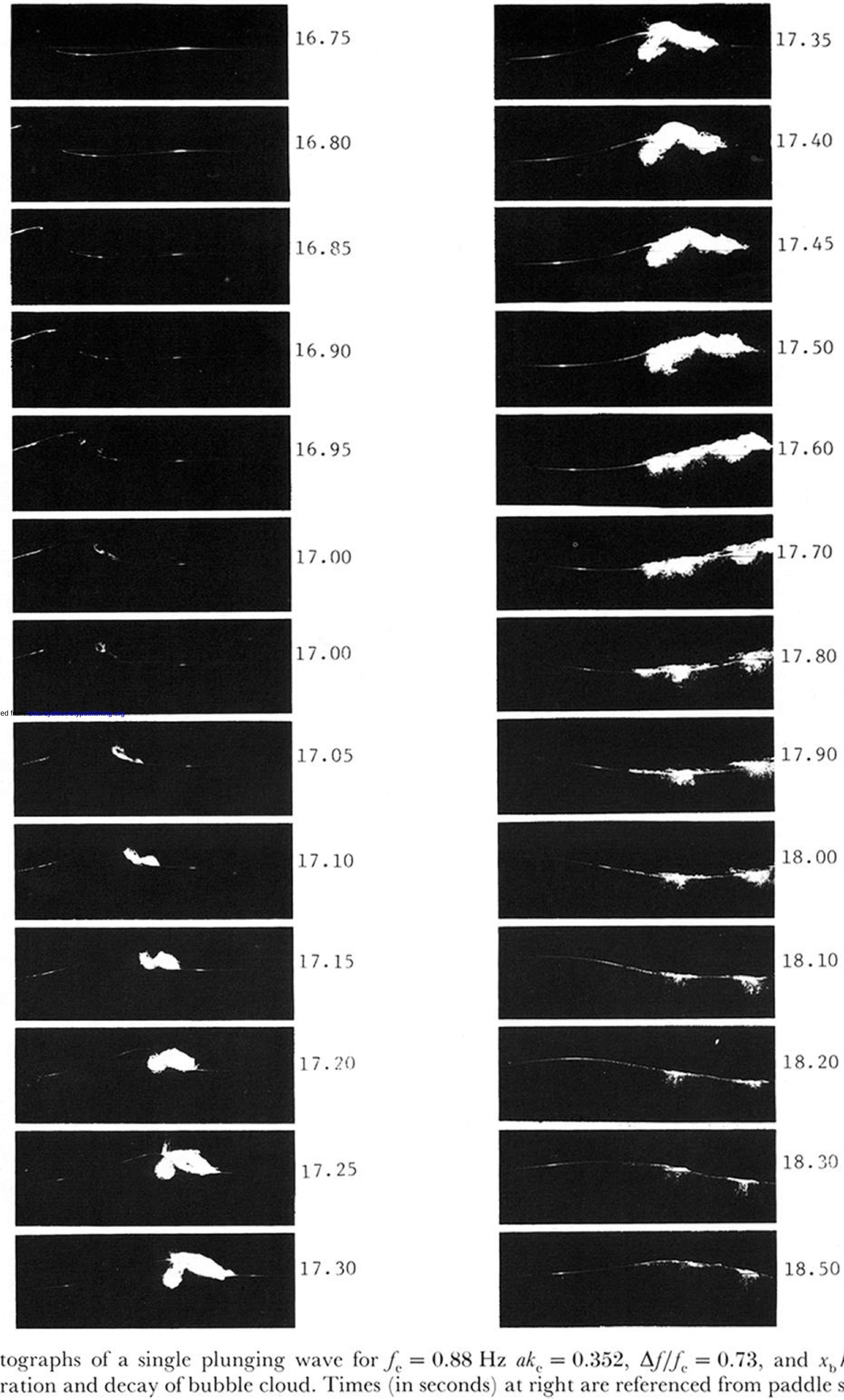

IGURE 10. Photographs of a single plunging wave for $f_c = 0.88$ Hz $ak_c = 0.352$, $\Delta f/f_c = 0.73$, and $x_b k_c = 27.4$ showing generation and decay of bubble cloud. Times (in seconds) at right are referenced from paddle startup.

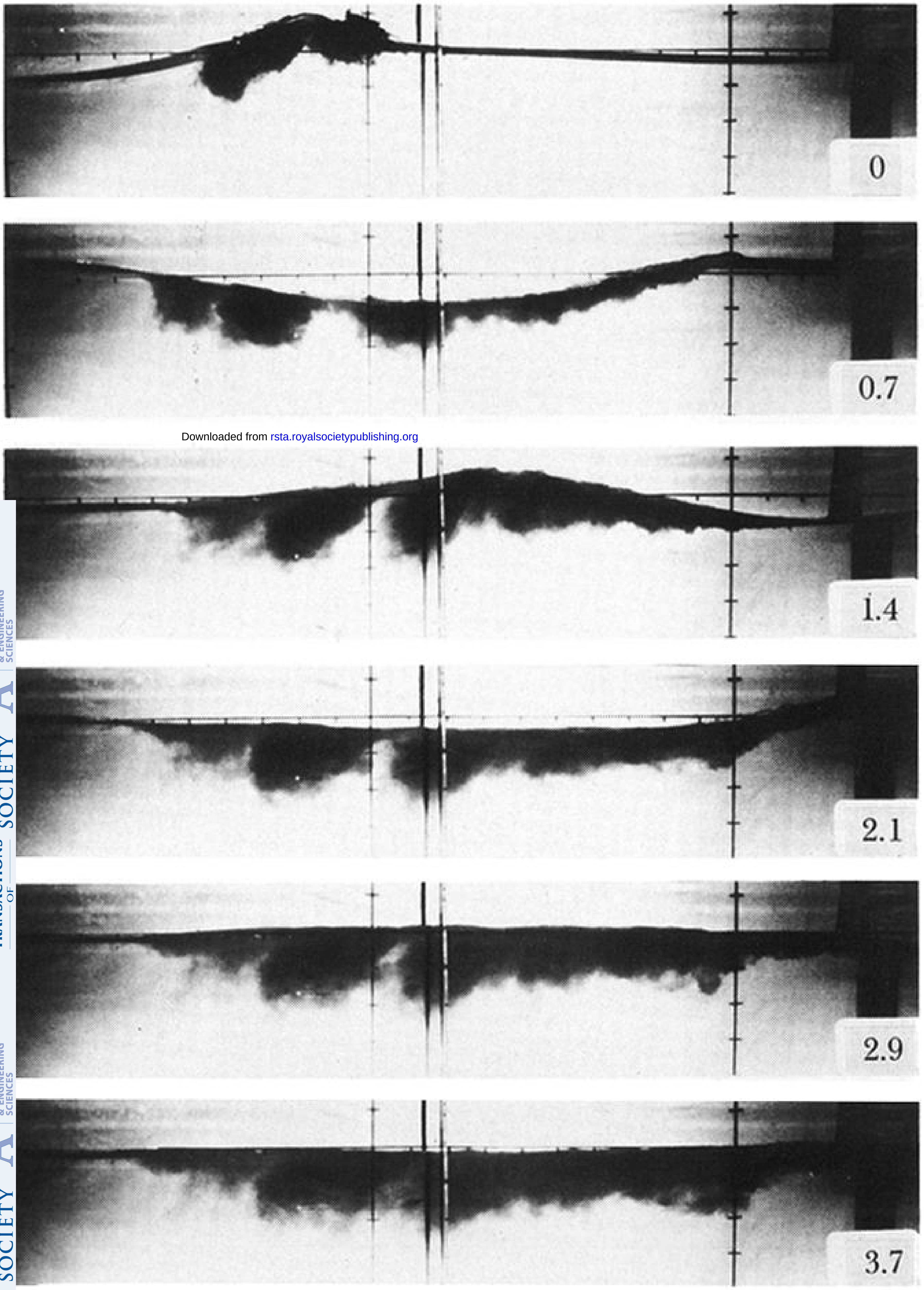

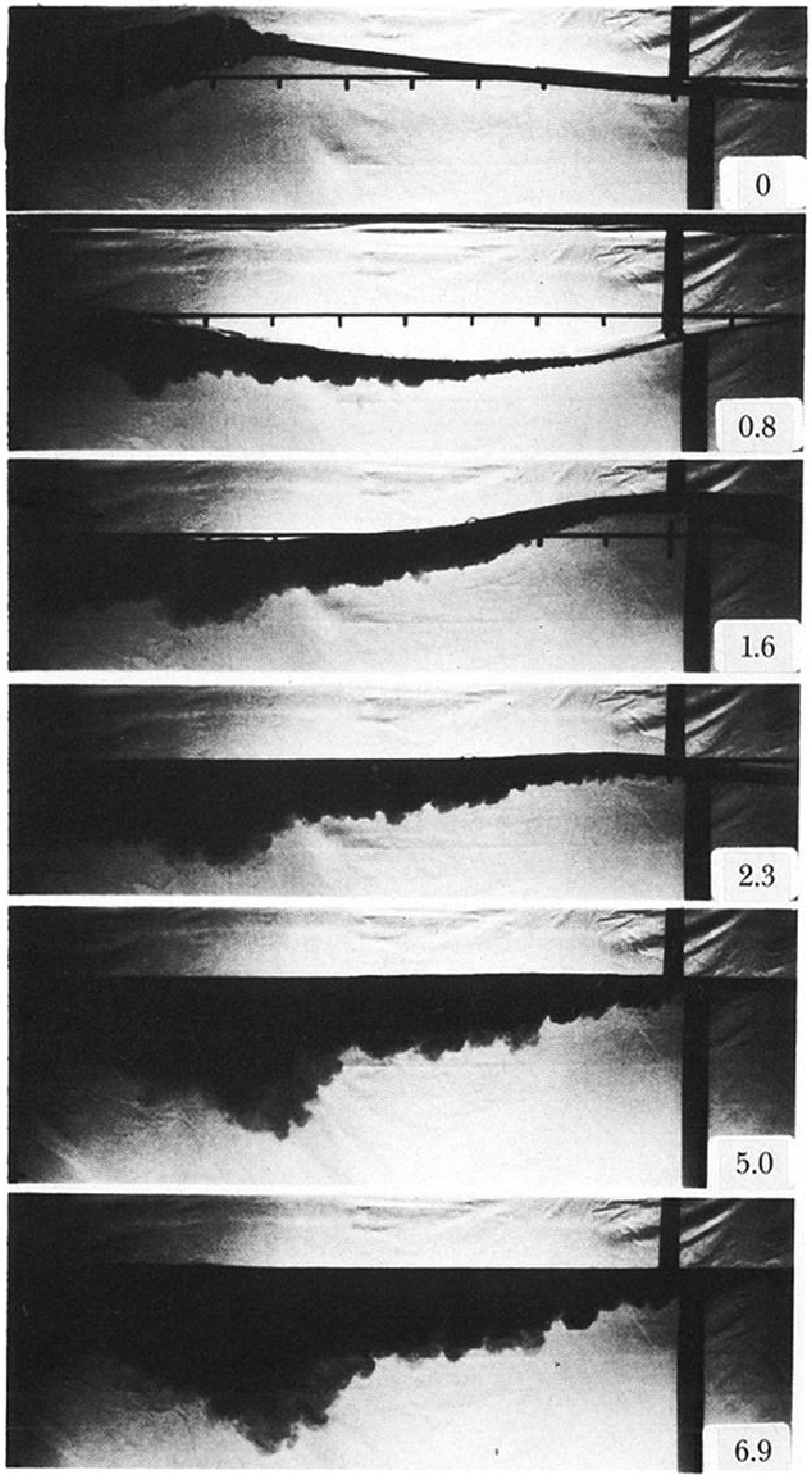

FIGURE 29 (left). Photographs of dye mixing under a plunging breaker for $f_c = 0.88$ Hz, $ak_c = 0.352$, $\Delta f/f_c = 0.73$, and $x_b k_c = 27.4$. Tick marks are 10 cm intervals. Numbers at right are elapsed times in seconds from top frame.

FIGURE 30 (right). Photographs of dye mixing under a spilling breaker for $f_c = 0.88$ Hz, $ak_c = 0.278$, $\Delta f/f_c = 0.73$, and $x_b k_c = 27.4$. Tick marks are 10 cm intervals. Numbers at right are elapsed times in seconds from top frame.